5-2020

Influences of material extrusion additive manufacturing (MEAM) parameters and additives on polyvinylidene fluoride (PVDF) properties.

Niknam Momenzadeh
University of Louisville

INFLUENCES OF MATERIAL EXTRUSION ADDITIVE MANUFACTURING (MEAM) PARAMETERS AND ADDITIVES ON POLYVINYLIDENE FLUORIDE (PVDF) PROPERTIES

BY

Niknam Momenzadeh

B.S., Mechanical Engineering 2012

M.S., Mechanical Engineering 2015

A Dissertation Submitted to the Faculty of the

J. B. Speed School of Engineering University of Louisville

In Partial Fulfillment of the Requirements for the Degree of

Doctor of Philosophy

in Mechanical Engineering

Department of Mechanical Engineering

University of Louisville

Louisville, Kentucky

May 2020

INFLUENCES OF MATERIAL EXTRUSION ADDITIVE MANUFACTURING (MEAM) PARAMETERS AND ADDITIVES ON POLYVINYLIDENE FLUORIDE (PVDF) PROPERTIES

By

Niknam Momenzadeh

A Dissertation Approved on

April 14, 2020

by the following Dissertation Committee:

_____

Dissertation Director: Dr. Thomas A. Berfield

_____

Dr. Roger Bradshaw

_____

Dr. Keng Hsu

_____

Dr. Li Yang

ACKNOWLEDGMENTS

I would like to express my sincere gratitude and thanks to my supervisor, Dr. Thomas A. Berfield for his support and guidance throughout my PhD studies. I would like to thank him for encouraging my research and for believing in me and for taking me on as a PhD student in the first step and allowing me to grow as a research scientist. I wish him the best.

I also wish to thank my committee members – Dr. Roger Bradshaw, Dr. Keng Hsu, and Dr. Li Yang for their time and scientific advice about my research.

I should express appreciation for my research group members – Masoud Derakhshani, Trung VT Hoang, Dr. Daniel A Porter. It was a pleasure for me to work with this research group. In addition, a big thank you also goes out to my colleagues at University of Louisville – Dr. Hadi Miyanaji, Qasim Shaikh, Dr. Subrata Nath, Dr. Shanshan Zhang, Carson Stewart, Benjamin Hutcherson for their time and help.

Moreover, I would like to truly thank my wonderful parents who have sacrificed much during their lives for me. Thanks dad and mom for guiding me through life and giving me the strength to chase my dreams.

The last, but not the least, I would like to express my sincere appreciation for my wife, Sahar. Thanks for your love, understanding, unconditional and endless support during my good and bad times.

ABSTRACT

INFLUENCES OF MATERIAL EXTRUSION ADDITIVE MANUFACTURING (MEAM) PARAMETERS AND ADDITIVES ON POLYVINYLIDENE FLUORIDE (PVDF) PROPERTIES

Niknam Momenzadeh

April 14, 2020

Beyond the beneficial characteristics of smart polymers associated with all polymers such as flexibility and cost fabrication, smart materials exhibit multifunctional behaviors. The prospect of integrating structural and sensing/actuation capabilities into a single structure gives design engineers an ability to innovate highly novel, multi-functional creations. Polyvinylidene Fluoride (PVDF) is one of the widely used multi-functional materials which offers a variety of desirable material properties. It possesses exceptional chemical and UV resistance, biocompatibility, low processing temperature and affordable price making it a competitive choice for many commercial applications. In addition, among polymers, PVDF is simply the most dominant piezoelectric polymer.

On the other hand, material extrusion additive manufacturing technique helps to fabricate parts with different levels of complexity which can be joined with PVDF advantageous properties to be useful for different purposes. However, due to high thermal expansion and low surface energy of PVDF material, fabrication of this semi-crystalline

thermoplastic polymer via material extrusion process is challenging and commonly results in substantial stress accumulation during filament extrusion and unwanted distortion in printed parts.

In order to facilitate the printing challenges, advanced manufacturing techniques and optimal printing parameters were employed to create viable 3D printed PVDF structures with a balanced mix of mechanical and electromechanical characteristics. In addition, effect of deposition parameters on potential piezoelectric properties of PVDF 3D additively manufactured components were investigated. Moreover, in order to enhance net piezoelectric properties of fabricated parts, impact of post processing methods like annealing process and corona poling on piezoelectric behavior of printed samples were evaluated. Also, microscale zirconium tungstate particulates with a negative coefficient of thermal expansion were added to PVDF matrix in the attempt to decrease the total coefficient of thermal expansion of the composite and improve the printability of PVDF materials. Experimental and simulation methods were employed in order to control and minimize component warping and residual stress in the printed objects. Successful completion of this research will help enable products and prototypes that exhibit multi-functional behavior to be rapidly manufactured, a capability that will provide benefits in a variety of applications.

TABLE OF CONTENTS

LIST OF TABLES

LIST OF FIGURES

CHAPTER 1

INTRODUCTION

1.1. Motivation and problem statement

Unlike most traditional manufacturing methods, three-dimensional printing (3D Printing) /Additive Manufacturing (AM) technologies are fabrication methods in which polymers, metals, ceramics or composite components are built in a layer-upon-layer manner. While these methods do not currently lend themselves easily to mass production, they do provide great benefits with respect to design manufacturability and product storage logistics (i.e., print-on-demand capabilities).

Of the many widely available AM methods, material extrusion additive manufacturing (MEAM) is the most ubiquitous due to its ease of implementation and its highly economical and rapid production timescale. Besides the anisotropic mechanical properties of additively manufactured structures, one of the drawbacks of MEAM as opposed to injection molding is related to limitations of source material. Of interest to the advancement of the field is the creation of viable 3D-printed MEAM components made with new materials and functionalities, that also demonstrate reasonable mechanical and rheological properties. Due to the similarities in stresses during extrusion and mechanical stretching, MEAM is an intriguing approach to induce piezoelectricity within additively manufactured Polyvinylidene Fluoride (PVDF) components. But 3D printing of this

semi-crystalline polymer by material extrusion method is challenging. One of the impediments of PVDF additive manufacturing is related to its high coefficient of thermal expansion (CTE), which leads to substantial component warping during deposition. PVDF has high CTE compare to common thermoplastic polymers which are used in fused filament fabrication (FFF) printer as a feedstock material. For instance, the CTE value for most PLA and ABS filaments are in the range of 70-120×10^{-6}/°C, while PVDF CTE value is in the range of 124-180×10^{-6}/°C according to one datasheet [1]. Higher CTE can affect the thermal stresses within the printed objects during printing; this may increase the probability of unwanted distortion.

In addition, PVDF is a fluoropolymer with low surface energy (LSE); such polymers are noted for their non-stick properties. Therefore, the bonding quality both between the first printed layer and heated bed, as well as inter-layer adhesion, are other major challenges for 3D printing of this polymer. During 3D printing, upon cooling from the filament deposition hot-end (210-225°C), the PVDF matrix will be under pressure to shrink a large amount (up to 3-4%), much as observed for injection molding cases [2, 3].

Material extrusion additive manufacturing of film-like PVDF structures is much easier than fabrication of truly three-dimensional objects. The increased number of layers in taller specimens produces higher temperature gradients and a greater number of cooling-heating cycles within the printed part. Consequently, residual stresses are increased, and unwanted distortion may occur in the build if not properly constrained [4]. A survey of the recent work on FFF printing of PVDF reflects these challenges, revealing a huge gap in the field with respect to specimen geometry. Nearly all PVDF 3D printing studies are limited to thin films or micro-scale 3D structures, with the tallest height of the

reported specimens remaining below 0.7 mm, relating to just 1-2 printed layers [5-8]. As the fabricated structure base dimensions increase, the likelihood of partial detachment between the part and the base plate rises.

Apart from dimensional accuracy, poor mechanical and electro-mechanical properties of printed parts compared to traditionally manufactured counterparts are the other issues related to PVDF MEAM 3D printed objects. Attempts were made to increase these properties of PVDF additively manufactured components in order to pave the ways toward wider applications of 3D printed smart materials specially PVDF. In addition, a "design of experiments" methodology has been used to test influences of particulate loading concentration on component warping, mechanical properties and ultimately the piezoelectric effect behavior demonstrated by printed composite structures.

1.2. Hypothesis and approach

The main hypothesis of this work is that the inherent stresses associated with creating thick parts of PVDF objects using material extrusion additive manufacturing process can be harnessed to induce piezoelectric behavior in PVDF parts with any complex geometry. More specifically, generation of higher magnitude local residual stresses will promote the electro-mechanical coupling responses and increase the effective piezoelectricity. Towards this end, a thorough investigation has been performed into MEAM parameters and PVDF microstructure relationships, characterized via scanning electron microscopy (SEM) and Fourier transform infrared spectroscopy (FTIR). In addition, residual stress testing and component warping characterization was performed through both experimental and simulation modeling. Piezoelectric response testing was done through dynamic electro-mechanical response characterization. In

addition, the properties of PVDF copolymer (PVDF-TrFE) components with the same deposition parameters were compared with homopolymer PVDF mechanical and piezoelectric behaviors.

According to molecular mobility changes, recrystallization and phase transformation of homopolymer PVDF, it was hypothesized that post-fabrication heat treatments could improve the mechanical and electro-mechanical coupling responses of MEAM fabricated PVDF structures. Effects of temperature and time of the annealing treatments on the strength of material and β-phase fraction within the samples were characterized by mechanical tensile testing and FTIR tests.

The final hypothesis driving a part of this study is the notion that a combination of micro-particulate loading and fused filament fabrication (FFF) deposition parameter refinement can be leveraged to control the semi-crystalline phase and microstructure morphology of PVDF, ultimately reducing the residual stress and warpage of additively manufactured polymer components. To investigate the effects of adding zirconium tungstate particulate to the PVDF matrix on physical, mechanical and piezoelectric behavior of printed samples, a variety of experimental techniques such tensile testing, digital image correlation system (DIC) and FTIR tests were employed. It was further hypothesized that electrical poling could enhance the piezoelectric responses within a fabricated PVDF 3D part based on increased dipole alignments induced through a corona poling station with a variable high voltage source. Electromechanical response for these was directly evaluated using an energy harvesting cantilever beam application test case.

In brief, the stated hypotheses of this research were tested through a series of experiments, which involved four different primary targets areas:

- Evaluate the viable deposition parameters for 3D printing of PVDF structures and probe the relationships between piezoelectric behavior and printing parameters of PVDF parts
- Component warping and residual stress measurement utilizing experimental and simulation results
- Influences of zirconium tungstate additives as a material with negative coefficient of thermal expansion on characteristics of PVDF components fabricated via MEAM
- Electro-mechanical and mechanical properties enhancement of material extrusion additively manufactured PVDF components using post-processing methods (annealing and electrical poling).

1.3. Overview of dissertation

This study aims to investigate the MEAM deposition parameters and post-processing techniques for creating viable 3D printed PVDF structures with a balanced mix of mechanical and electrical properties. An introduction and overview of the work performed is presented in Chapter 1. Chapter 2 constitutes a review of relevant literature that will provide a background on important topics, as well as the current state of the field for context. Chapter 3 presents a study into the viable printing parameters for creating MEAM PVDF components with precise physical dimensions and appearance. Chapter 4 provides insights into the effects of post-fabrication thermal treatments, supplementing the feedstock material with a copolymer (PVDF-TrFE), and electrical poling. In Chapter

5, the thermo-mechanical behavior of MEAM PVDF is explored, including both experimental quantifications and simulation of the distortions and residual stress states. Chapter 6 gives the effects of adding negative coefficient of thermal expansion material particulate into the feedstock as a means of controlling printed structure dimensional tolerances. Finally, conclusions and future work are given in Chapter 7.

CHAPTER 2

LITERATURE REVIEW

2.1. Piezoelectricity and smart polymer materials background

Smart materials or multifunctional materials consist of materials which are useful in variety of applications based not only on their physical structural properties, but also because of additional intrinsic mechanical, thermal, or electrical capabilities they demonstrate [9, 10]. Smart materials are divided into active and passive groups; the active ones have the capability to react to external stimuli or environmental condition such as electrical, magnetic, mechanical, thermal, chemical or other origins. On the other hand, the passive smart materials such as fiber optics do not possess this inherent ability and no reaction occurs when external stimuli are applied on them. Piezoelectric, electro-active polymers, magnetostrictive, shape memory alloys, hydrogels and thermochromic materials are some examples of the several types of active smart materials which are employed in different fields [11].

Piezoelectricity is a material characteristic that is described as the ability of producing electrical charge when subjected to mechanical stress (or vice versa); when means piezoelectric material can transmute mechanical energy to electrical energy and vice versa [12]. Piezo has a Greek root “Piezin”, which means to press, and piezoelectricity defines as electricity derived from pressure. In the late 1800’s, Jacques

and Pierre Curie found that quartz crystals would generate electric charges under applied pressure. The converse effect of piezoelectric phenomenon (stress generation by applying electrical field) was investigated by Lippman in 1881. This property can be found in natural materials such as quartz, Rochelle salt, topaz, bone, dentin, and hair or man-made materials like barium titanate or lead titanate [13, 14]. One of the most broadly utilized piezoelectric material is lead zirconate titanate (PZT). Due to environmental issues, many researches have been conducted on lead-free piezoelectric materials, but there is still a huge gap for replacing PZT with lead-free piezo-electrics [15-17]. Some of the popular applications for piezoelectric materials include energy harvesting systems, actuators, sensors [18], transducers[19], piezoelectric motors, medial applications [20, 21] and driving vibrations [22].

Large group of ceramics (such as barium titanate ($BaTiO_3$), lead zirconate titanate (PZT), lithium niobate ($LiNbO_3$), lithium tantalate ($LiTaO_3$)) and some select polymers (like PVDF, poly-L-lactic acid (PLLA), polymethyl-L-glutamate (PMG)) exhibit piezoelectric behavior [13, 23]. While piezoelectricity traditionally occurs within electro ceramics, piezoelectric behavior in polymers arises from a few limited, basic mechanisms. Polymers that demonstrate piezoelectricity generally demonstrate lower ~~piezoelectric~~ coefficients than their ceramic counterparts, but the greater strain tolerance of piezoelectric polymers make them highly useful in certain applications. The induced strain (electrically or mechanically driven) can be up to two orders of magnitude higher than for ceramics [24]. The source of piezoelectricity within polymers generally falls into one of the following categories [25, 26]: 1) a semi-crystalline microstructure, at least one phase of which produces a net polarization change under loading/unloading (the case for

PVDF); 2) an amorphous microstructure, but with a molecular dipole structure that can be reoriented under an electric field; 3) a microstructure including voids that contain charged media, like gases or ionic liquids (not feasible for MEAM processes); or, 4) a composite microstructure, containing fibers or particulate demonstrating net dipoles embedded within a polymer matrix.

Polymers are flexible materials, much more durable than ceramics, and can be formed easily. These unique features make piezoelectric polymers an attractive and widely-studied class of materials [27]. PVC [28], nylon-11 [29], PVDF and its copolymers are such polymers that exhibit piezoelectric behaviors. Piezoelectric properties of properly oriented PVDF was discovered by Kawai in 1969 [30]. Multiple polymer films consist of polyvinylidene fluoride, polyethylene, polypropylene, polycarbonate and other polymers with 0.003-0.005 cm thickness were stretched multiple times at fairly high temperature (100-150 °C). The spontaneous polarization and piezoelectric constants were measured, while an electrical field (approximately 300 kV/cm) was applied to them. It was showed that, comparing to other kind of polymers, PVDF has more piezoelectric attributes. Since then, PVDF have been used in various industries such as ultrasonic and medical transducers, headphones, hydrophones, microvalves, vibrometer, air flow and pressure sensors, etc. [23, 31-34].

2.2. Structure and properties of polyvinylidene fluoride (PVDF)

PVDF is a thermoplastic polymer with $(-CF_2–CH_2-)_n$ molecular structure that offers a variety of desirable material properties. The magnitude of piezoelectric responses of this semi-crystalline polymer and its copolymer and terpolymer is the greatest among the other polymers [35]. PVDF can demonstrate a significant piezoelectric coefficient

sufficient for a variety of sensing, actuation, or energy harvesting applications. The caveat for enabling effective piezoelectricity in PVDF is that the material must contain a substantial content of the all trans (β-phase) configuration of the ($-CF_2-CH_2-$) molecular structure [36-38]. In addition to its phenomenal resistance to corrosive acids (such as HF, HBr and HCl), PVDF has been also recognized as a biocompatible material with various medical applications [39-43]. PVDF is a non-toxic material with high thermal and hydrolytic stability, and exhibits good resistance to degradation under UV radiation [44, 45]. When used as a binder in composites, PVDF has also shown resilience in abrasive wear applications[46].

Electro-mechanical coupling behavior of this electro-active polymer are highly linked to its microstructure; when configured in the proper semi-crystalline phase, PVDF is recognized as one of the few piezoelectric polymers to demonstrate a large enough piezoelectric effect to be used in sensing [47, 48], actuation [49, 50], and energy harvesting applications [51, 52]. The microstructural phase is a function of the stress state and the thermal history experienced by the material during the fabrication process. Based on processing method, PVDF has five different crystalline polymorphs (α, β, γ, δ, ε), with, four of these having a net dipole (α is non-polar phase). Between them the β-phase has respectable piezoelectric responses due to its polar molecular structure. The α-phase is the most stable phase of PVDF, which creates directly from cooling of the melt. Due to the molecular chain conformation of this polymorph, fluorine atoms cancel out each other and make PVDF α-phase a non-polar polymorph. The β-phase has the strongest piezoelectric responses because of its non-zero dipole moment of the chain structure. Since, the piezoelectric properties of fabricated PVDF depend on the amount of

crystalline β-phase, achieving the β-phase content is favorable. Other phases can potentially be converted to β-phase content through combinations applied of thermal, electrical and mechanical energy or particle addition [38, 53-55]. Figure 1 shows a schematic representation of three different (α, β, γ) chain conformations of PVDF. Commercial piezoelectric PVDF is generally manufactured by mechanical stretching sheets of material by up to 300% strain, either uniaxially or biaxially [6, 36]. However, the planar geometry of these piezoelectric polymer sheets ultimately limits its application potential. Annealing at high pressure and poling are other methods for converting other phases of PVDF to β-phase [56].

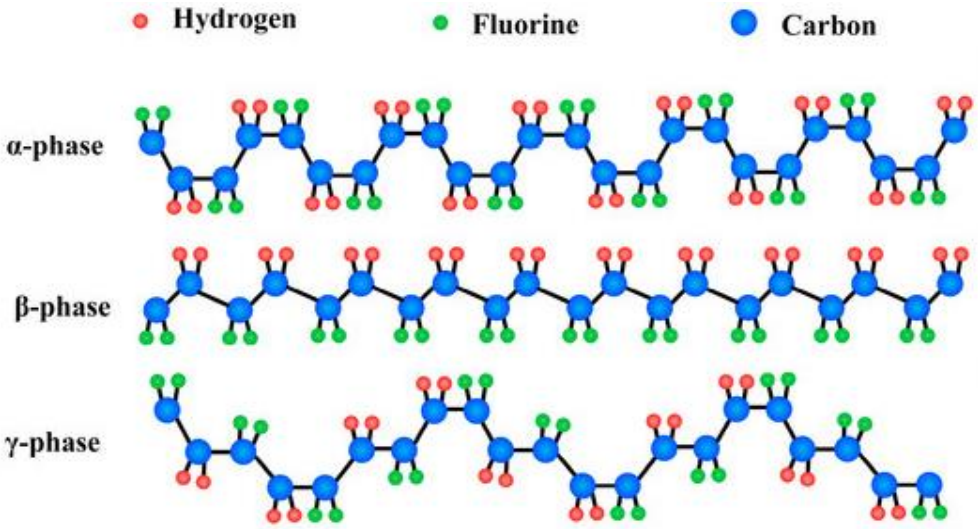

Figure 1. Schematic view of three common chain conformations of PVDF phases[57]

Transition from α phase of pure homopolymer PVDF into β-phase by drawing process, includes necking and structural changes steps [58]. PVDF α-phase resulting from melting has a ringed spherulitic structure with monoclinic cell unit and trans-gauche-trans- gauche' conformation. By applying the mechanical stretching to PVDF sample, parts lose their thermomechanical stable structure and change to other energetically

favorable phases. Considering the carbon atom spacing differential between the □-phase and β-phase shown schematically in Figure 1, one can see that the β-phase structure occupies a longer natural period along the molecular chain direction. Therefore, in order to accommodate the applied mechanical strains, the spherulitic form of PVDF is rearranged into a fibrillar structure and creates the all-trans planar zig-zag (TTTT) conformation which is called the β-phase of PVDF. Results showed that stretching temperature and drawing ratio have more impact on β-phase fraction than stretching speed [59-61].

2.3. Additive manufacturing (AM)

AM is a technology in which a digital three-dimensional (3D) model is utilized to create a part geometry by joining the constituent materials layer-upon layer. There are some synonyms has been used in literature instead of AM, like solid freeform fabrication, additive fabrication, layer manufacturing, rapid prototyping, automated manufacturing, direct digital manufacturing and 3D printing [62, 63]. Although the general strategy (layer-based production fashion) is the same in all AM methods, according to ASTM F2792-12a, AM is divided into these seven different categories: material extrusion, binder jetting, directed energy deposition, material jetting, powder bed fusion, sheet lamination, and vat photo-polymerization [63]. Differences between these categories are related to the type and shape of raw material, the deposition method, and the adhesion/bonding technique. AM techniques were invented in the late 1980s as a way to create prototypes and visionary objects, but it has evolved rapidly in the past decades and nowadays can be used to fabricate end-use components [64-66]. Although AM is not a good choice for most mass

production systems, it has been widely used in various of applications areas such as medical [67-70], aerospace [71-74], food [75-78], architecture [79-82], automotive [83-86], fashion [87-90], etc.

One the most important advantages of AM is that due to the layer-wise fashion of AM fabrication, structures with a high degree of complexity can be created; this means customized and novel objects can be easily fabricated in a 3D printer. In addition, this technique can reduce material waste and the need for tooling, and is also good choice for making lattice-based lightweight parts. Despite these unique advantages, it has some challenges. Considering the time and cost of creating parts in mass production systems, traditional manufacturing is still a better option than AM in most cases. Another AM limitation is that printers can only fabricate parts which are smaller than the printer bed size. Limitations in raw material and the mechanical and thermal characteristics of additively manufactured structures restrict the use of AM methods in industry [91, 92]. Therefore, many researchers are focusing on overcoming the limitations of AM, especially for specialized applications where the benefits make it a preferable option.

2.4. Material extrusion additive manufacturing (MEAM)

As one of the AM categories, material extrusion is a process in which components are fabricated by extruding molten thermoplastic material, high viscosity slurries, or low melting temperature metals through a nozzle or an orifice that moves in different directions. Material extrusion additive manufacturing (MEAM), also referred to as fused filament fabrication (FFF), is the first and most popular process of the extrusion-based methods that can extrude distinct material using multiple extrusion nozzles. FFF is

portable, easily scalable, and a cost effective method which can print multiple materials through a straightforward mechanism [93]. One of the main advantages of the most commercialized extrusion-based process method related to its broad compatibility with different materials. Polymeric, ceramic and metallic feedstock materials in the form of filament (cylindrical shape) can be used to fabricate functional components for variety of applications [94]. Figure 2 shows a schematic image of the MEAM method. A filament with a fairly consistent diameter is passed through a hot nozzle by using stepper motor system to create semi-liquid state extrudate of the material for creating the first layer on the platform. Once the first layer printed completely, the bed moves downward (or, conversely, the head moves upward), and the second layer is deposited on the first layer. This process occurs in layers again and again to create the whole 3D part.

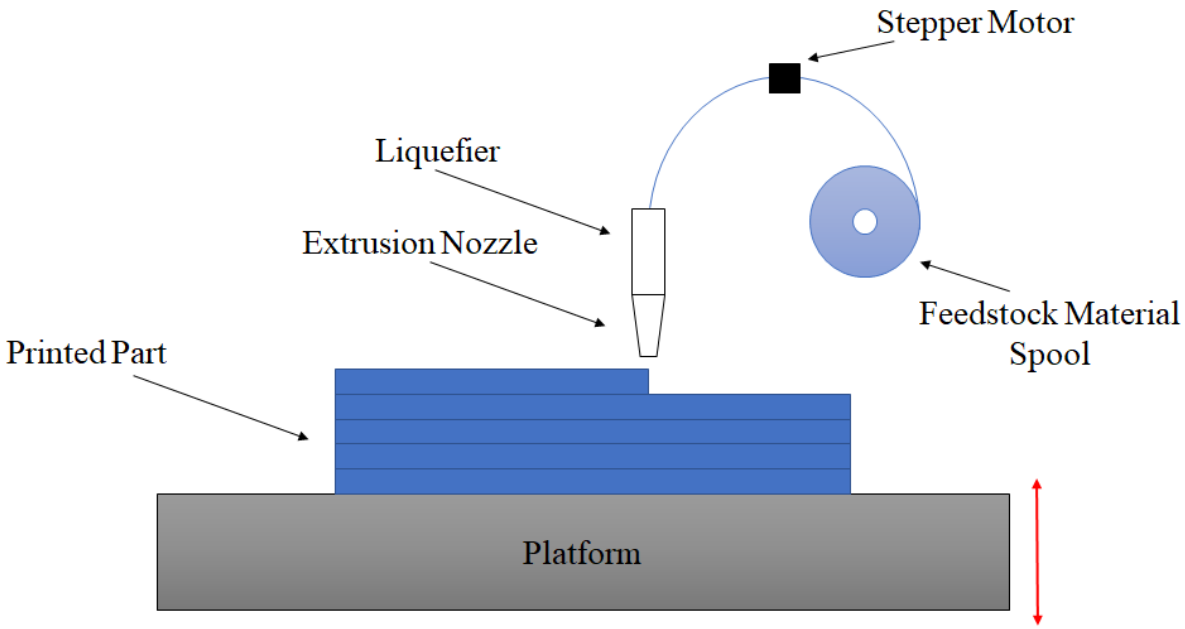

Figure 2. Schematic image of material extrusion additive manufacturing process

A liquefier is an important part in MEAM 3D printer, which melts the feedstock filament using coiled heating element or cartridge heater(s). In the most of MEAM 3D printers, the temperature of the liquefier is controlled by a thermistor on the side the nozzle. Since the thermistor is not located in the nozzle, there exists a temperature variation between filament and nozzle temperatures [95] which should be considered when polymer flow rate is investigated. Increasing the printing temperature will lead to a decrease in the flow resistance, but it may increase the residual stress with in the part [96, 97]. In order to decrease the residual stress and thermal gradients, an enclosed print chamber, cooling fan and heated platform can be used during part fabrication [98].

Two of the challenges of 3D printing polymers are the track weld quality and bed adhesion quality. Surface contact is the first step of the adhesion process in printed MEAM samples. After the initial contact between two adjacent material tracks, a neck is formed between the interfaces based on wetting. Then, during cooling, inter-diffusion and randomization of polymer chains occurs until solidification of the printed bead takes place [99, 100]. Therefore, molecular diffusion and entanglement are the main mechanisms that influence layer-to-layer bonding strength and track weld interfacial strength. Temperature at material interfaces is one of the most important factors influencing weld strength. Higher deposition (hot end) temperature leads to better bonding quality, though because of thermal degradation it should not pass a range limit. Other printing parameters, such as layer thickness, raster angle, infill density and deposition, also have a notable influence on bonding cohesion and mechanical properties of fabricated MEAM parts [101-107]. Results from prior MEAM works have shown that samples which were printed at 0° raster angle had the highest tensile strength. Samples

with thinner layer thickness, had better mechanical strength and smother surface than thicker ones, but higher manufacturing costs. In addition, higher infill density leads to parts with better mechanical responses and faster printing speed will reduce the tensile strength of objects printed with FFF printers.

One of the downsides to AM polymer parts is related to the mechanical strength of printed samples. Objects created by some of the traditional manufacturing process like injection molding were stronger than additive manufactured counter parts. Many in-process and post processing methods were used to improve the mechanical features and reduce the residual stress and strain and defects of additive manufactured components [108-110]. Regarding the material extrusion additive manufacturing (MEAM) process, Fitzharris et al. [111] investigated the effect of heat treatment process on polyphenylene sulfide (PPS) MEAM parts. According to their results, the annealing process had notable impact on increasing the ultimate tensile strength and Young's modulus due to improved crystallinity. Higher infill density and thinner layers had significant effect on increasing the mechanical properties of polymer material extrusion AM structures, regarding to Torres experiments results [112]. Cwikla et al. [113] showed that by selecting higher shell thickness, higher extrusion multiplier (above 0.9) mechanical strength is improved in fused filament fabrication process. Durgun and Ertan [114] observed that orientation and raster angle play an important role in mechanical properties and surface roughness of fused filament fabricated parts. In addition, in order to improve the mechanical, electrical, and thermal properties of FFF printed parts, several materials were added to thermoplastic polymer matrix to develop composite feedstock materials [115-118]. The

net effect of the infused particulate leads to a composite material that its specifications fall somewhere between the two individual constituent properties.

Among the feedstock materials, thermoplastic polymers are the most common used materials in extrusion-based processes. Acrylonitrile butadiene styrene (ABS) and polylactic acid (PLA) are two widely used thermoplastic polymers in MEAM [119]. Besides ABS and PLA, polyvinyl alcohol (PVA), high impact polystyrene (HIPS), polymethyl methacrylate (PMMA), polycarbonate (PC), polyetherimide (ULTEM), polyphenyl sulfone (PPSF) are some of the other types of thermoplastic polymers using in MEAM method [120-122].

As a thermoplastic material, PVDF has a glass transition temperature of around -37°C, and a melting point of 179°C. Due to the low cost, low melting point and potential for piezoelectric properties, PVDF is an intriguing choice as a feedstock material for deposition via MEAM machines. Ideally, piezoelectric PVDF could be easily 3D-printed via material extrusion processes, which would enable a variety of polymer structures with innate energy harvesting, sensing, or actuation capabilities. Such components would be desirable in applications as diverse as soft robotics, wireless sensor node arrays, and human powered products [123-126]. Tarbuttona, et al. [6]–demonstrated that phase transformation occurs in 3D printing of PVDF and the amount of α-phase (the most stable and abundant polymorph of this polymer) decreased while the β-phase content increased compared to PVDF filament. Kim, et al. [127], used in-situ corona poling electric field to improve dipole alignment, and piezoelectric PVDF films with enhanced β-phase percentage were fabricated through this technique. Porter, et al. [7] showed that there is limited influence of the relatively small electric field compared to post-processing

poling field effects on piezoelectric behavior and it was demonstrated that fabrication conditions with higher printing speeds, lower deposition temperatures and higher hot-end voltages improve the amount of crystalline β-phase in the material extrusion additively manufactured parts. In addition, according to their research, nozzle types (conical or flat) and extrusion multiplier have no significant effect on the piezoelectric responses of the fabricated components. The influences of other printing processing parameters such as infill density, fill pattern, layer thickness and nozzle diameter on the amount of β-phase content are still not determined.

In this study, different processing and post-processing experimental approaches, various mechanical, electro-mechanical and thermal characterization tests and simulation process were employed to evolve a methodology for fabricating 3D printed PVDF structures by MEAM technique.

CHAPTER 3

PVDF AS A FEEDSTOCK FOR MEAM PROCESS

3.1. Viability of MEAM PVDF

Fast progresses in FFF 3D printing, make this technique a process which not only produces prototypes, but also fabricates parts with wide area of end use application. Based on the several applications, various kinds of feed stock thermoplastic materials have been used such as PLA, ABS, nylon, polyolefins, polyamides, recycled polymer, and polycarbonate in FFF 3D printing[128, 129].

As discussed before, PVDF demonstrates a variety of remarkable material properties. The range of melting temperature of PVDF makes this thermoplastic semi-crystalline polymer a viable choice as a feedstock material for deposition via MEAM 3D printers, though this process is not without its challenges. For example, the shrinkage associated with semi-crystalline materials is generally greater than amorphous polymers [128]; this can result in material distortion and poor quality fabricated samples.

Homopolymer PVDF has a CTE of ~ 150×10^{-6}/°C from (Kynar 740 datasheet), which is 2-3 times that of traditional filament-based polymer feedstock materials like poly lactic acid (PLA), acrylonitrile butadiene styrene (ABS), and nylon-12. Although thermally induced shrinkage is not the only factor that causes MEAM components to

warp upon deposition, large CTEs increase the probability of this phenomenon during the plastic extrusion process [25, 27, 128, 130, 131].

Three-dimensional (3D) printing of polymer smart materials offers great potential in terms of design of applications either requiring inherent electro-mechanical sensing or vibration-based energy production capabilities. Currently, the piezoelectric response of homopolymer 3D-printed PVDF lags the properties offered by using the costly alternative feedstock PVDF-TrFE or the geometrically limited sheets produced commercially via mechanical stretching. A survey of the recent work on material extrusion AM of PVDF reflects these challenges, revealing a huge gap in the field with respect to specimen geometry. Nearly all PVDF 3D printing studies are limited to thin films or micro-scale 3D structures, with the tallest height of the reported specimens remaining below 0.7 mm, relating to just 1-2 printed layers [5-8]. The increased number of layers in taller specimens produces higher temperature gradients and a greater number of cooling-heating cycles within the printed part. Consequently, residual stresses are increased and unwanted distortion may occur in the build if not properly constrained [4]. As the printed structure base dimension increase, the likelihood of partial detachment between the part and the base plate rises. Hence, 3D printing of film-like PVDF structures is much easier than fabrication of truly additively manufactured components.

Printing parameters play an important role in the resulting stress residual in the printed parts. The mechanical and the electro-mechanical coupling properties of PVDF are closely linked to the microstructural phase which in turn is a function of residual stress of the deposited material. Therefore, optimization of the printing parameters must include a weighting of mechanical properties, piezoelectric responses and the level of

unwanted distortion in the fabricated parts. In the current study, an experimental study was done to define the influence of printing parameters (infill density, infill pattern, layer thickness and nozzle diameter) on β-phase crystallization content within the PVDF fabricated parts. Since the piezoelectric behavior of homopolymer PVDF is essentially related to the amount of β-phase polymorph [132], knowing the relationships between the aforementioned printing parameters and resulting β-phase content will clarify the viable processing parameters based on piezoelectric responses. In addition, the influence of different process parameters on the microstructure, dimensional accuracy, and mechanical characteristics of the printed parts is systematically assessed. This work is aimed to provide helpful guidelines highlighting viable deposition parameters for 3D printing of PVDF, and the influence of those parameters.

3.2. Methodology

Printing Material

Kynar 740 homopolymer PVDF (Trident Plastics, Inc.) was procured in resin pellet form, after which it was turned into filament for MEAM printing purposes (Figure 3). Filament fabrication was performed via an in-house built, single screw Filastuder (Figure 4), which was used with the extrusion head set at a temperature of 210°C to produce uniformly cylindrical pure PVDF filament with a 1.75±0.15 mm diameter. Created filament was dried in the oven (Precision/ Thelco 26 incubator) at 50°C before printing for about 2 hours. The material extrusion additive manufacturing process was performed using a low cost Reprap Prusa i3, 3D printer (Figure 5).

Figure 3. Raw PVDF resin pellets (left), and the extruded filament (right).

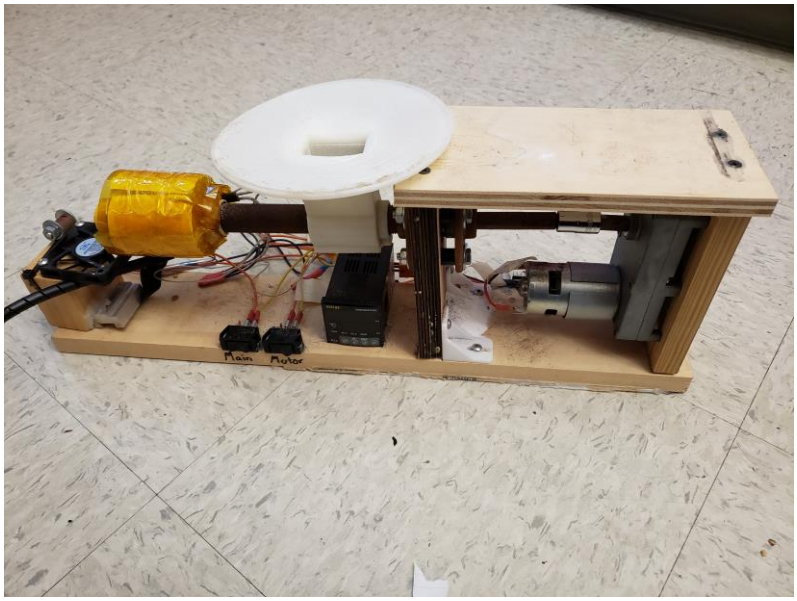

Figure 4. Filament extruder apparatus

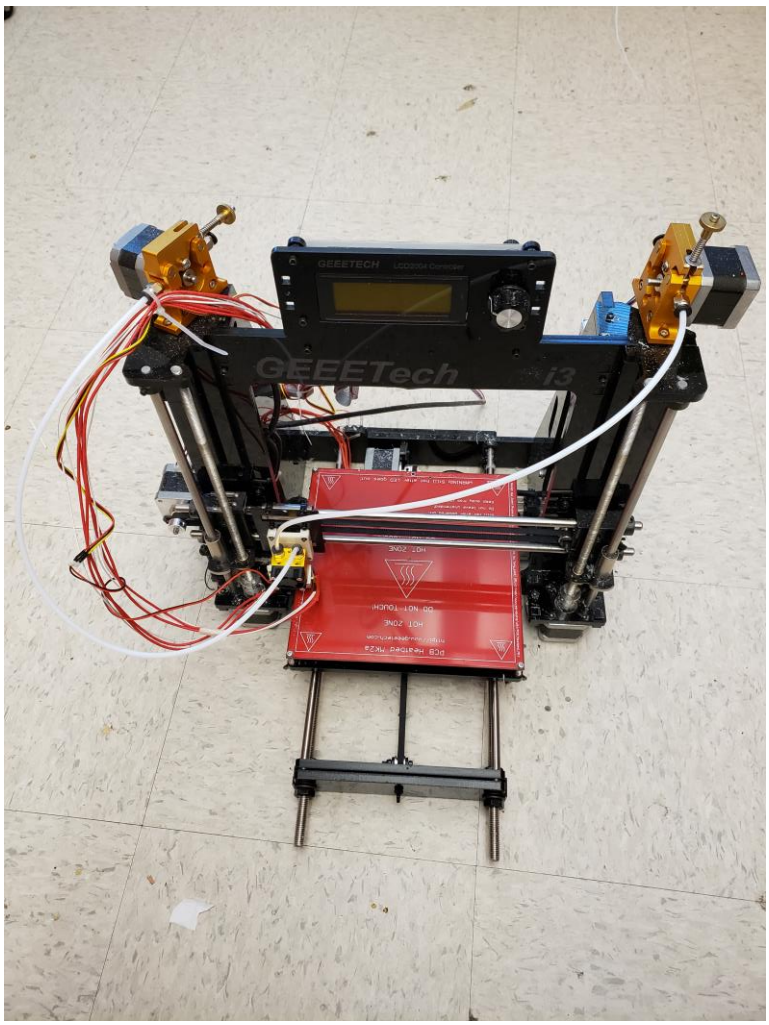

Figure 5. Reprap Prusa i3 3D printer

The deposition parameters were adjusted over a wide range of reasonable values as detailed in Table 1. In all cases the build platform was cleaned with isopropyl alcohol and then 3M blue painters' tape was applied to the deposition bed to improve adhesion to the first printed layer. Slic3r software was used for generating G-code from the input computer-aided design (CAD) files. Under each variation of the deposition parameters, test structures were printed in geometries of films, solid cylinders, rectangles, and split tube "C" structures. The height and the in-plane length dimensions of the printed objects were varied up to 50 and 100 mm, respectively.

Table 1.Printing parameters tested for fused filament fabrication of PVDF.

Extrusion Specification	Parameter Range Tested	Viable Range	Suggested Value
Deposition Temperature(°C)	180-250	200-230	220
Platform Temperature (°C)	70-120	90-110	105
Nozzle Diameter(mm)	0.2-1	0.2-0.6	0.35
Infill and Solid Speed (mm/s)	5-45	10-25	15
Perimeter Speed (mm/s)	5-35	10-15	10
First Layer Thickness(mm)	0.05-0.35	0.1-0.25	0.2
Layer Thickness(mm)	0.05-0.3	0.1-0.25	0.15
Perimeters	1-4	2-3	2
Infill pattern	Rectilinear/ Concentric/ Honeycomb/ Grid/ Triangles	Rectilinear (no major effect)	Rectilinear
Brim width(mm)	0-10	2-6	3

Viable process parameters were determined by first expanding a range parameter values around the conditions documented to be successful for 3D printing components using the common thermoplastic feedstock material acrylonitrile butadiene styrene (ABS). For each set of conditions, printed structures were evaluated for surface finish, physical integrity, and degree of component warping using dimensional measurements. Each deposition parameter was then individually incremented outwards (higher and lower values) in order to investigate the potential influences on the quality metrics and to establish the viable range of printing conditions. The range of parameters tested is shown in Table 1. Many of the printing parameters combinations resulted in unacceptable build quality. Examples of poor quality parts and the primarily attributed factors are depicted in

Figure 6(A-D). The effects of elevated extrusion temperature (above 240°C) are shown in Figure 6A. The influence of excessive perimeter speed (above 30 mm/s) is illustrated in Figure 6B, and the effects of higher and lower infill speeds (above 40mm/s and below 5mm/s) inducing excessive residaul stresses and weak adhesion quality, resulting in warping and deposition bed delamination and poor surface roughness, are shown in Figure 6C-D.

Figure 6.Printed PVDF parts experiencing poor dimensional accuracy(A), poor surface finish on perimeters(B), deposition bed delamination(C), and poor inter-layers bonding quality(D), contrasted with similar parts fabricated under viable printing parameters(E)

After the initial round of fabricating and evaluating the printed PVDF components, a narrow range of viable deposition parameters was established (Table 1). In order to test effects of combinations of parameter permetaions over this viable range, a sceond iteration of experiments using a randomized design of experiments approach with the same assesment methodology was employed. Based on the results of this assessment,

the authors report a set of suggested deposition parameters for optimal component fabrication. Example structures using these optimized parameters are shown in Figure 6E. Samples prepared under these suggested conditions were further assessed for microstructure development and mechanical response. Though in many cases a qualitative assessment of the part quality was sufficient to deem it unacceptable (parts with no structural integrity, or extreme surface roughness as shown in Figure 6(A-D)), additional mechanical tests were performed on some of the process parameters combinations near the "suggested" ones. To avoid confusion, the results of mechanical test of non-optimal printed samples were not presented and just some of the unsuccessful printed samples were generally shown in Figure 6(A-D).

The optimal values for piezoelectric and mechanical properties are different. In this research, the viable printing parameters to fabricate PVDF 3D objects with sufficient structural integrity and minimal warping were found, and the corresponding microstructure was determined. Therefore, the suggested values were not utilized for fully controlling both the mechanical properties and the piezoelectric response of PVDF. It is just established a solid baseline against which other works may be compared.

Printing parameters may have different effects on the amount of the β-phase fraction and warping rate, for example using thinner layers will increase the number of cooling and heating cycles which results in higher residual stress. Although, this residual stress is beneficial for having more β-phase fraction, it has a negative effect on the warping rate. Excellent β-phase content (indicating a good piezoelectric response) within a printed sample is ultimately worthless if the resulting component has no structural integrity. This research, tried to balance these issues by presenting a viable range of

printing parameters (parts have basic structural integrity), over which the β-phase content was measured.

Microstructure Characterization

Scanning electron microscopy was used to inspect printed surface quality and characterize the presence of porosity between layers. Typical top layer surface roughness and porosity are shown in Figure 7A, while a representative image of the generally smoother printed PVDF bottom surface is shown in Figure 7B. In general, the side-to-side fusion between individual bead tracks was observed to be high quality. However, occasional pores were found between layers as shown in Figure 7C.

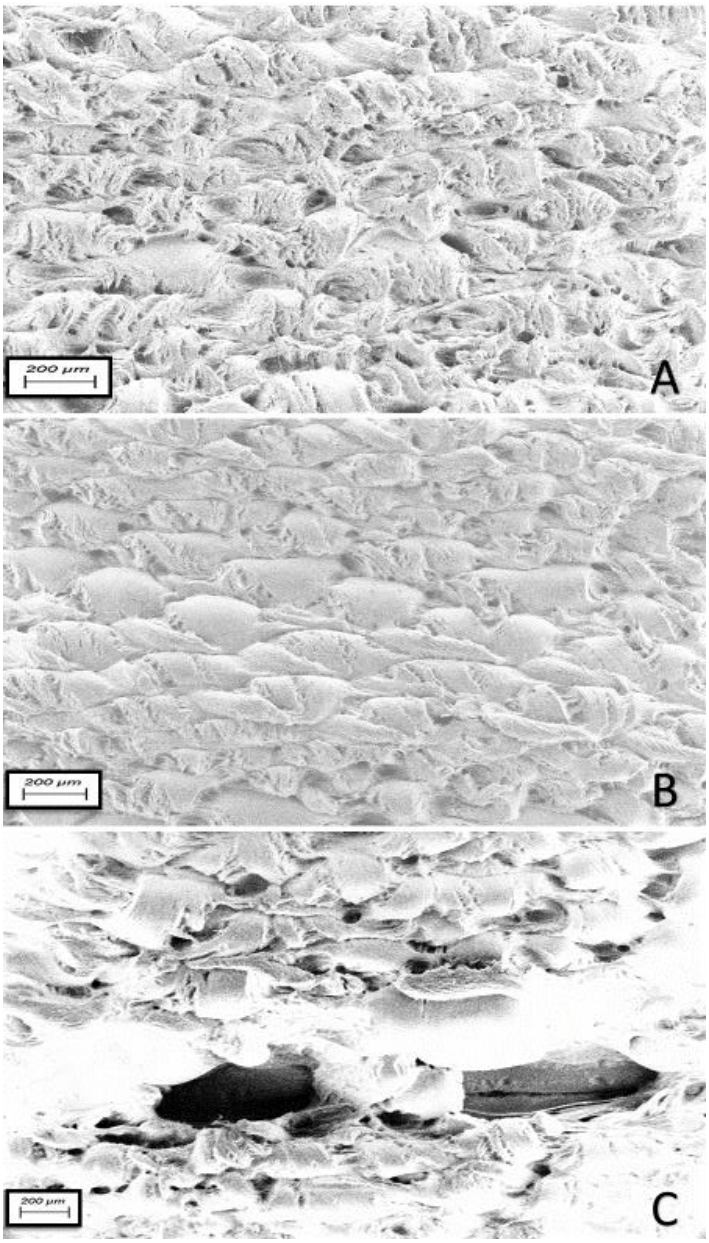

Figure 7.Scanning electron micrograph showing the top surface (A) and bottom surface (B) of an MEAM printed PFVD structure, as well as a printing defect pore (C) located between layers

Mechanical Characterization

Basic mechanical properties of PVDF components printed using optimal parameters were determined via tensile testing in an MTI universal material testing machine at a constant displacement rate of 1.25 mm/min. Following ASTM standard

D1708, six samples with 1.5 mm thickness (corresponding to 10 printed layers) and 70% infill density were designed and printed to measure the effective Young's modulus of the PVDF parts. Specimen dimensions are shown in Figure 8. A digital image correlation (DIC) system (VIC3D, Correlated Solutions, Inc.) was used for measuring the strains within the specimen gage area during testing. DIC is an optical non-contact method for measuring the full-field deformation and strain. Prior to doing the mechanical testing, all the FFF printed coupons were patterned utilizing two spray paint (white and black) in order to have artificial and random speckle pattern on the part. All DIC images were taken by two high resolution digital Cameras during tensile testing. Test results discussed in section 3.3.

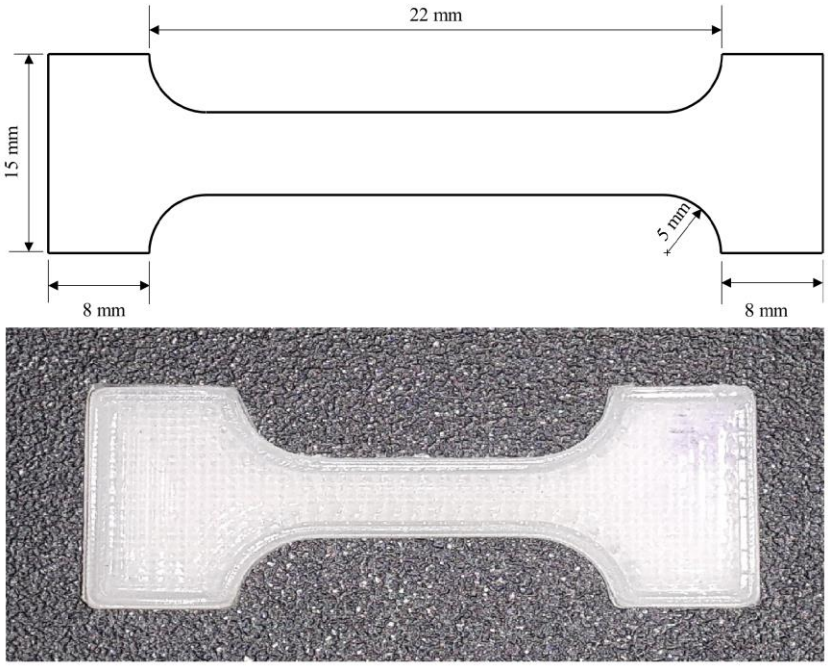

Figure 8.Tensile test specimen dimensions (top) and top surface of printed sample (bottom).

Electro-mechanical Characterization

Phase content characterization within PVDF objects was determined through the standard method of Fourier transform infrared (FTIR) spectroscopy with an attenuated total reflectance (ATR) attachment [54] using an PerkinElmer Spectrum™ 100 FT-IR spectrometer. FTIR is a well-known method that provides a wealth of significant data about the presence of various semi-crystalline phases within polymer materials. This method works by using a high-energy light source coupled with a special ZnSe crystal to measure the relative absorbance/reflectance of the incident waves across a range of frequencies. PVDF's piezoelectric properties are essentially subjected to the amount of the crystalline β-phase, this constituent is the most desirable phase from the viewpoint of piezoelectric properties in PVDF and FTIR test was performed to estimate relative semi-crystalline content[133]. Due to different contact areas between samples and special crystal in FTIR machine, all spectrums results were normalized to 1070 cm^{-1} peak before analyzing [134].

In addition, effect of printing parameters such as infill density, infill pattern, layer thickness and nozzle diameter on the electro-mechanical coupling responses of printed parts were investigated. For this purposes, specimens were deposited in six different levels of infill density, five distinct patterns of printing, four different layer thickness heights, and five different nozzle diameters (Table 2). At least three samples were fabricated for each unique set of printing parameters. PVDF 3D printed samples were shown in the Figure 9. The thickness and diameter of all samples were fixed at 3 mm and 20 mm, respectively.

Table 2.Specimens used for FTIR testing

Sample Variation #	Infill density (%)	Infill pattern	Layer thickness (mm)	Nozzle diameter (mm)
1	100%	Rectilinear	0.10	0.4
2	95%	Rectilinear	0.10	0.4
3	90%	Rectilinear	0.10	0.4
4	85%	Rectilinear	0.10	0.4
5	80%	Rectilinear	0.10	0.4
6	75%	Rectilinear	0.10	0.4
7	90%	Concentric	0.10	0.4
8	90%	Honeycomb	0.10	0.4
9	90%	Rectilinear	0.10	0.4
10	90%	Grid	0.10	0.4
11	90%	Triangles	0.10	0.4
12	100%	Rectilinear	0.05	0.4
13	100%	Rectilinear	0.10	0.4
14	100%	Rectilinear	0.15	0.4
15	100%	Rectilinear	0.20	0.4
16	100%	Rectilinear	0.10	0.2
17	100%	Rectilinear	0.10	0.4
18	100%	Rectilinear	0.10	0.6
19	100%	Rectilinear	0.10	0.8
20	100%	Rectilinear	0.10	1

Figure 9. PVDF samples for electro-mechanical test

3.3. Results and Discuusion

3.3.1. Printing parameters

Processing parameters have a significant effect on the mechanical properties, dimensional accuracy, electrical behaviour, bonding quality and anisotropy of 3D printed objects, regardless of the additive manufacturing method [7, 135-139]. The primary challenges of PVDF homopolymer 3D printing are related to the bonding quality and dimensional accuracy of the deposited part. Heat flux from the hot-end into the feedstock material must be sufficient to turn PVDF into molten form and has a notable effect on bonding quality. Extrusion temperature has key impact on the neck formation phenomenon between adjacent extrudate. Higher extrusion temperature leads to larger neck growth and better bonding condition between the adjoining extrudate which makes internal voids smaller and consequently leads to higher strength components [128, 139, 140]. Hence, according to melting and transition temperature of PVDF the extrusion temperature was selected in the range of 200-230° C. Under 170 °C, the piezoelectric behavior-associated microstructure of 3D printed parts was not significant [7], and as it is shown in Figure 6B, above 230° C thermal degradation occurs. Although increasing the bed temperature takes time especially in low-cost 3D printer, since higher platform temperature improves the necking growth in each neighboring filament segment, the heated bed was utilized for printing PVDF and the platform was heated up to 90 -110° C. In addition, the heated bed helps to prevent uneven heat distribution in the fabricated part, which leads to lower dimensional tolerance losses within it.

Extrusion speed is another parameter that influences the part quality as it has direct impact on cooling condition of deposited filament and consequently the interlayer

and intra-layer bonding characteristics. Printing speed not only affects the quality of final 3D printed components, but also determines the total printing time. Although higher printing speed is desirable to reduce the fabrication time and lower the cost, it results in complications during the printing process as shown in Figure 6. Higher infill speed creates poorly bonded layers in the printed specimens. Although using lower deposition speeds improved the bonding quality between layers, they resulted in greater distortions in the fabricated parts. The viable extrusion speed range for printing PVDF was found to be 10-25 mm/s, while the perimeter speed was kept under 20 mm/s. Above this rate the resulting surface finish was not acceptable (Figure 6).

An additional consideration is the cumulative effect additional cooling and heating cycles associated smaller layer thickness selection. This influences residual stress development, microstructure evolution, warping rate, and total print time. In this work, the part dimensional tolerances and physical integrity were weighted most heavily in determining the suggested parameters. Specific applications may require different priorities, however. Here, the layer thickness was set 0.15 mm, with a thicker first layer (0.2 mm), which helped to improve the bonding quality between the first printed layer and platform.

3.3.2. Tensile Testing Results

The effective Young's modulus of specimens was calculated from the result of tensile test experiments and DIC data. Strain was computed in the linear region for printed samples. According to a 95 percent confidence window, Young's modulus and β-phase fraction of PVDF printed samples with 70% infill density was in the range of 772.4 ± 44.3 MPa and 0.433 ± 0.048, respectively. The calculated mean value of Young's

modulus of 772.4 MPa was less than the published Kynar 740 datasheet value of 1.7 GPa; it is expected for lower density MEAM components and this finding is anticipated. The lower crosshead velocity rate used in for the tensile test experimentation might have influence on the elastic modulus. In addition, the infill density of the printed components was 70%, the infill angle was 90° perpendicular to the axial dimension of the dog bone, and its Young modulus should be less than a bulk PVDF part. The effective stress-strain response for the components with infill less than 100% was found similar to [141]. Figure 10 presents the tensile test apparatus and DIC system which were used for obtaining the stress and strain graph. As it is shown, the perimeters of the sample reached higher stresses before separation than other sections of the printed parts due to the fact that the value for perimeter was set at 2 shells which is higher than infill. Figure 11 represents the stress-strain curve for six PVDF printed specimens.

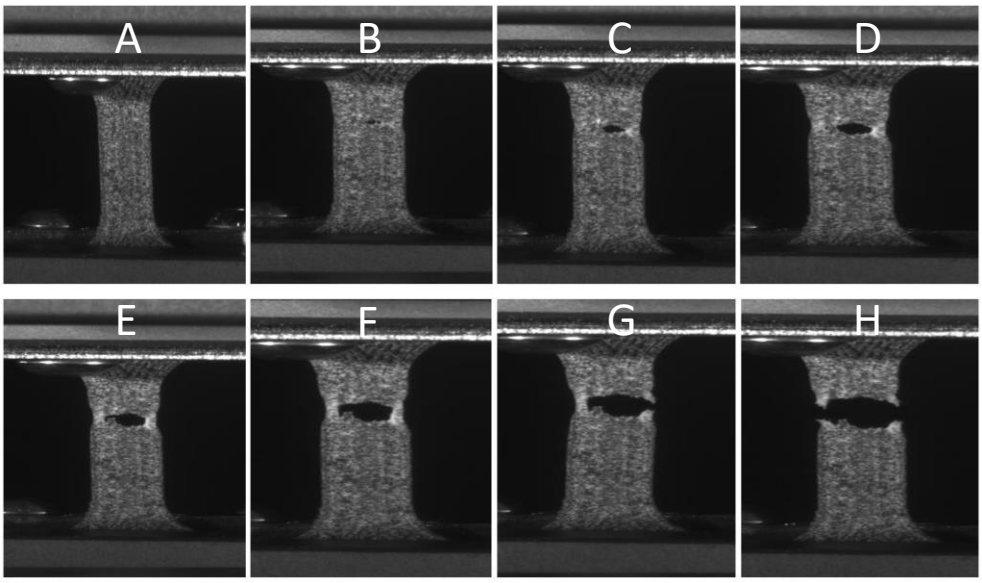

Figure 10.Tensile testing progression used for 3D digital image correlation system analysis. (Strain at A: 0.000, B: 0.079, C: 0.085, D: 0.092, E: 0.098, F: 0. 105, G: 0.113, H: 0.122)

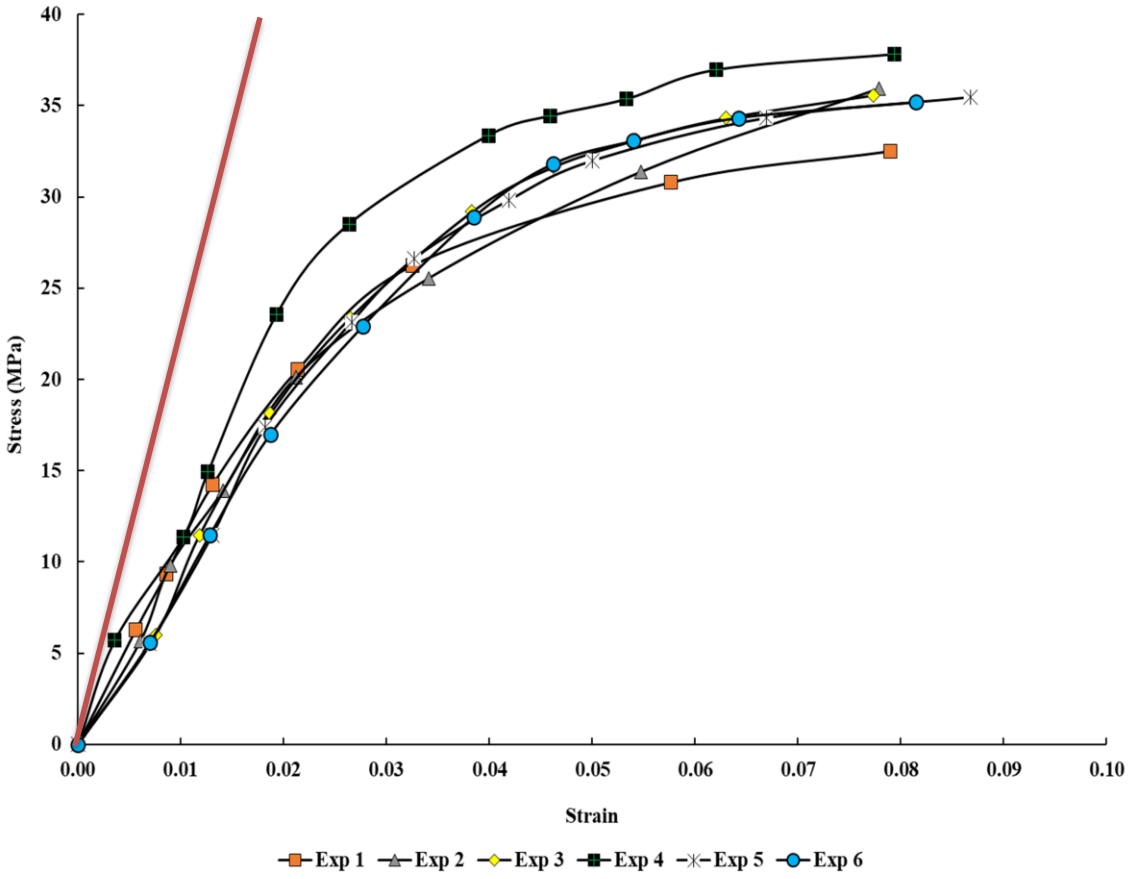

Figure 11.Stress-strain curves of six PVDF 3D printed samples (slope of the red line represents the data sheet values for Young's modulus (E=1.7 GPa)).

3.3.3. FTIR Results

FTIR spectra of printed PVDF samples is shown in the range of 650-1400 cm^{-1} (Figure 12). The FTIR data was utilized to study the PVDF polymorphism. The peaks at 840 cm^{-1} and 1279 cm^{-1} correspond to β-phase [53]. The fraction of β-phase in the specimens were calculated using

$$F(\beta) = \left(\frac{A_\beta}{1.26A_\alpha + A_\beta}\right) \quad (1)$$

where A_{α} and A_{β} represent the intensities of absorption band at 763 cm^{-1} (α-phase) and 840 cm^{-1} (β-phase), respectively. *F(β)* correspond to the relative amount of β-phase in the samples[4, 36]. Equation 1 was used to quantify the results through FTIR test which is a pathway to determine the β-phase crystallization content in the printed parts. The value of F(β) does not show the exact amount of crystalline β-phase in the PVDF samples, but it represents the relative amount of β-phase to α-phase within that part. So, equation 1 does not represent any information about other phases of printed sample like γ, δ, ε phase. Therefore, by using equation 2, β-phase content fraction was calculated for pellet, filament, extrudate and 3D part of PVDF; the calculated amount of β-phase fraction is shown in Figure 13.

The reported printing parameters were utilized to find the β-phase fraction within six specimens as it shown in Table 3. The average amount of β-phase fraction of printed samples was 0.433. Due to the extensive mechanical stretching on the filament fabrication from PVDF pellets and substantial stresses accumulation during filament extrusion, the amount of crystalline β-phase in the 3D samples was measured to be 20% and 39% higher than extruded filament from the 3D printer brass nozzle and from the filastruder, respectively. In addition, the β-phase fraction in PVDF samples was about 3 times greater than the raw pellet material. A likely reason for the increase in β-phase from pellets to 3D parts is the elevated temperatures and pressure at the tip of the 3D printer nozzle during filament deposition, somewhat ressembling the mechanical stretching process used for producing commerical piezoelectric PVDF sheets. Moreover, the crystallization from melt at high shear stress rate, which occurs at extrusion process step, has impact on the amount of β-phase fraction [6, 142]

Table 3.Fraction of β-phase within the six printed samples

Sample ID#	1	2	3	4	5	6
β-phase fraction	0.411	0.446	0.445	0.415	0.438	0.440

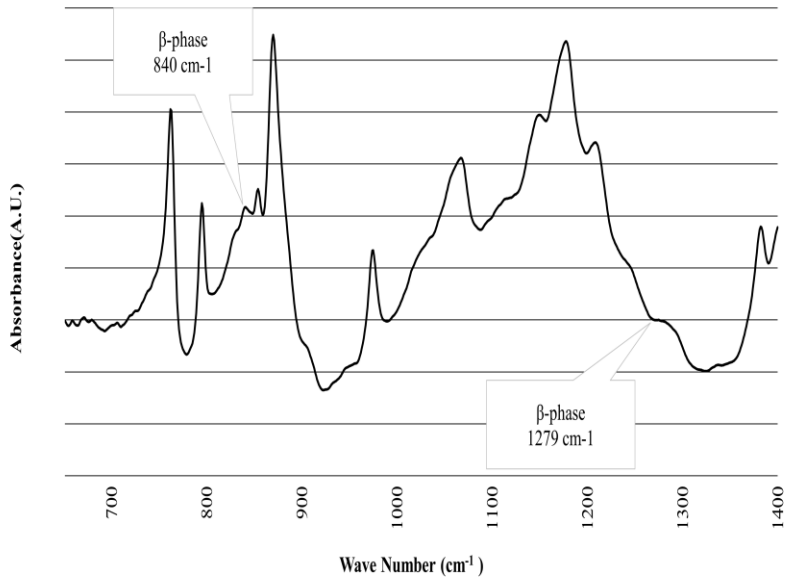

Figure 12.FTIR spectra of PVDF printed under suggested parameters.

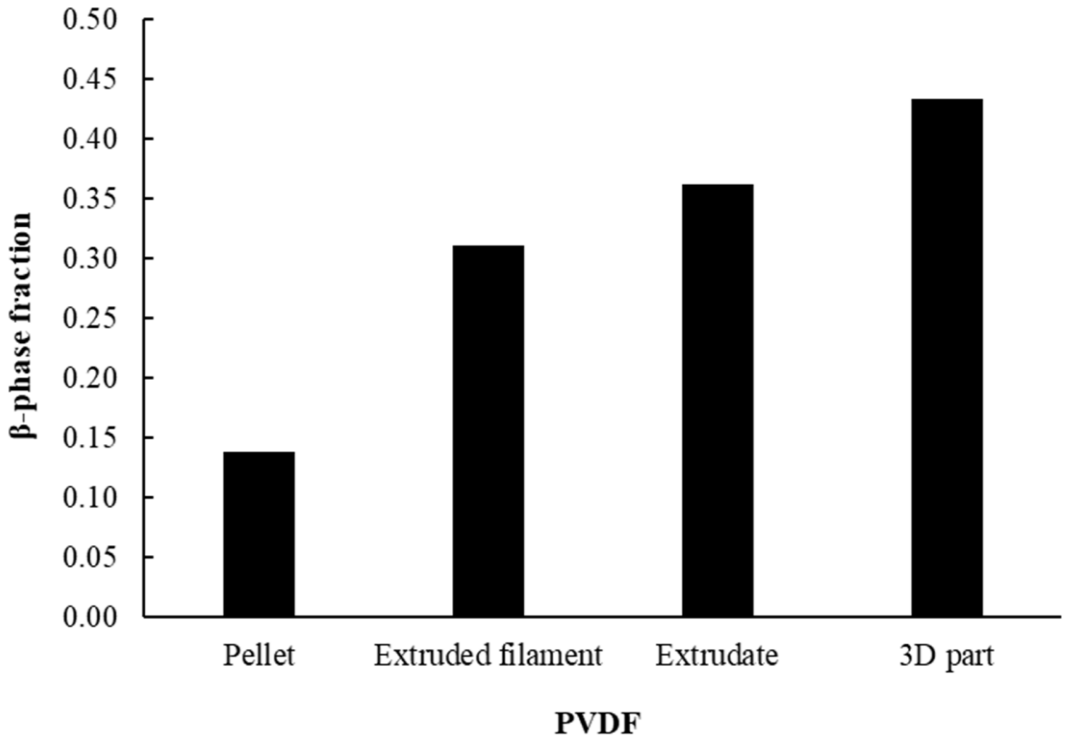

Figure 13.FTIR test results showing average β-phase fraction for PVDF homopolymer at different states of MEAM processing.

The stress state of homopolymer PVDF dictates the semi-crystalline polymorph content of PVDF. Higher β-phase content (associated with piezoelectric response) of PVDF will be varied using different printing conditions. Variations of F(β) for 3D printed PVDF samples using different deposition parameters was evaluated to determine the parameters influences on the microstructure development and piezoelectric potential of parts.

3.3.4. Infill density

Infill density is one of the processing parameters that has notable effect on the strength and mass of the printed objects, which determines the volume portion of the part

that is filled with printing feedstock material. Different percentages of infill density (100%, 95%, 90%, 85%, 80%, 75%) were used in order to clarify the effect of fill density on the piezoelectric properties. Figure 14 shows the fraction of β-phase in different percentages of infill density. Higher percentage of fill density leads to parts with more crystalline β-phase, which means the fraction of β-phase in the specimens printed with 100% infill density is higher than the others. Increasing the percentage of infill printed material from 75% to 100% will decrease the number of air gaps within the printed samples. Therefore, the piezoelectric properties of FFF printed parts were directly tied to the infill density of printed samples. Although higher percentage of infill density consumes more material and printing time, it produces much stronger components with higher piezoelectric properties.

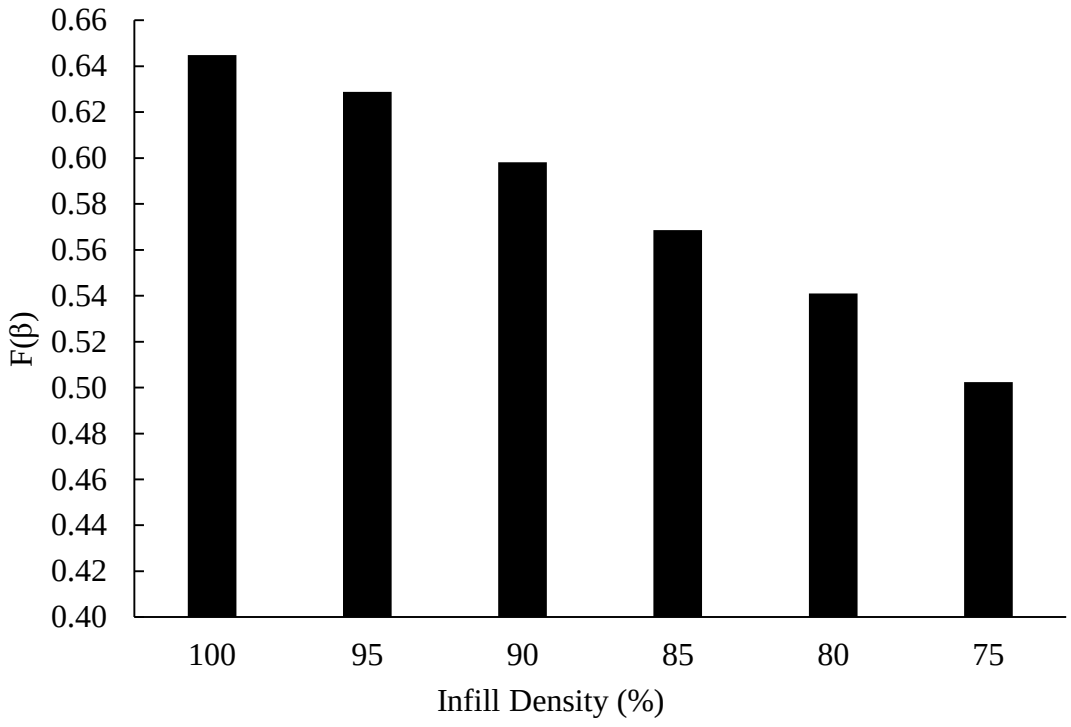

Figure 14.β-phase fraction in samples with different fill densities

3.3.5. Infill pattern

Five different nozzle pathways were used to investigate the influence of infill pattern on the amount of crystalline β-phase within the printed samples. As it is concluded from Figure 15, although triangle and honeycomb had slightly higher amounts of crystalline β-phase than other patterns, the change in amount of this polymorph was minimal. Therefore, internal infill structures did not make a big change on the amount of β-phase fraction within the components.

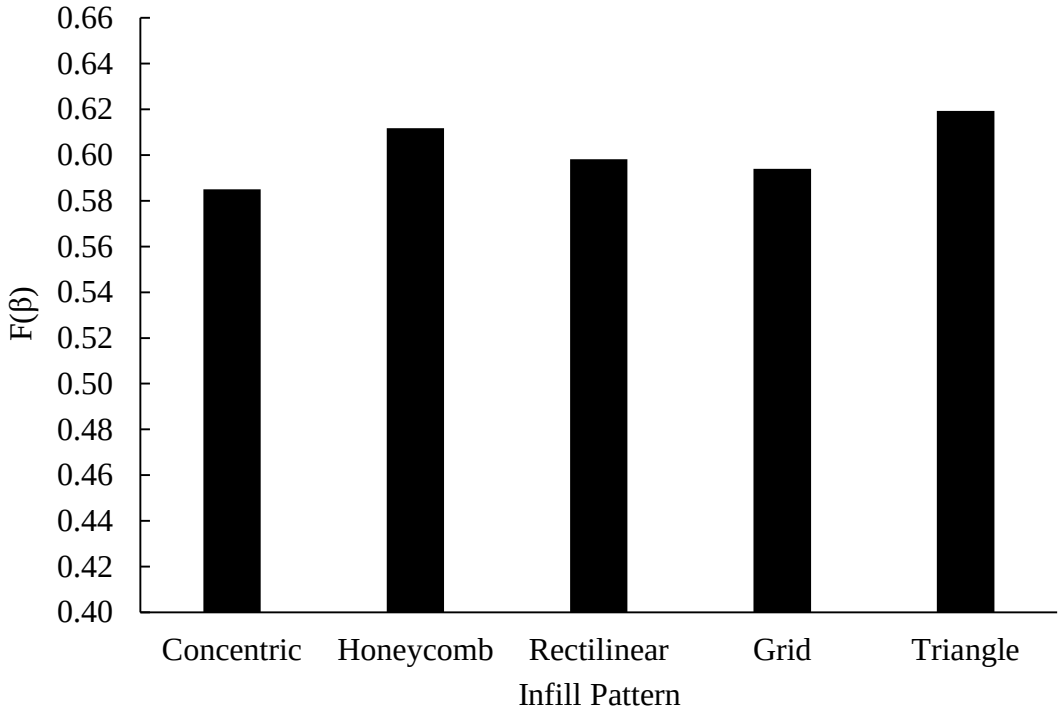

Figure 15.β-phase fraction in samples with different infill patterns

3.3.6. Layer thickness

Since the layer thickness defines the number of cooling and heating cycles during deposition for a given part thickness, it plays an important role in determining the residual stress state and distortion; this in turn affects the semi-crystalline microstructure

development. Thinner layers are predicted to contain larger residual stresses compared to thicker layers, assuming the same thermal disparities between the deposited material and the underlying structure [143]. As shown in Figure 16, thinner layers had higher amount of crystalline β-phase than the thicker ones. In the specimens with 0.05 mm thickness layers, warping (deformations relieving internal stresses) has occurred and this poor adhesion quality between the first printed layer and platform may affect the β-phase content, hence it had less β-phase fraction than the sample with 0.1 mm layer height.

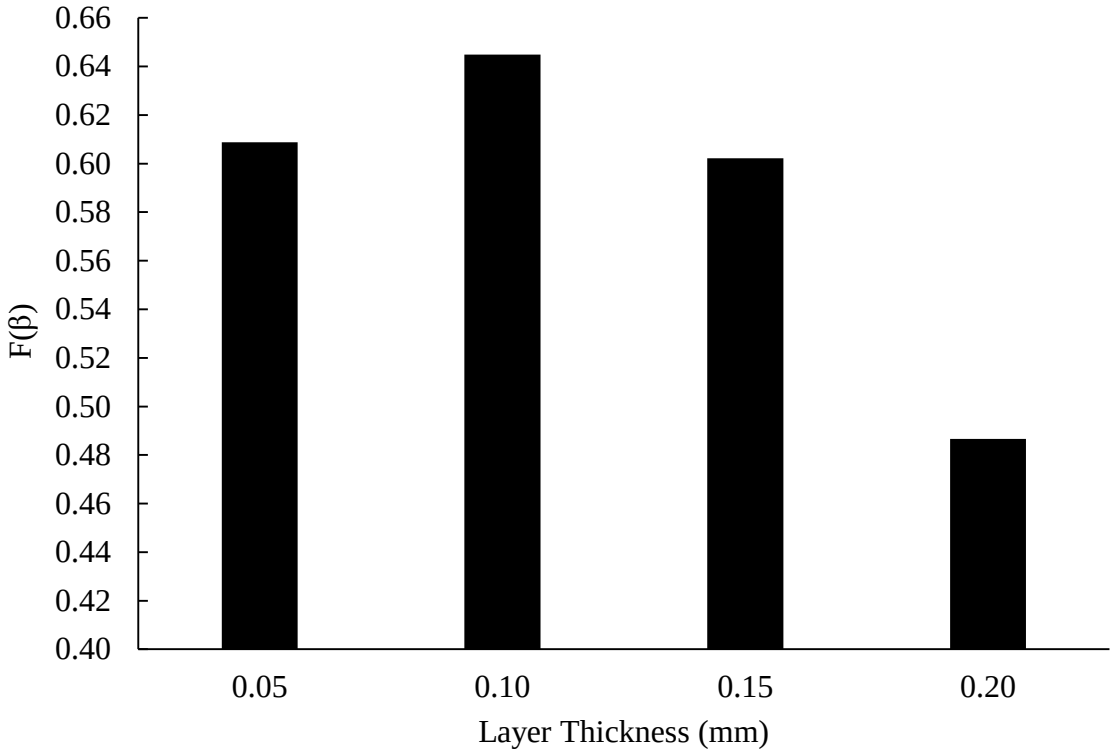

Figure 16.β-phase fraction in samples with different layer thicknesses

3.3.7. Nozzle Diameter

Nozzle diameter is another parameter that was found to have an effect on the amount of β-phase within the fabricated parts using FFF 3D printer. Nozzle diameter

determines the print resolution and affects the speed of printing. In this case, five different brass nozzles with sharp geometry were used to extrude PVDF filament. Figure 17 presents the relation between F(β) and nozzle diameter. According to this plot, the conical nozzles with 0.2 mm and 0.4 mm diameters had higher amount of β-phase fraction than the rest, and there was a drop off in the piezoelectric properties with bigger diameters (0.8mm and 1 mm) which was related to delamination from the print platform in these 3D parts.

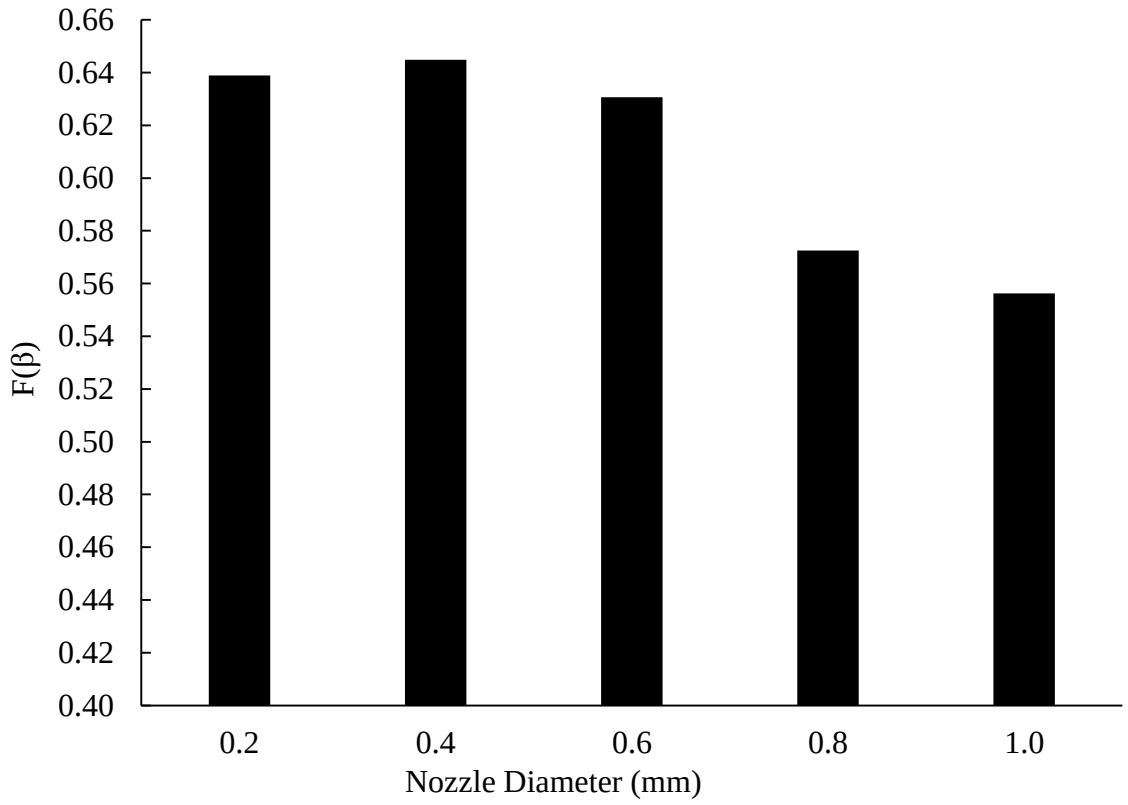

Figure 17.β-phase fraction in samples with different nozzle diameters

3.4. Conclusions

In this chapter, the feasibilty of employing PVDF homopolymer as a multi functional feedstock material for creating different 3D structures was evaluated, and viable deposition parameters are reported. Due to the large coefficient of thermal expansion and higher shrinkage, printing PVDF via Fused Filament Fabrication is more challenging than other common feedstock material in an FFF process. It was found that using a heated build platform, a specimen brim, and a thicker first deposition layer helped to reduced structure warping. The layer thickness had the greatest impact on controlling the warping rate. The semi-crystalline phase and microstructure of PVDF ultimately enhances the piezoelectric potential for additively manufactured PVDF parts. According to FTIR results, the β-phase fraction in final 3D parts is about 3 times greater than PVDF pellets, or this amount in fabricated PVDF samples were 31% and 18% higher than extruded filament and extrudate due to stressing/stretching situation and annealing at high pressure in the brass nozzle.

Moreover, this work investigates the effects of processing parameters of FFF method on microstructure development within additively manufactured parts. Infill density, layer thickness, and nozzle diameter were found to be the most influential parameters affecting the amount of β-phase content in fused filament fabrication PVDF components. The volume fraction of air gap has profound effect on the piezoelectric properties of the 3D printed parts, in which the part with 100% infill density has about 22% higher amount of fraction of β-phase than its counterpart with 75% infill density. Hence, the presence of voids or pores will gradually decrease piezoelectric properties of printed samples, which means that denser parts have higher β-phase content. Layer

thickness, which has a direct impact on warping and distortion issue, is another major factor that evaluated in this research. By increasing the layer thickness, F(ß) decreased. For instance, the fraction of β-phase content for samples with 0.1 mm and 0.2 mm layer height, was about 0.64 and 0.48, respectively. Another way to get higher piezoelectric properties in the additively manufactured parts is related to nozzle diameter, smaller diameter of conical nozzles produced PVDF samples with higher fraction of β-phase than larger ones. The infill pattern was not a significant influencing parameter on the PVDF microstructure. Although triangle and honeycomb had slightly higher amounts of crystalline β-phase than other geometries, the change in amount of this polymorph was minimal.

CHAPTER 4

IMPROVING ELECTROMECHANICAL AND MECHANICAL RESPONSES IN MEAM PVDF USING POST-PROCESSING METHODS AND ADDING PVDF-TRFE

4.1. Introduction

Intrinsic multifunctionality (or smart attributes) demonstrated by certain additively manufactured materials has extended their use beyond just structural applications [144-147]. The multifunctional behavior that smart polymers exhibit, coupled with their natural high-strain tolerance, enables engineers to innovate highly novel designs that integrate load-bearing and sensing/actuation capabilities into a single structure. Though traditional means for preparing piezoelectric polymers have been generally limited to sheets of material, new advances in material extrusion additive manufacturing (MEAM) research have facilitated fabrication of more complex features.

Piezoelectric materials are one of the several types of active smart materials which generate electrical charges when mechanical forces are exerted on them [148]. A variety of potential applications could possibly gain from the addition of piezoelectric properties built into the components. Some could use vibration-based energy harvesting to provide extra power to improve electrical efficiency of a device [149], or use force

detection built within the packaging to monitor a component's structural health [150], or revolutionary custom medical products could be fabricated, such as a knee brace uniquely designed to fit a specific person with enhanced, integrated load sensing capabilities within the structure [151]. This intrinsic property can be found in several man-made and natural materials. Polymers in comparison to other types of piezoelectric materials exhibit unique properties, which can be utilized in vast majority of applications. Although polymers have lower piezoelectric strain constant, they are more versatile for using in sensing mechanism because of their higher piezoelectric stress constant, lower dielectric constant and small density. Polymers are flexible materials, much more durable than ceramics, and can be formed easily. These distinctive features made piezoelectric polymers an attractive and widely studied class of materials [27, 152-155].

The copolymer of PVDF, PVDF-TrFE ($C_4H_3F_5$), has been used to great success in thin film fabrication of piezoelectric layers in MEMS device applications. In specific ratios, the copolymer adds a fluoride group that makes formation of the all-*trans* morphology favorable and specimens exhibit β-phase content upwards of 50%, even when manufactured via melting or upon crystallization from solution. Multiple studies focused on this system report significant piezoelectric behavior, or devices demonstrating functioning actuation or energy harvesting capabilities [23, 156-159].

Multiple studies were investigated the effect of annealing process as post-process method on PVDF microstructure phase transformation. Abdullah et al. [160] by using the X-ray diffraction (XRD) and Fourier transform infrared spectroscopy (FTIR) tests results showed that annealed samples at 60°C and 90°C had the greatest amount of crystalline β-phase. At 30°C both α and β polymorph were exist and at temperatures higher than

100°C, β to α transition occurs within the samples. According to FITR and XRD results, Satapathy et al. [161] observed that maximum increase of β-phase content in the PVDF annealed samples were related to sheets which were annealed at 90°C. Based on their experiment, at higher temperature due to reduction of PVDF viscosity and increment of mobile fraction, α-phase will be increased. Tiwari and Srivastava [162] showed that about 70% of the total crystalline phase within the annealed samples at 80°C and quenching temperature of 20°C was the crystalline β-phase, which was the greatest between other annealed samples. Therefore, temperature and holding time are two main factors in annealing process. Based on thermal history of PVDF, curie temperature, melting point and phase transition of PVDF at different temperature, heating temperature and holing time was selected. Due to phase transition, crystallinity and chain mobility changes in a wide range of heating temperature and holding time, changes in mechanical and electromechanical will occur. These changes can extend the usage of PVDF in different fields.

The pervious chapter suggested the viable deposition parameters for PVDF truly 3D printed components but the mechanical and piezoelectric properties of the fabricated objects were poor. The aim of current research is to improve the electromechanical and mechanical properties of PVDF additively manufactured samples, in order to enhance its sensing, actuation and stability capabilities for different applications.

This section focuses on the effectiveness of using post-printing processing techniques for producing MEAM printed PVDF components with mechanical and electro-mechanical material responses comparable to baseline properties achieved from either MEAM produced parts using costly PVDF-TrFE (on the order of $6,000/kg for

raw material alone) or pure PVDF sheets commercially produced via mechanical stretching. Specifically, the effects of post-printing thermal annealing cycles on MEAM fabricated PVDF are explored, in addition to the use of corona poling to boost electro-mechanical efficiency. Testing performed included characterization of microstructure β-phase content via the Fourier transform infrared spectroscopy (FTIR) technique, standard mechanical tensile testing, and voltage response testing under dynamic loading conditions. Due to the inherent properties of PVDF, improving the sensing, actuation and mechanical properties of printed components not only extends its usability in harsh environments, but also makes it a good candidate for custom designed products in the bio-medical areas.

4.2. Experimental method

Materials and manufacturing conditions

Raw materials used for this project included homopolymer PVDF resin pellets (Kynar 740) and PVDF-TrFE copolymer powder with 75/25% mol ratio, provided by the Trident Plastic Company and Piezotech, respectively. A customized extruder was used to separately convert both the PVDF pellets and the PVDF-TrFE powder into filament with uniform, cylindrical cross-sections with diameter 1.75±0.15 mm. Filament diameter tolerances were measured regularly, as consistent filament diameter is required to ensure successful printing utilizing the fused filament fabrication MEAM process. To account for the possibility of moisture absorption, filaments were dried in an oven at 50°C for about 2 hours prior to printing. The dehydrated filaments were then used to fabricate samples via material extrusion on an open source 3D printer, Reprap Prusa i3 using G-code files produced by Slic3r software.

Rectangular geometry (cantilever beam) samples were selected for printing in this work for performing testing of both quasi-static mechanical response and dynamic electro-mechanical response characterization. All samples had dimensions of 70 mm in length, 10 mm in width and 2 mm in thickness (Figure 18). Previously determined printing parameters found to minimize net shrinkage and warping [163], shown in Table 4, were used to fabricate all specimens (both PVDF and PVDF-TrFE variants).

(a)

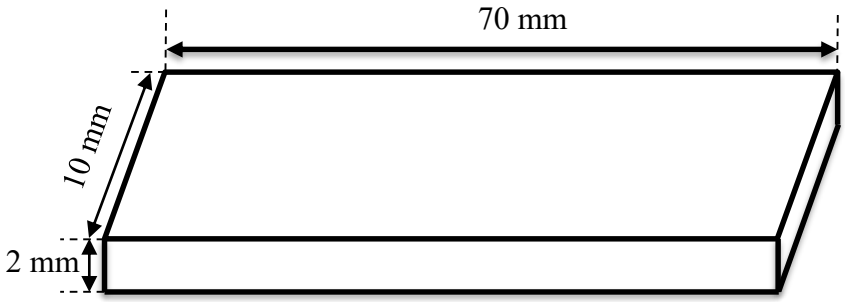

(b)

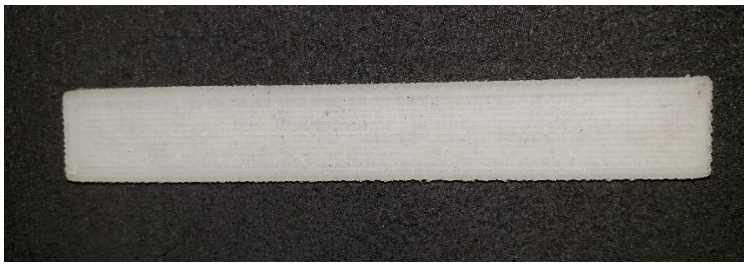

Figure 18. Test specimen dimensions (a) and an actual sample in the testing rig (b)

Table 4. MEAM process printing parameters used for all feedstock materials.

Processes parameters	Viable value
Printing speed (mm/s)	15
Nozzle diameter (mm)	0.4
Nozzle temperature (°C)	220
Bed temperature (°C)	90
Layer thickness (mm)	0.15
Infill density (%)	100

A total of 126 homopolymer PVDF and 6 PVDF-TrFE samples were printed for the experiments in this study. After printing, PVDF samples were randomized and six of them were selected for electromechanical testing; this requires electrode layers to be placed on the top and bottom of each specimen. In this work, 3 μm thick molybdenum electrodes were deposited on both top and bottom surfaces of each sample via sputter-coating on a Kurt J Lesker PVD 75 sputtering machine. Fine gage copper wires were then bonded using a silver epoxy to create a circuit to monitor voltage generated using an Agilent oscilloscope DSO1014A (1 GHz bandwidth). Resistivity of multiple points of the conductive layers were checked with multi-meter before and after testing in order to confirm that the deposited electrode uniformly covered the surfaces. In addition, the calculated sheet resistance of deposited thin film was around 17.8×10^{-3} Ω/sq. The remaining specimens were used for mechanical testing and microstructure characterization.

4.3. Methodology

Thermal treatments

During thermal treatments, the 3D-printed PVDF specimens were placed on a flat tray and placed into a preheated laboratory oven (a GCA/Precision scientific Thelco 26 incubator oven were used as a heating source). Upon completion of the thermal hold cycle, samples were allowed to slowly cool to room temperature by turning the oven off. Printed PVDF specimens were subjected to different temperature levels and varying annealing hold time periods, as indicated in Table 8. In total, 114 homopolymer PVDF cantilever beam samples were printed, with samples being thermally treated under 18 different annealing conditions. Thermal treatment variations examined included 6 different heating temperatures (70°C, 85°C, 100°C, 115°C, 130°C, 145°C) and 3 different holding times (1hr,3hr,5hr). For each condition, 6 PVDF fabricated parts were heated and 6 printed samples were remained non-heat treated to compare its properties with annealed ones.

Table 5.Temperatures/dwell times tested and number of samples for different condition of heat treatment

Temperature (°C)	Non-heat treated	70			85			100			115			130			145		
Time (hr)	-	1	3	5	1	3	5	1	3	5	1	3	5	1	3	5	1	3	5
Number of created PVDF parts for mechanical testing	4	4	4	4	4	4	4	4	4	4	4	4	4	4	4	4	4	4	4
Number of created PVDF parts for electro-mechanical testing	2	2	2	2	2	2	2	2	2	2	2	2	2	2	2	2	2	2	2

Microstructure evaluation

The crystalline phase and β-phase development of PVDF 3D parts were characterized using FTIR spectroscopy with an attenuated total reflectance (ATR) attachment. A PerkinElmer Spectrum™ 100 FT-IR spectrometer was used to determine the infrared spectra for each printed part with 4 cm^{-1} resolution and in the range of 650 to 1500 cm^{-1}. Due to different contact areas between samples and special crystal in machine, all FTIR absorption spectrums were normalized to 1070 cm^{-1} peak [134]. Following various references [119, 164-166], the peaks found at 840 cm^{-1} and 1275 cm^{-1} wavelengths that are uniquely associated with the β-phase were assessed for the different specimens in order to determine the relative amounts of each semi-crystalline phase.

Mechanical characterization tests

Mechanical properties of printed samples were evaluated by tensile testing at a rate of elongation of 1.25 mm/min on a bench-top materials tester. Samples were loaded axially, in a direction parallel to the printed layers. After applying a random speckle pattern on the sample surfaces via spray painting, deformations were measured using a three-dimensional digital image correlation (DIC) system (Correlated Solutions, Inc.). Images of the patterned specimen surface were analyzed using VIC-3D software to obtain the in-plane surface displacement field and average axial strains throughout the loading sequence, as illustrated in Figure 19. In each run, the mean of 6 different virtual extensometers values were used for strain calculations.

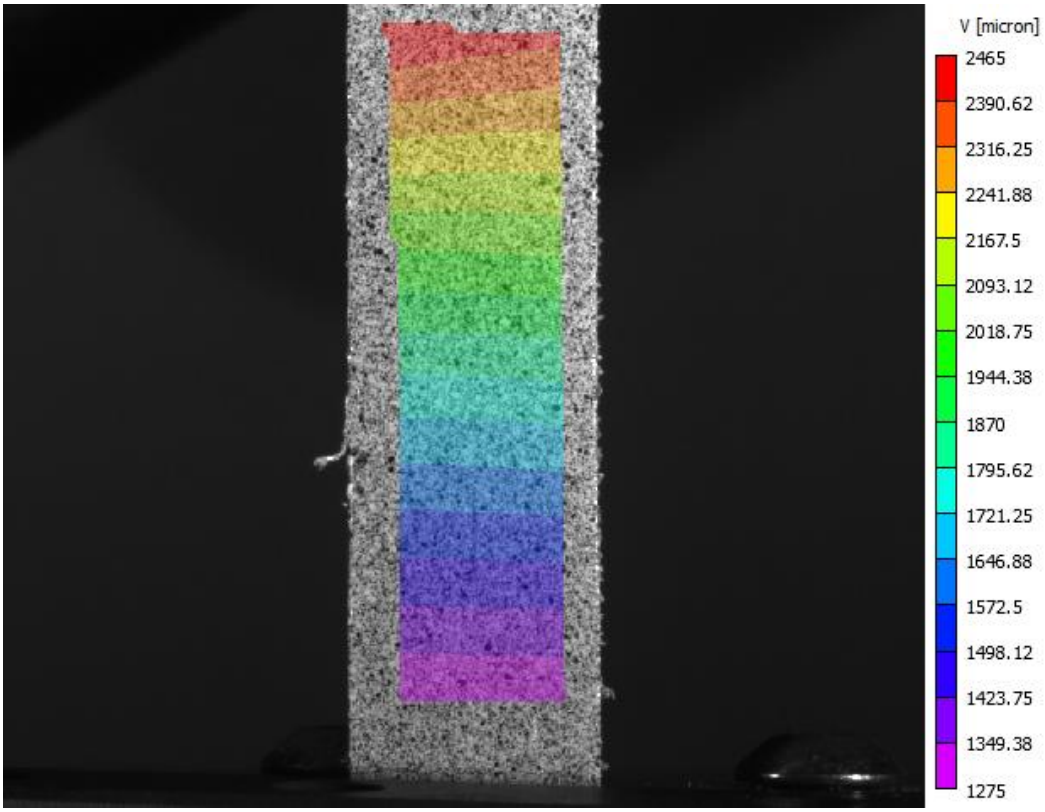

Figure 19. DIC image for displacement in the y direction of PVDF 3D printed sample

Electromechanical testing

The electro-mechanical performance of the MEAM PVDF specimens was evaluated in a basic energy harvesting, dynamic loading application. Samples were fixed as cantilever beams with 8.7 gram as a tip mass (Figure 20), then driven by a custom-made shaker table which equipped with an anchor platform mounted on speaker, amplifier, accelerometer and micro controller. The output voltage produced by each specimen was measured by the oscilloscope with known resistance (Table 8). The applied base excitation was harmonic with the base amplitude set to 0.9 mm and the driving frequency set to 23 Hz, which is about the first natural frequency of the sample (the calculated first natural frequency of the PVDF cantilever beam is 23.6 Hz), and the

output voltage response of the beam was measured by digital storage oscilloscope. The whole experimental setup of the shaker table and the tested sample is shown in Figure 21.

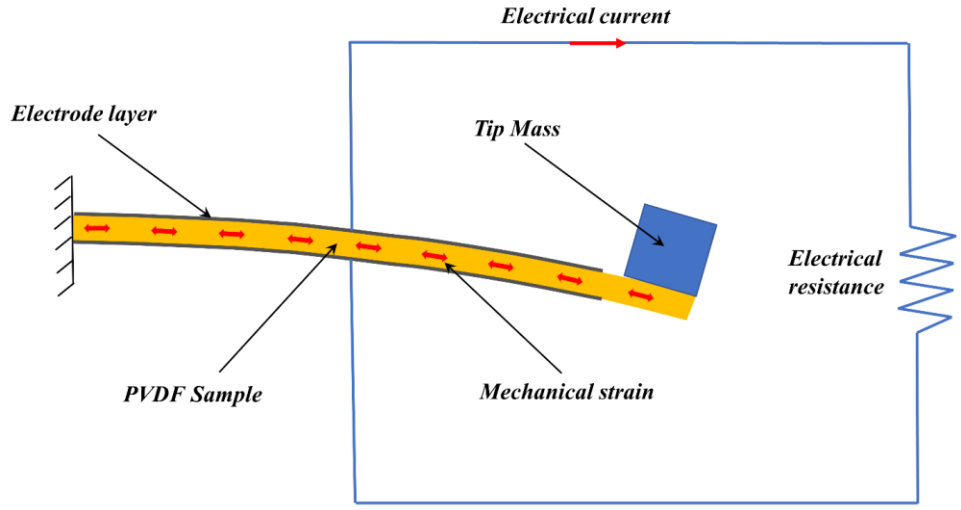

Figure 20. The schematic model of cantilever beam with mass connected to an external electrical resistance.

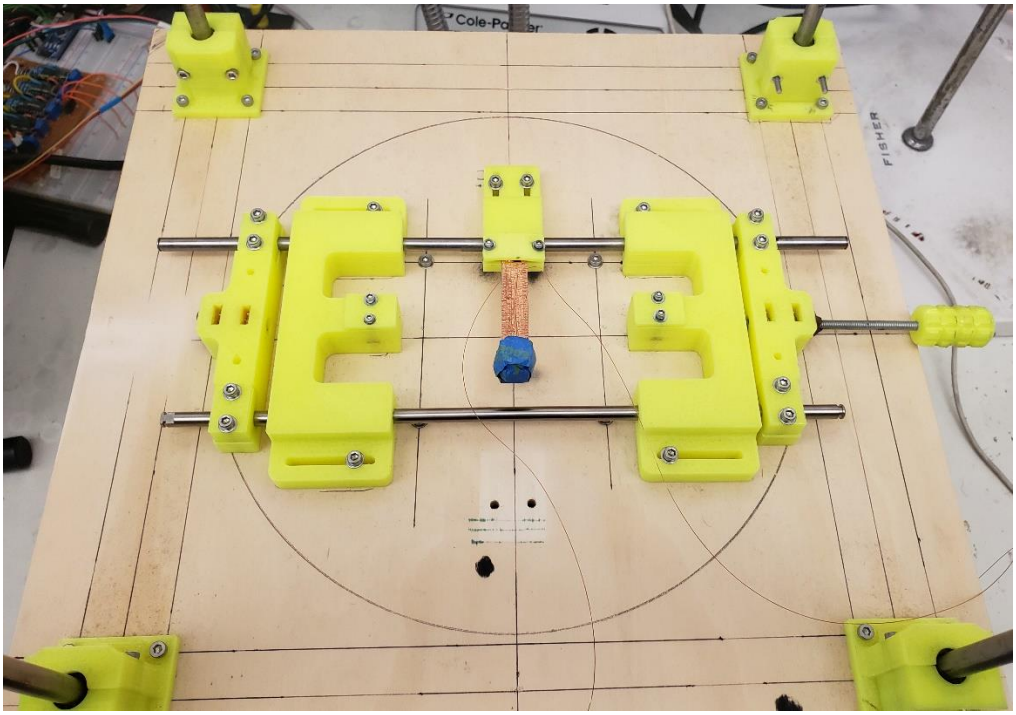

Figure 21. Experimental electro-mechanical testing setup with tested sample

In order to estimate d_{31} coefficient, a single degree of freedom vibrational model was also developed for the experimental setup. The equivalent single-DOF electrical-mechanical equations of motion for the explained cantilever beam could be written as follows:

$$M\ddot{x}(t) + C\dot{x}(t) + Kx(t) + \alpha v(t) + f(t) = 0 \quad (2)$$

$$C_p\dot{v}(t) + \beta_0\frac{v(t)}{R} + \beta_1\dot{x}(t) = 0 \quad (3)$$

where $x(t), v(t)$ and $f(t)$ are the tip mass deflection, output voltage and base excitation force respectively and parameters $M, C, K, C_p, R, \alpha, \beta_0,$ and β_1 are the equivalent system mass, damping, stiffness, piezoelectric capacitance, external resistive load, and electro-mechanical coupling factors respectively. All the experimental dimensions and parameters of the tested samples are shown in Table 6.

Table 6. Mechanical and physical specification parameters

Parameters	E (MPa)	Mass (kg)	Density (kg/m^3)	Resistance (KΩ)	Length (cm)	Width (cm)	Thickness (cm)
Value	1.1	0.00873	8.03497	200	50.10	10.60	2.05

Corona poling

The effects of electrical poling using a custom-made corona poler setup for selected samples was also investigated [7, 167]. A tungsten probe (Ted Pella 0.6 μm radius) was utilized as a needle in the corona poling station and samples were placed on the bed of corona poling station at the distance of about 8 mm from stainless steel mesh grid for about 15 minutes. PVDF sample with thin film (3-micron) of Molybdenum as an

electrode is depicted in Figure 22a and Custom-built corona poling station is shown in Figure 22b. Each sample was placed on platform (on the top of the electrode) for poling purposes.

a) 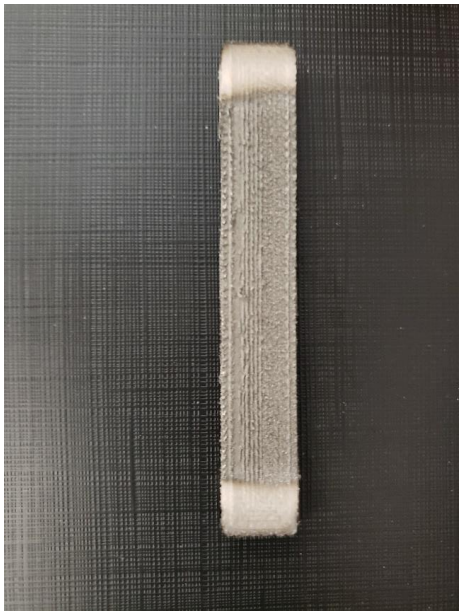 b) 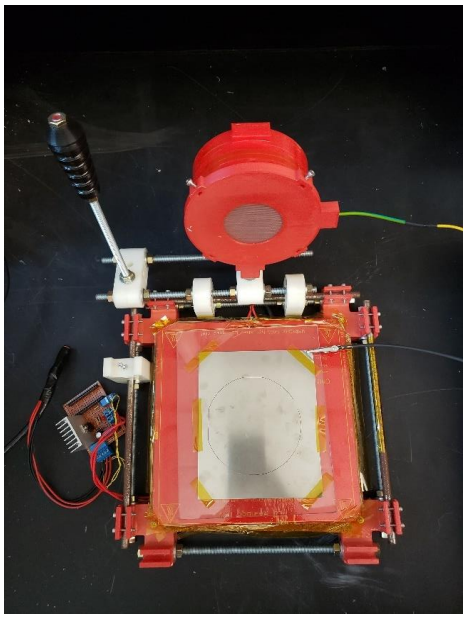

Figure 22. a) PVDF sample with sputter-coated electrode, and b) Corona poling station

4.4. Effects of printing with PVDF-TrFE copolymer

4.4.1. FTIR results

Piezoelectric responses of fabricated samples were evaluated with FTIR spectroscopy and direct measurement of electromechanical response. Moreover, in order to verify the functionality of AM parts, an energy harvesting cantilever beam has been modeled and tested experimentally.

Figure 23 shows the results of FTIR characterization tests for MEAM fabricated PVDF, compared with MEAM PVDF-TrFE and a commercial sheet of PVDF manufactured by mechanical stretching. Higher absorption intensity at 840 cm^{-1} and 1275 cm^{-1} peaks for PVDF-TrFE, revealed that copolymer of PVDF had higher β-phase content and eventually electromechanical responses than homopolymer PVDF both 3D printed part or sheet manufactured.

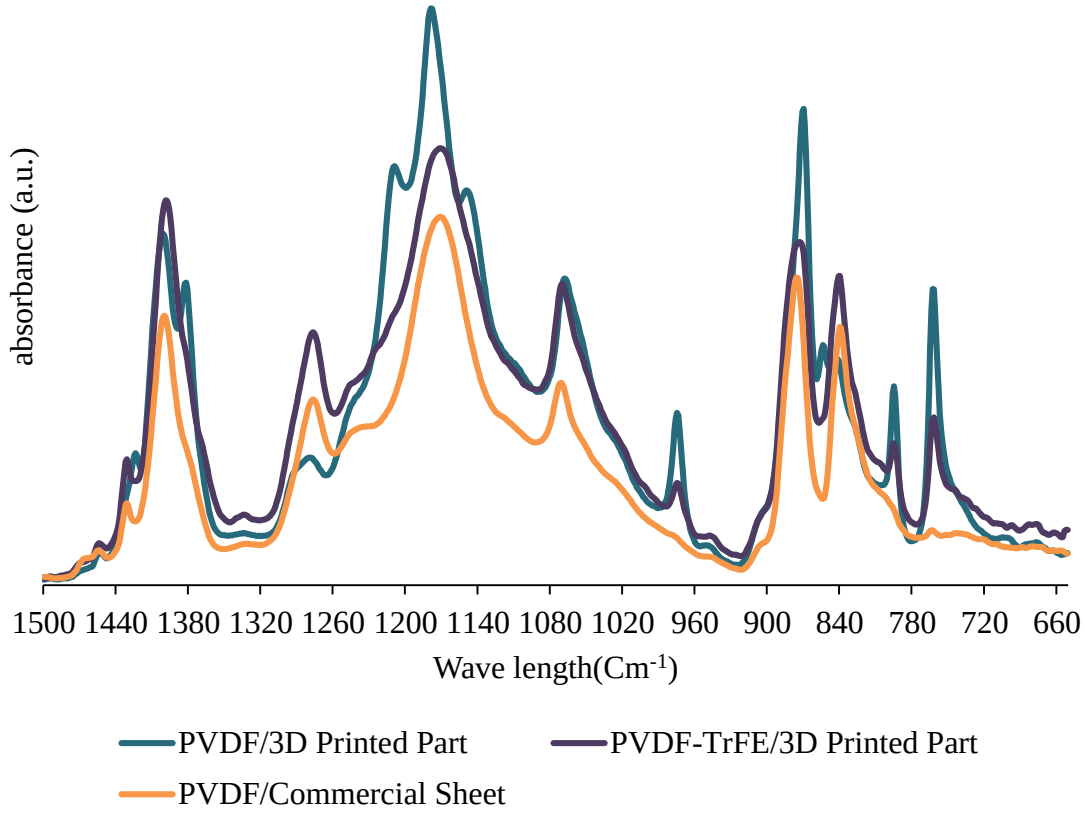

Figure 23. FTIR-ATR absorption spectrum of PVDF and PVDF-TrFE

Effects of post-processing annealing

Electro-mechanical coupling responses of annealed samples (same as PVDF and PVDF-TrFE samples) were evaluated with FTIR spectroscopy. According to the FTIR results (Figure 24), the absorption intensity in the peaks related to β-phase in annealed samples were much higher than as printed samples, so the β-phase formation and effective piezoelectricity is promoted by annealing process. In addition, at annealing temperature around 85°C the β-phase absorption intensity was the greatest. Therefore, samples which heat treated for a given time at 85°C had the highest electromechanical responses between annealed and as printed samples. After that, samples which were annealed at 100°C and 115°C had the highest β-phase peaks, respectively. Due to the different activated phase transitions (such as decomposition of β-phase to other phases) and viscosity reduction at higher temperature, the net relative amount of α phase (as the most stable phase in PVDF) is increased. However, the exact relationship between different annealing temperatures and the amount of β polymorph fraction warrants further investigation to determine the exact mechanisms involved.

Moreover, FTIR characterization test showed that there was direct relationship between annealing time and β-phase content. More β-phase development was occurred at higher annealing times at any heating temperature. Figure 25 shows FTIR absorption spectrum for samples which heat treated at 115°C with 3 different holding time. As it shown, samples which heat treated for 5 hours had slightly higher *β*-phase content in 840 cm^{-1} and 1275 cm^{-1}.

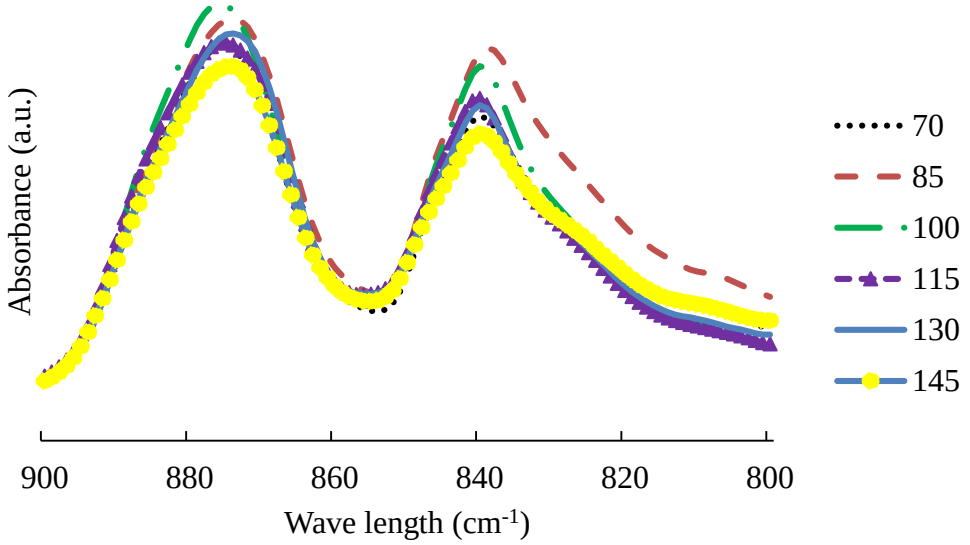

a)

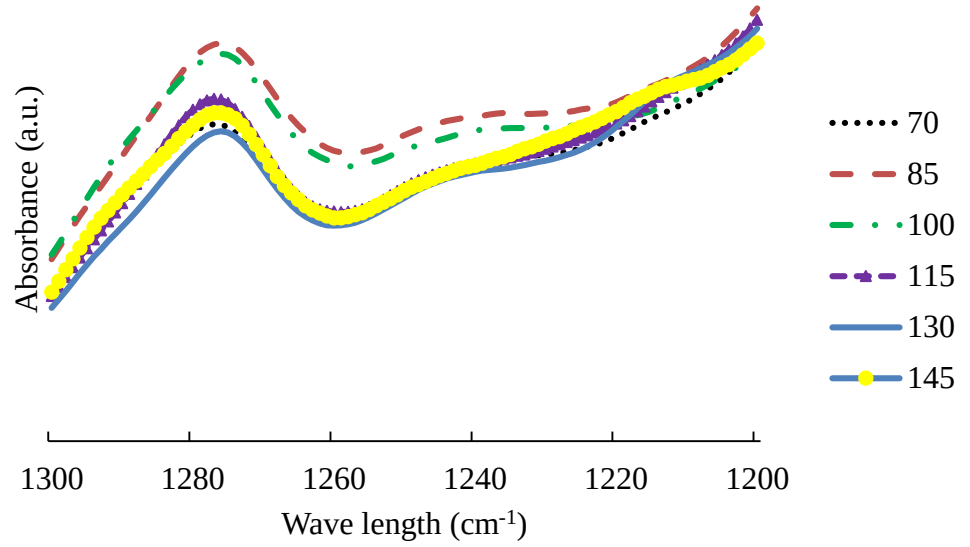

b)

Figure 24. β-phase peaks at different annealing temperature (in range of 800-900 cm^{-1}(a), in range of 1200-1300 cm^{-1}(b) for PVDF samples with the same holding time (3 hours))

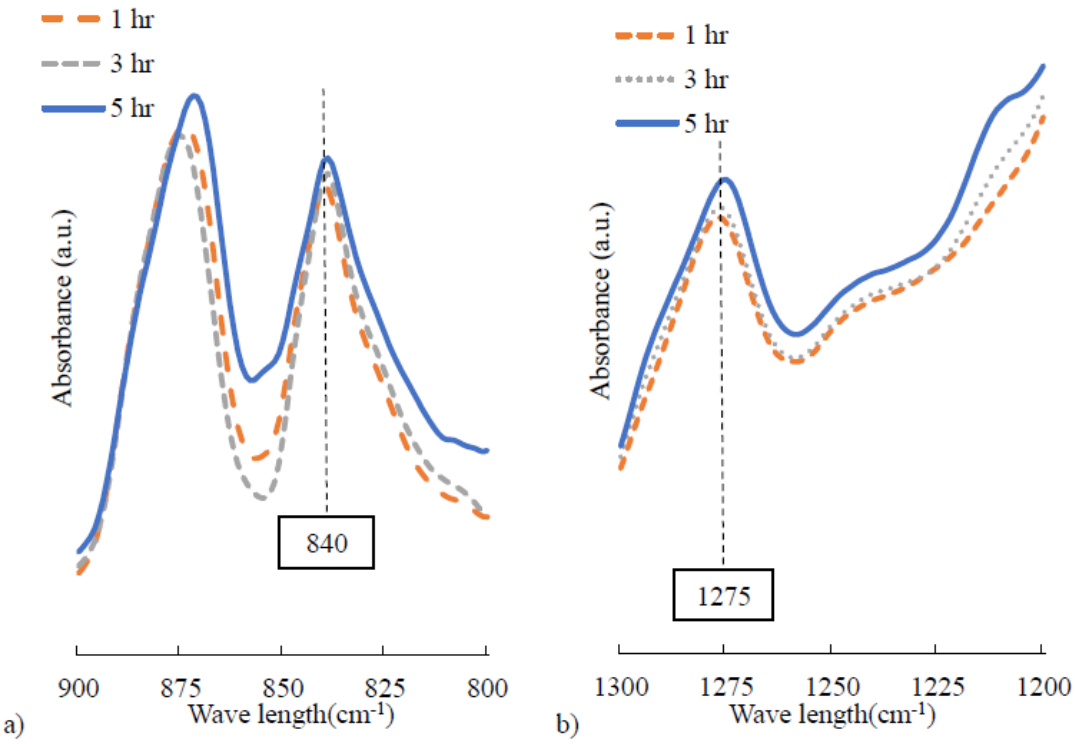

Figure 25. β-phase peaks at different annealing holding time (in range of 800-900 cm^{-1}(a), in range of 1200-1300 cm^{-1}(b))

First reason for improving the electro-mechanical properties of annealed samples is related to recrystallization and reorganization of conformation of polymer during the heat treatment. By increasing the crystallinity of material, piezoelectric behavior is likely to be improved. The α relaxation temperature is around 75°C (less than 85°C), so increment of the temperature up to 70°C, did not help to promote polar phase [161]. Because of the phase transition from α to β polymorph around 80°C within the homopolymer PVDF, β phase fraction and effective piezoelectric responses was greater

in samples which was annealed at 85°C. The β phase content is turned to other phases in temperature above 100 °C. Due to increasing the molecular mobility fraction and decreasing the viscosity at higher temperature, non-reactive phase (α) is developed within the printed parts.

4.4.2. Electromechanical response direct evaluation results

The net amplitude of the output voltage noticeably increased in both experimental and modeling results by about 40% for the PVDF-TrFE sample compared to the PVDF one, Figure 26 and Figure 27. Furthermore, from the developed model, the calculated values for PVDF and PVDF-TrFE samples were $1.4\ pC/N$ and $1.9\ pC/N$ respectively, which shows an increase of about 36% in the piezoelectric properties.

a)

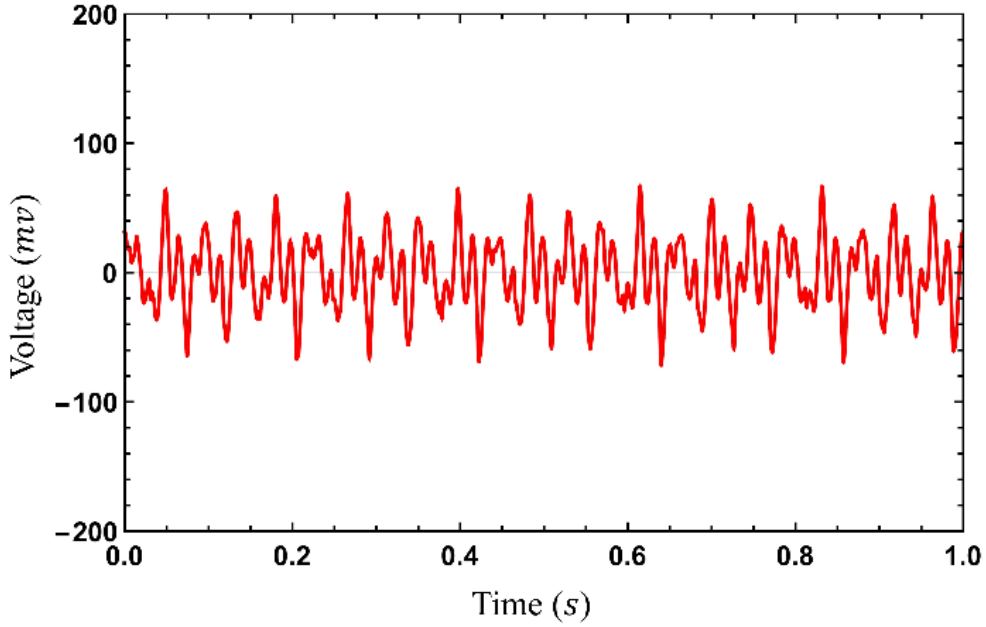

b)

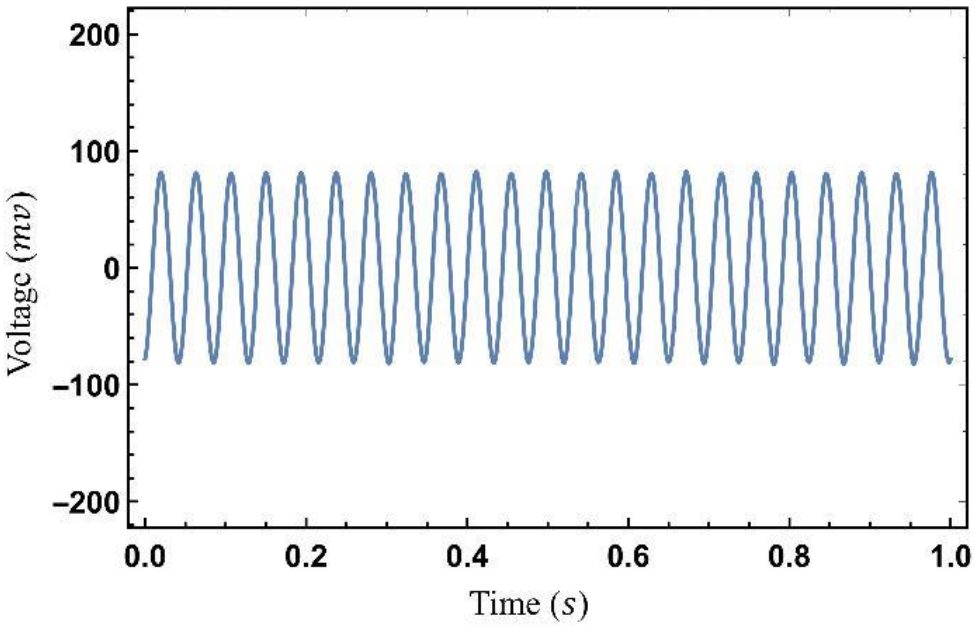

Figure 26. Output voltage response of the PVDF sample: (a) experimental result; (b) modeling result.

a)

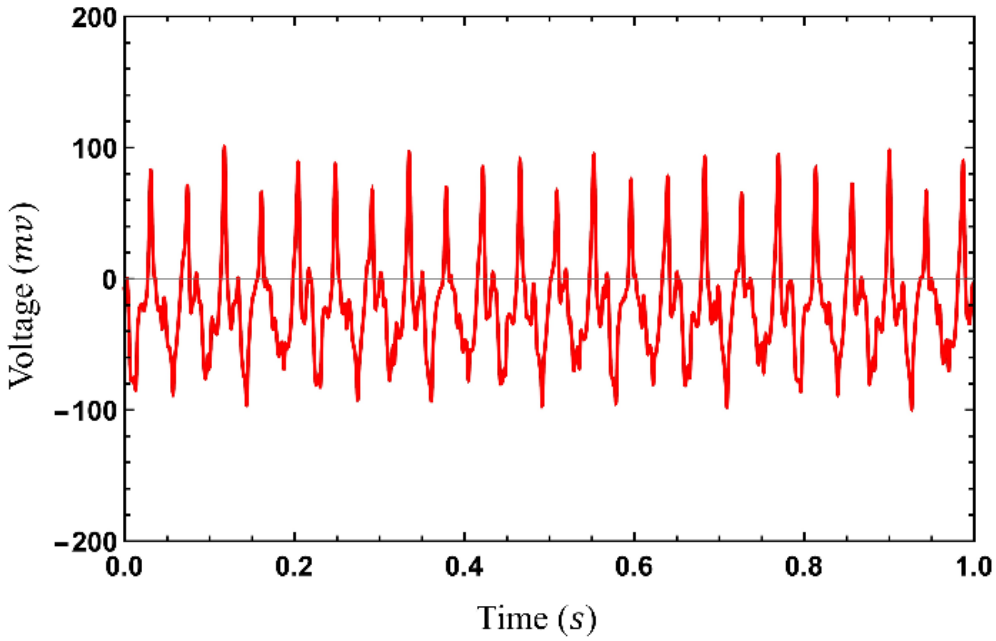

b)

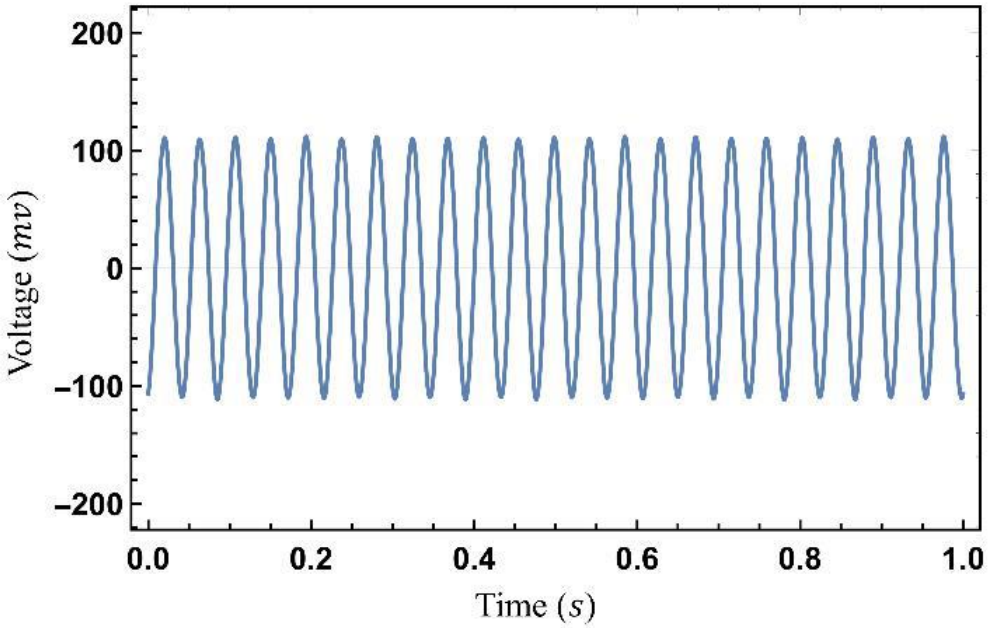

Figure 27. Output voltage response of the PVDF-TrFE sample: (a) experimental result; (b) modeling result.

Experimental results from energy harvesting cantilever beam showed that electromechanical properties of PVDF copolymer was higher than homopolymer PVDF which was match with the modeling results. But due to their proprietary status and limited production scale, it is prohibitively expensive to make entire components out of copolymer systems. Moreover, the mechanical responses of PVDF-TrFE was weaker than homopolymer PVDF. One bright spot is that by employing a dual head extrusion in a MEAM 3D printer system, one could easily print about 95% of a component out of homopolymer PVDF (very cheap and more strength) and limit the expensive specialty polymer deposition to areas where piezoelectricity is desired.

In order to find the effect of post-processing electrical poling field on electromechanical behavior of PVDF printed samples, 3D printed beam specimens were covered by Molybdenum electrode. The coating layer which played as an electrode on the 3D printed components were deposited by physical vapor deposition (PVD) sputter coating process. Molybdenum as a conductive material, was deposited on 2 side of printed samples at 500 watts and 6 MTorr pressure for about 2 hours.

Due to the shortening which limited the applied voltage in contact poling method, corona poling was used to align the dipoles within the fabricated parts. After electrode deposition, electrical poling was performed using a variable (up to 50.0 kV) high voltage source. The electrical breakdown voltage for specimens is determined first, after which additional specimens is poled at lower fields this threshold. The voltage of mesh stainless steel grid of corona poling setup is reached about 22 kV without any arcing. Then, poled specimens were placed on custom-built shaker table for finding and comparing the output voltage before and after poling by the oscilloscope.

Electrical poling aligned the dipoles within the PVDF structure, which helped to enhance net piezoelectric properties of fabricated parts. As it shown in Figure 28, by applying electrical field, the output voltage of a poled PVDF sample a was about 300% higher than that sample when it was not poled. Therefore, due to easy poling setup, electrical poling is one of the methods that can be used to improve the electromechanical behavior of PVDF 3D printed parts significantly.

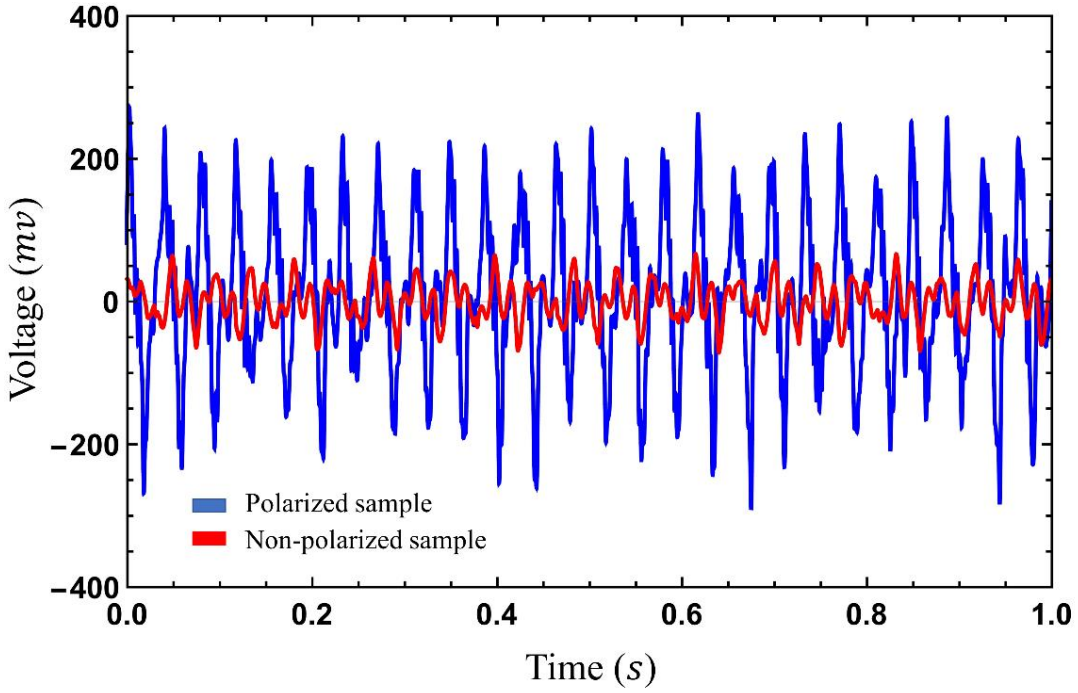

Figure 28. Output voltage of a PVDF 3D printed sample before and after polarization (Poling voltage 22 KV)

4.4.3. Mechanical properties testing

In terms of mechanical responses, PVDF was compared with its copolymer, using tensile tester and DIC system. Modulus of elasticity was found by fitting a line to the elastic region of stress-strain curve derived from tensile testing and DIC results and finding the slope of the line. Young's modules of homopolymer PVDF samples were about 1082 ± 16 MPa, which was higher than PVDF-TrFE with 995 ± 19 MPa. In addition, ultimate tensile strength (UTS) of PVDF is about 5% greater than the copolymer. Elongation to failure of PVDF-TrFE was about 8% lower than PVDF. Therefore, PVDF 3D parts had higher tensile strength and lower strain to failure than PVDF-TrFE counterparts.

The average Young's modulus and UTS percentage difference of isothermal heat-treated samples were shown in Table 7. According to this table, modulus of elasticity and UTS were increased by annealing processes. For instance, Young's modulus of annealed samples for 5 hours at 145°C is improved about 9% than as printed one, or UTS is increased about 19% for same parts. Annealing at higher temperature had more significant impact on Young's modulus than lower temperature and the effect of temperature was much greater than holding time. Same trend was observed for UTS, in which specimens that annealed at higher temperature for greater period were more strength.

Due to changes in molecular mobility during annealing process, porosity and internal defects have been reduced which was a reason for improving the mechanical properties of heat-treated samples. In addition, due to recrystallization in heat treatment process, crystallinity is increased. Improvement in crystallization led to increase on

mechanical performance of 3D printed PVDF samples. Therefore, mechanical responses of annealed parts were greater than as-printed counterparts.

Table 7.Young's modulus and UTS percentage increment of PVDF 3D printed parts at different annealing condition

Annealing Temp(°C)	Annealing Time (hr)	Young's Modulus (MPa)	UTS Increment (%)
70	1	1128	1.4
	3	1139	4.1
	5	1140	5.5
85	1	1130	5.7
	3	1138	7.9
	5	1178	10.9
100	1	1161	8.8
	3	1179	11.4
	5	1183	14.4
115	1	1168	11.0
	3	1180	13.4
	5	1184	15.5
130	1	1177	12.7
	3	1180	15.4
	5	1197	18.3
145	1	1195	13.4
	3	1213	18.2
	5	1239	19.1

4.5. Conclusions

This paper focused on investigating the ways to improve the electro-mechanical properties of PVDF additively manufactured components which may be uniquely suited to facilitate the emergence of new and transformative products. FTIR spectroscopy and direct evaluation test were performed on 3D printed samples and they had shown that annealing process had significant effect on electromechanical responses due to the increasing the crystallinity and decreasing the defects and porosity. Post-heat treatment process had improved the mechanical properties as well, samples which annealed at 145

°C for 5 hours had about 19% and 9% higher UTS and modulus of elasticity than as-printed samples. Electrical poling was another method employed to increase the piezoelectric properties of thick parts of PVDF AM specimens ascribed to the dipole alignments under strong electrical field. PVDF-TrFE had notable impact in terms of electromechanical responses, but due to the economics issues and mechanical behavior was not an ideal material for using a piezoelectric feedstock polymer for fused filament fabricating, unless a dual-head deposition strategy is employed.

CHAPTER 5

THERMAL-MECHANICAL EFFECTS IN MEAM PVDF

5.1. Introduction

Internal stresses which are locked into a manufactured solid part and exist even without external applied loads are called residual stresses. This stress remaining in a body can arise due to non-uniform plastic deformations when mechanical forces are applied, from evolving constrain conditions during cooling-heating cycles, or from phase transformations during cooling process [168, 169]. Residual stress can be valuable or unfavorable depending on its type and distribution. Generally, locations of tensile residual stress are concerning as they can have a detrimental effect on the structural performance of parts, such as decreasing the fatigue performance or increasing crack growth rate. On the other hand, surface compressive residual stress states are desirable and can improve the fatigue life of fabricated objects [168, 170, 171].

Undercutting the few advantages of AM methods, poor dimensional accuracy with respect to the source digital CAD model for some 3D printed parts resulting from residual stress is a significant impediment that limits the usage of additively manufactured objects as end-use parts in commercial applications [172, 173]. Although different mechanical and thermal methods can be used to relieve residual stresses in 3D printed samples [174-177], residual stress formation during the additive manufacturing

process can lead to failed builds due to cracking or print bed debonding. Therefore, the focus of some current research has been dedicated towards understanding the fundamental relationships between the material processing conditions and the resulting residual stress state in the additively manufactured structures in order to overcome these challenges [178-183].

Component warping and unwanted distortion in the 3D printed parts are common issues in 3D printing semi-crystalline thermoplastic polymers via the MEAM method. According to PVT (pressure-volume-temperature) properties of different polymers, semi-crystalline polymers experience larger volume shrinkage between melt and solid transition than amorphous polymers [184]. Volume contraction will influence the stress state in the part, which has a significant effect on the dimensional accuracy and warpage [185, 186]. Apart from shrinkage within fabricated structure when melt solidification is happening, thermal gradients during deposition process typically lead to significant stress accumulation within the part. Due to the layer-wise fashion of deposition for the MEAM process, various heating-cooling cycles happen within each part during fabrication which results in residual strain/stress, warpage and dimensional inaccuracies. [96, 187]. Significant stresses can develop in each build layer plane of filament-extruded components, which can result in a substantial gradient throughout the total height of a build. All of these effects are exacerbated in the presence of non-optimal printing parameters, certain geometrical (aspect-ratio) designs, or specific material properties [188, 189] like larger coefficients of thermal expansion (CTE). 3D Printing of materials which have high CTE is challenging [122, 190]. Due to inherent behavior of PVDF and

its high CTE values, printing this semi-crystalline thermoplastic polymer using MEAM 3D printer contains substantial stresses accumulation and deformations [119].

Depending on the materials involved, different mechanical and thermal treatments can be used to relieve residual stresses produced by additive manufacturing processes. Residual stresses within a part can be measured experimentally by different destructive, semi-destructive or non-destructive measurements, like slitting/contour and sectioning methods (destructive) [168, 191], hole-drilling and ring-core techniques (semi-destructive) [192, 193], X-ray diffraction and neutron diffraction methods (non-destructive) [194, 195]. All of these methods are using indirect ways to measure residual stress [196].

Although some research has been conducted on the theoretical modeling of warping deformations during FFF, limited quantitative studies in this field have been performed [197]. In this chapter, residual stresses within the 3D printed PVDF FFF components with same cross section area but different heights were experimentally measured using slitting/contour method in order to find the relationship between height of fabricated part with rate of warping and residual stress. In addition, part warpage and deformation in printed parts were experimentally measured by digital image correlation (DIC) techniques and were compared with the simulation analyses.

The expected effects of residual stress development within MEAM PVDF are twofold. On one hand, large tensile residual stresses are expected to be detrimental to mechanical performance and to be associated with higher levels of dimensional losses (structure warping). On the other hand, increased tensile residual stresses residing at

surface is expected to potentially increase the β-phase fraction, which is linked with better piezoelectric performance.

5.2. Experimental method

Fabrication parameters were set at suggested values that is mentioned in previous chapters for printing PVDF Kynar 740 samples (Table 1). Since, deformation in MEAM parts has been traditionally observed to be greater at corners and sharp edges, a square cross section part (15mm×15mm) was selected rather than a circle. In order to find the relationship between warpage and height of the samples, 6 different heights of samples were tested (2.5mm, 5mm, 10mm, 20mm, 40mm, 80mm). For each set of height, 5 specimens were produced to measure the residual stress and warpage. These specimens will allow direct comparison of height aspect ratio effects on part stress and deformation.

Deformations in the printed structures were experimentally measured using DIC technique. The bottom, top, and side surfaces of parts were artificially speckled using white and black spray paint. After calibrating the DIC optical system, images of the specimen surfaces were analyzed and the maximum distortion was calculated by finding the average values of the greatest deformations in sides and bottom surfaces of samples for each specimen.

Residual stresses were measured using slitting method [198-200]. This method is an inverse method which measure deformations as a function of slit depth, and then residual stress normal to the cut plane can be found as function of thickness using the measured strains. For this purpose, a pre-wired Omega strain gage was attached to the bottom surface of the samples using super bonder instant adhesive. Before applying super

glue, the bottom surface was cleaned with a solvent cleaner (acetone) to remove any dust or dirt from the surface that strain gauge will be applied. Then, the attached strain gauge was connected to a strain indicator with 1.92 gage factor. Figure 29 shows the attached strain gauge to the center of the bottom surface of one the PVDF 3D printed sample.

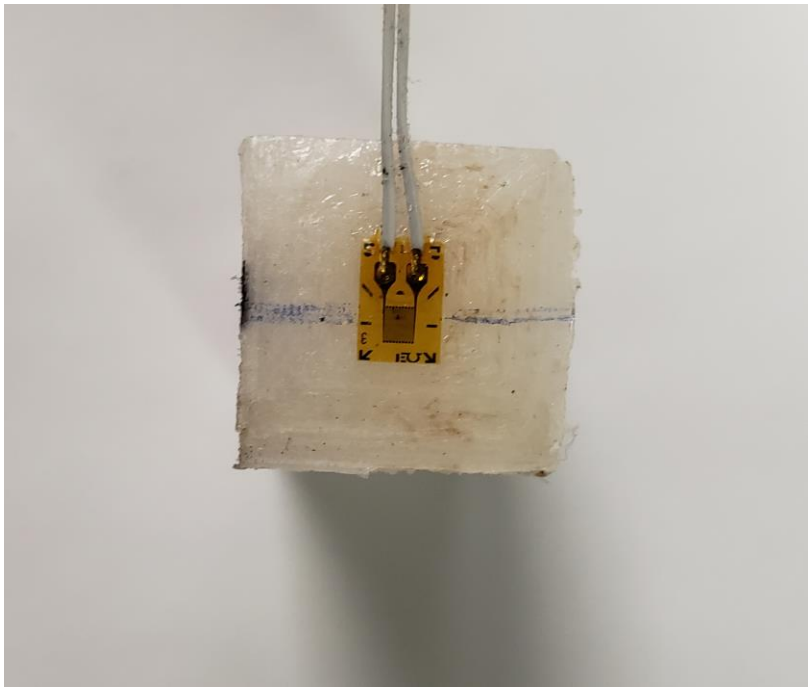

Figure 29. Attached strain gauge to the bottom of one PVDF sample

In strain gauges, any deformation causes electrical resistance changes, which can be recorded by a strain indicator. These kinds of indicators work based on a Wheatstone bridges, which is an electrical circuit that record any small resistance changes, accurately. Changes in resistance can be converted again to micro-strain in strain indicator. Therefore, any deformation in each depth of slit can be found by this setup and it can be a good candidate for measuring strain in different materials. Full, half and quarter Wheatstone bridge circuits are typically utilized to calculate strain changes. In this

experiment, the quarter strain-gauge configuration was selected in the strain indicator to show the values of strain after each slit depth increment. The strain indicator with the connected strain gauge wires is shown in Figure 30.

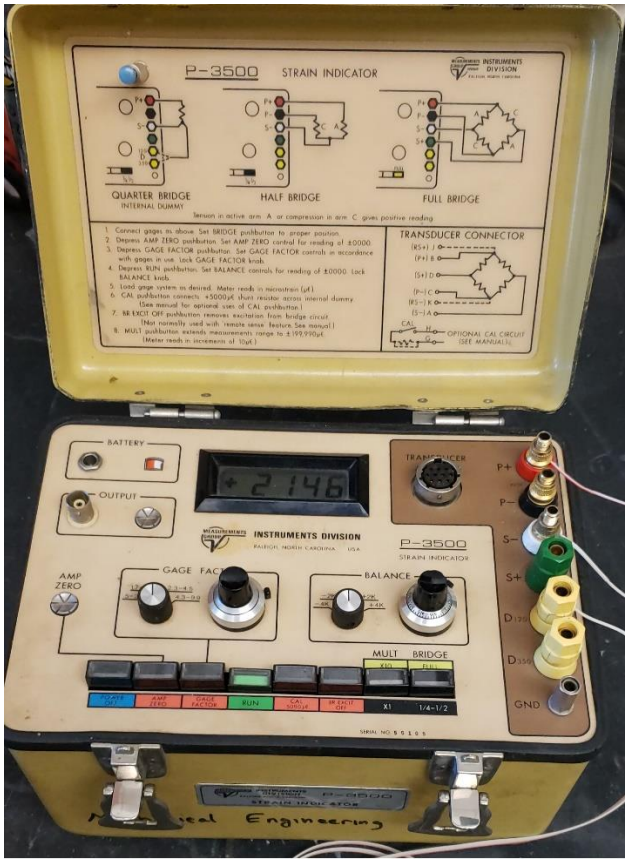

Figure 30. Strain indicator with the recorded strain value for one slit depth

In the slitting method, the part is securely clamped on one side, and the slit is created by using an EDM machine or hacksaw. All samples were cut by a hacksaw in this experiment, two of the sectioned specimens are shown in Figure 31. For each sample, strain was recorded for at least 25 cut increments [201]. As mentioned earlier, this destructive experimental method was performed by incrementally cutting through the components while monitoring the deformations that occur throughout the structure as a

function of slit depth by a strain gage. The magnitude of changes in strain are related to stress relieved, the material stiffness, and the geometry (how deep and far away was that cut increment). Then, residual stress was estimated from recorded strains using ANSYS workbench version 18.1. A static structural analysis was picked as an analysis system, which is necessary to determine the compliance behavior for different specimen geometries. A simulation was performed on half of the model, due to the symmetry for each cut depth. Finer mesh sizes were utilized for the region close to slit, because the deformation in the strain gauge location was important for this experiment (Figure 32). Constraints were applied to the model according to literature (Figure 33) [202-205]. After selecting the proper boundary conditions and finding the created strain (Figure 34) from unit axial pressure for each cut depth, residual stress versus depth results were computed in an iterative fashion. A model like Figure 32 was required for every cut depth of each sample, so based on the number of tested samples, 120 models were run altogether for this experiment.

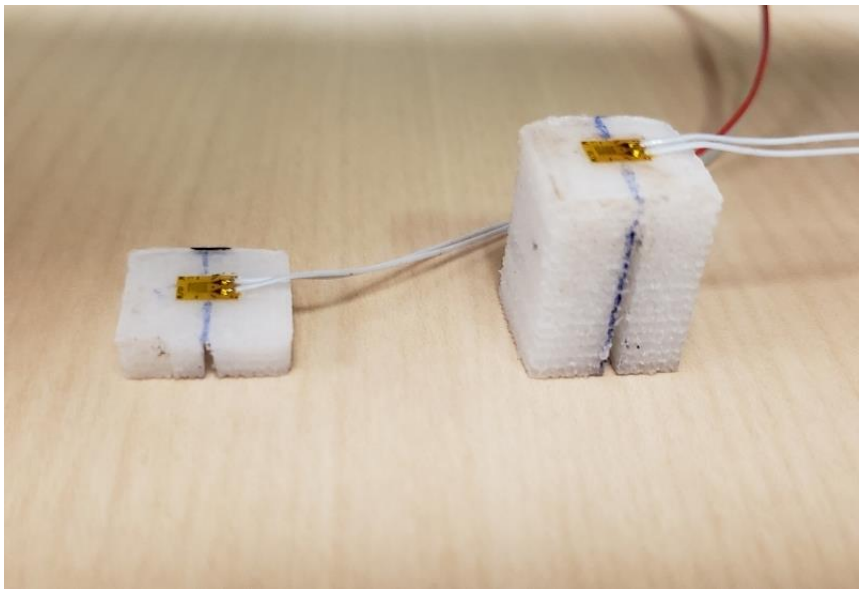

Figure 31. Two of samples were used for slitting method as destructive way to find residual stress

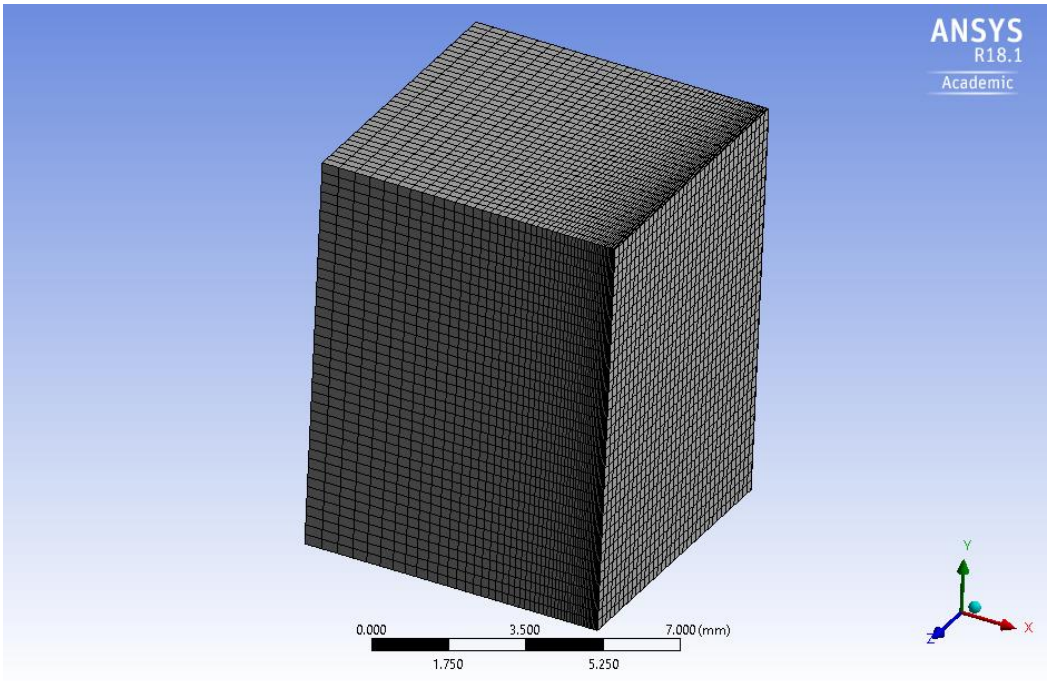

Figure 32. The mesh model of one of the PVDF sample geometries used for residual stress calculations

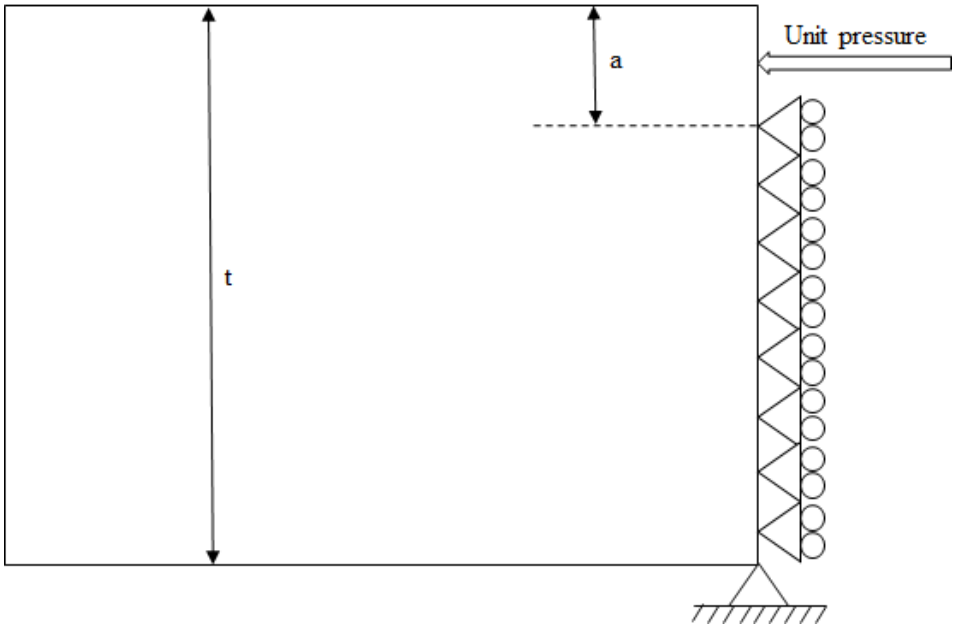

Figure 33. Constraint conditions used along the slit face for compliance calculations performed in ANSYS

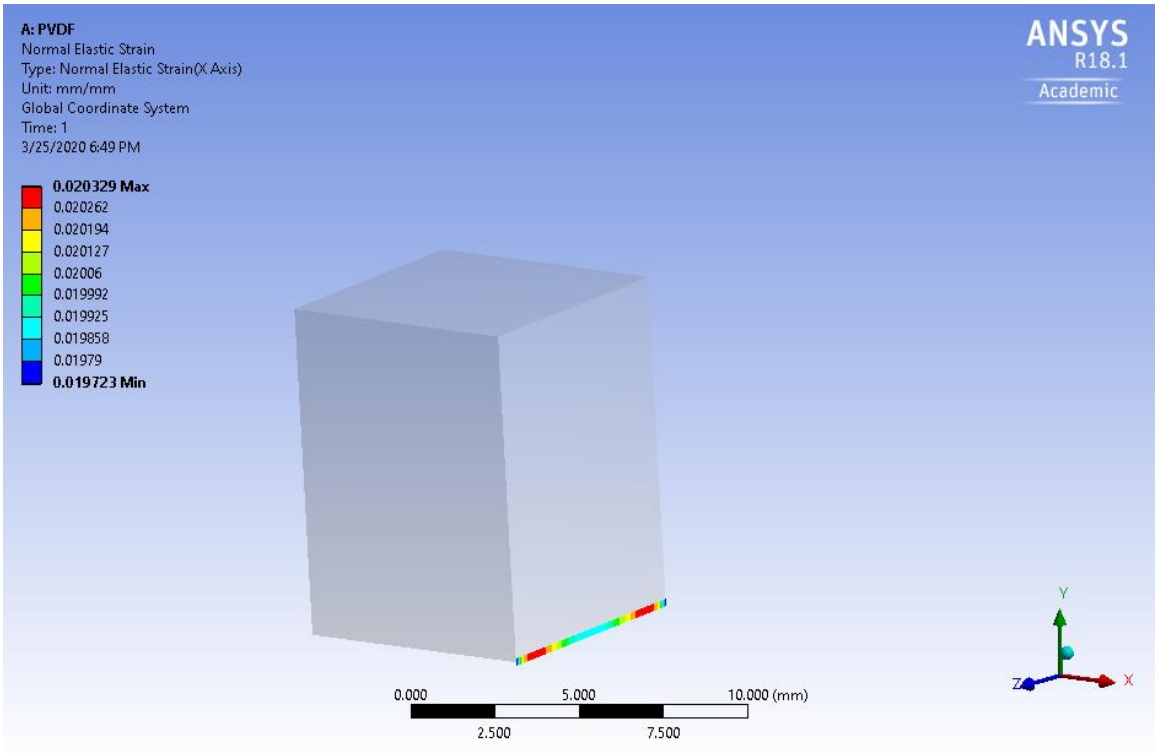

Figure 34. Produced strain by applying a unit pressure on the face of the first cut depth

In addition to experimental measurements, Digimat software was used as a material modeling platform to find component warpage and residual stresses for the different geometry cases. Digimat-AM is the specific software package that was used to perform the multi-scale thermo-mechanical modeling of the MEAM process. Mechanical and thermal characteristics were gathered from PVDF datasheets (Arkema and Solvay) and inserted in the material model definition section of the Digimat-AM software. By inserting the mechanical/thermal properties of PVDF, including Young's modulus, Poisson's ratio, specific volume, thermal conductivity, CTE, specific heat and some other parameters in this software, the FFF method can be simulated. Moreover, by adding the g-code and deposition conditions of a 3D printed parts, residual stress and warpage of the part can be estimated, either by layer or by considering the deposition path used.

Results and discussion

5.3. Thermal Warping

5.3.1. Digimat thermal deformation model

Warping deformations in 3D printed samples are often caused by uneven heat distribution within a part during the printing process and typically lead to significant dimensional inaccuracies in the fabricated components. Adding specific filler particulate material(s) to the feedstock, using optimal printing parameters, heated print bed, cooling fans and environmental chambers are some of the ways that have done by researcher to reduce the warping rate [14, 206-208]. In this section, warpage in printed PVDF samples were measured through experimental and simulation modeling for different height of samples. As there were lots of images (each side, top, and bottom surfaces) at each

sample geometry height, DIC and simulation images for just one representative height (10mm) are depicted in this chapter, and just the final results for other samples are shown in Table 8. Figure 35, Figure 36 illustrate the total deflection found on the top side and bottom side of the sample, respectively.

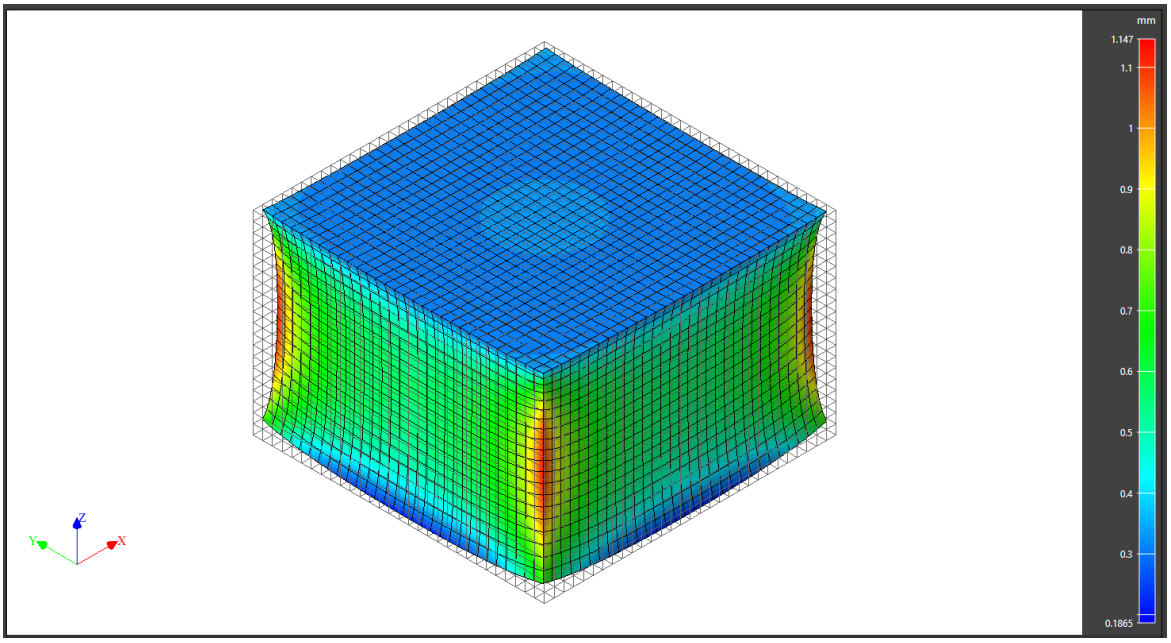

Figure 35. Total deformation of sample with 10 mm height using Digimat - top side (max value=1.147 mm, min value= 0.186)

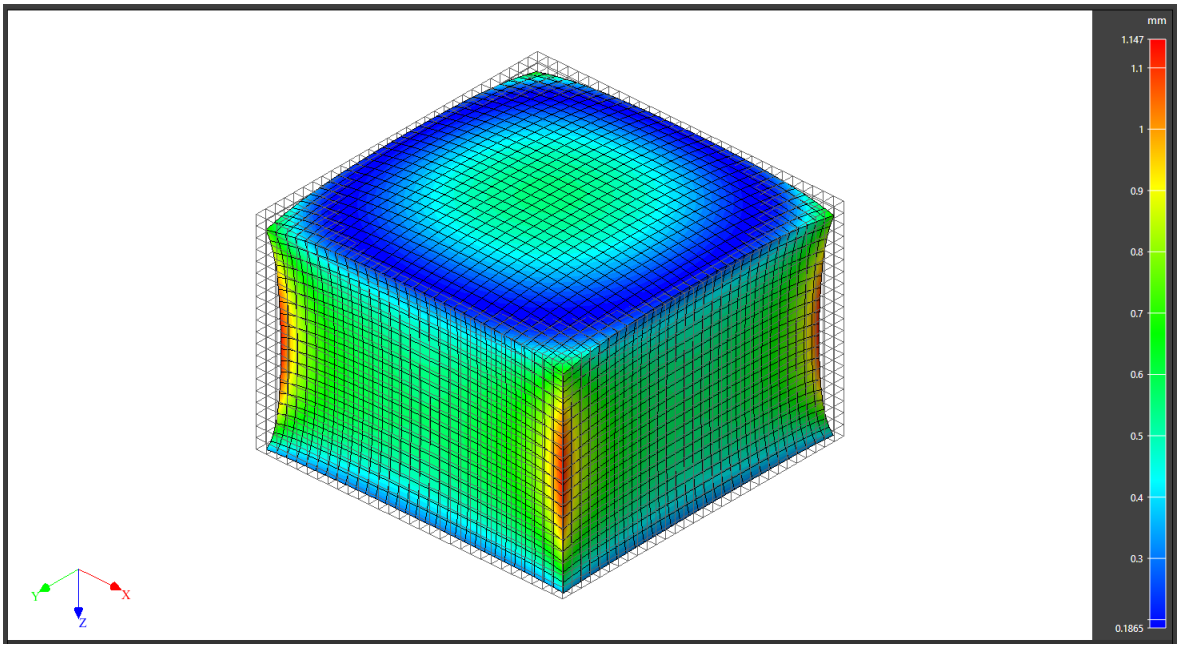

Figure 36. Total deformation of sample with 10 mm height using Digimat – bottom side (max value=1.147 mm, min value= 0.186)

As was expected, the corners of the part had the greatest total warpage (about 1.15mm) in the printed MEAM sample. Due to the lack of constraint and growing residual stress in the build direction as more layers are added, eventually thermal stress in the corners leads to debonding with the print bed (peeling up). Part deflection in just z-direction is presented in Figure 37.

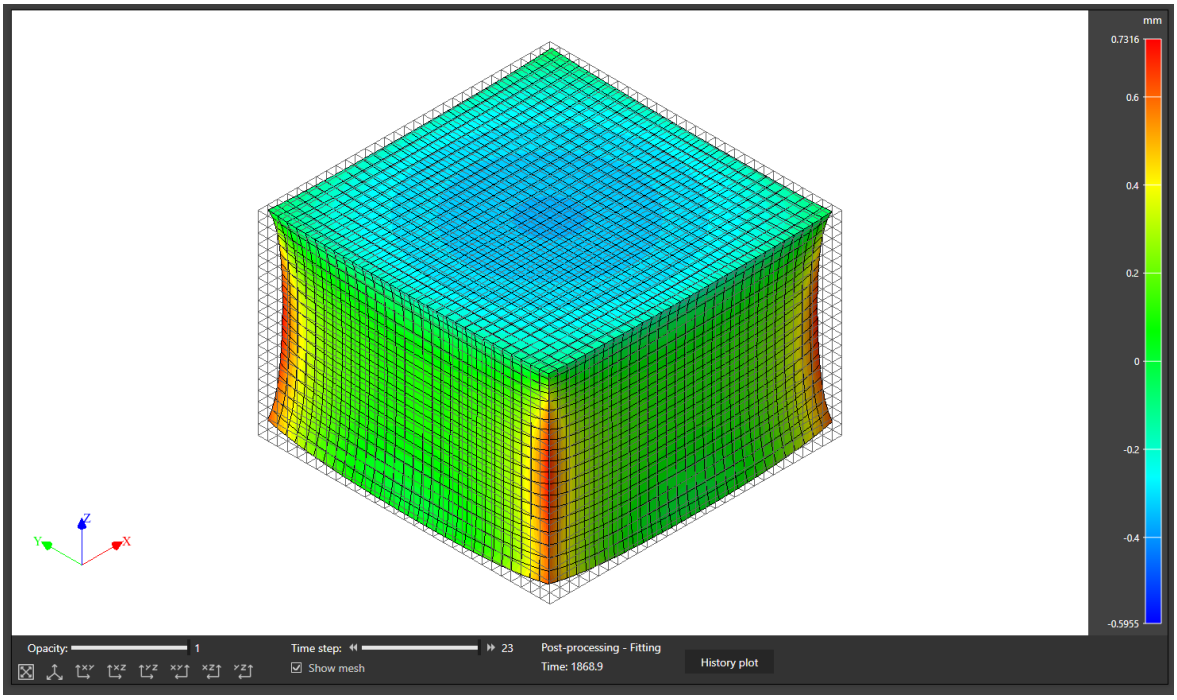

Figure 37. Deflection in Z direction for part with 10 mm height (deflection at corners of the part = ~ 0.73mm)

Deflection in z-direction at the corners of the part was much higher than other section of the part, same as total deformation. So, the measured warpage with Digimat-AM software for PVDF MEAM samples was around 0.71 mm. As a comparison between the un-warped and warped digital parts, and .STL model from both Solidworks and simulation model is shown in Figure 38.

Figure 38. Comparison between CAD file (left) and warped model (right)

The left part is the CAD model and the right part is the warped part. As discussed previously, warpage in the corners was much higher than for other locations within the part.

5.3.2. Thermal deformation measurements using digital image correlation

To perform the non-contact digital image correlation (DIC) method to quantify surface deformations, first the areas of interest (bottom, top, and side surfaces) of the fabricated samples were speckled patterned with spray paint. After doing the DIC system calibration, different images of each surface was acquired. Images for a sample with 10 mm height are displayed in Figure 39 and Figure 40.

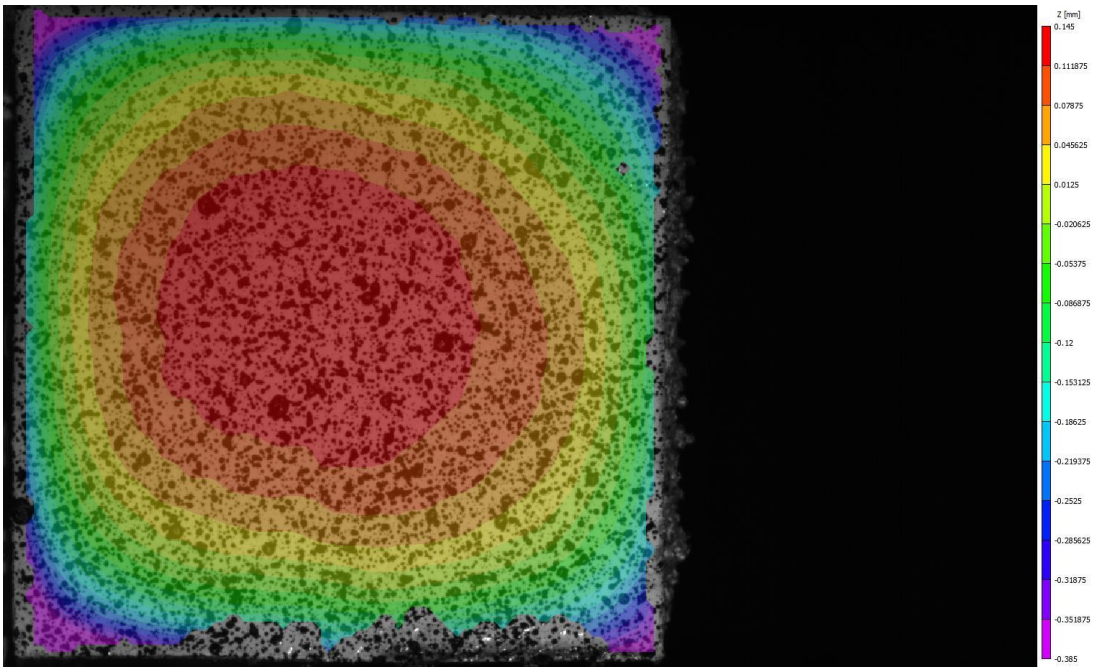

Figure 39. DIC image from bottom surface for sample with 10 mm height (max value=0.145 mm, min value= -0.385)

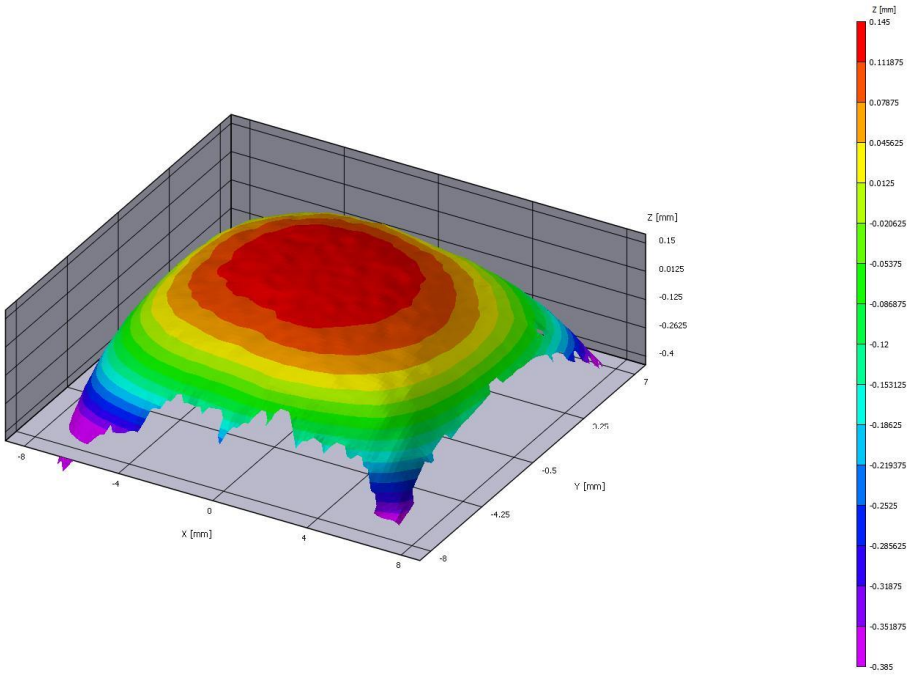

Figure 40. 3D deflection image created by DIC Vic 3D software for sample with 10 mm height (max value=0.145 mm, min value= -0.385)

By using Vic 3D software analysis tools and creating different inspection lines on the part (side to side and diagonal lines), a deflection equation for the bottom surface of the part was obtained (Figure 41). Apart from probing the warpage, information from this figure can be used for creating a plot surface from bottom surface using different plotting software for comparison purposes.

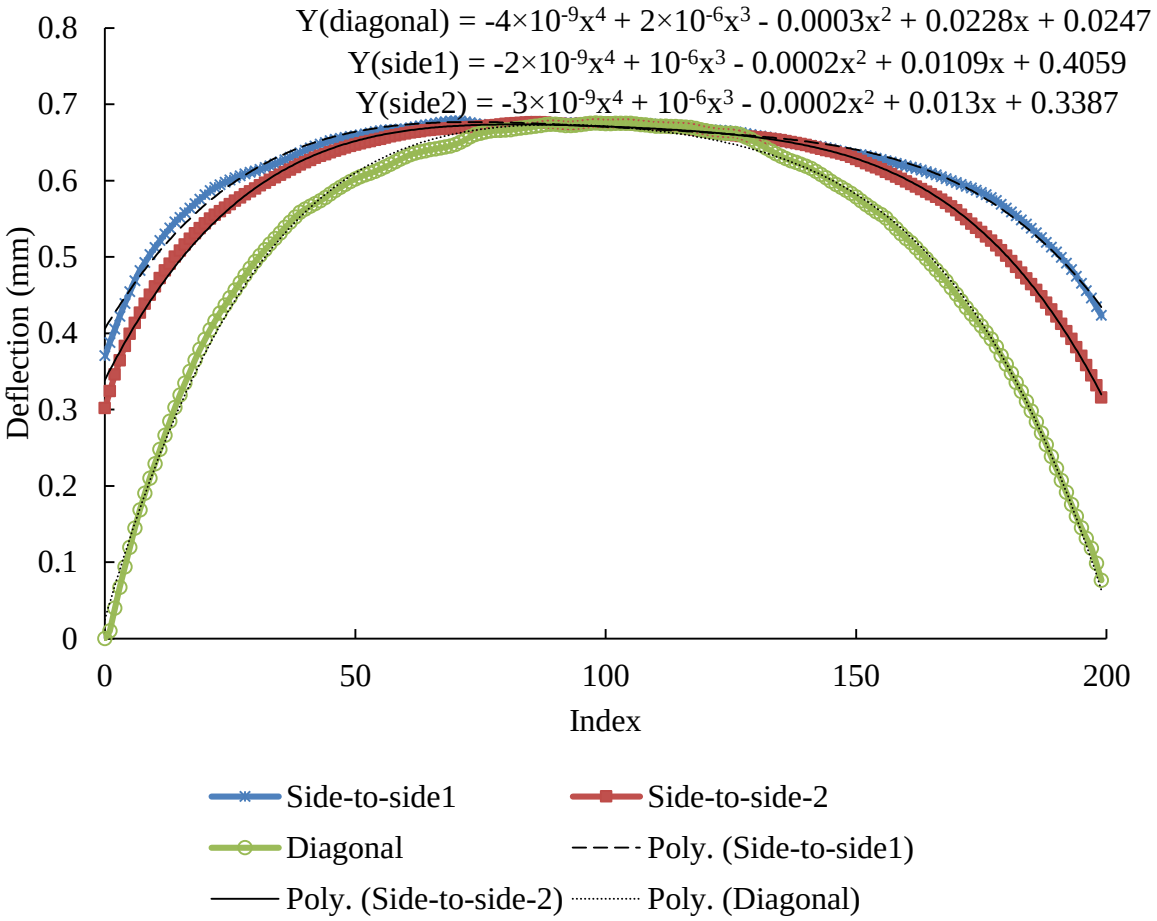

Figure 41. Deflection fit equations for side to side and diagonal lines in the bottom surface

Final warpage for all samples using simulations and experimental results is shown in Table 8. Unit of all values in this table are mm, and the average warping from experimental results were obtained from both side and bottom view of samples.

Table 8. Measured warpage from simulation and experimental results for different height of samples

Height (mm) / Method	2.5	5	10	20	40	80
Simulation result	0.46	0.48	0.73	0.85	0.80	0.73
Experimental result (Mean value)	0.45	0.53	0.66	0.84	0.69	0.67

As it is concluded from both experimental and simulation results, samples with 20 mm height had the largest warping rate than the other samples. Since printing parameters were the same for all of samples, thinner specimen (2.5 mm, 5 mm and 10 mm height) had smaller number of created layers, so these samples experienced fewer heating and cooling cycles. Therefore, warpage in these samples were less than sample with 20 mm height. Although, thicker samples (40 mm and 80mm height) had more successive heating and cooling cycles during fabrication, and thus more expected residual stress, the total warpage was not found to increase monotonically with height. This effect was attributed to the increased bending stiffness for these geometries and differences in thermal conduction, compared to the thinner specimens [209].

5.4. Residual stresses

5.4.1. Digimat residual stress model

Non-uniform thermal gradients during 3D printing are the primary source of residual stress in MEAM parts. In this section, experimental and simulation approaches were employed in order to figure out the distribution and magnitude of these stresses for MEAM PVDF. Simulation and experimental results for all samples shown in Table 9. Simulation modeling conditions used for residual stress were the same as for the warpage measurements. The in-plane residual stress (von Mises stress) within the center of the top surface, for instance within the sample with 10 mm thickness was found to be about 55 MPa.

5.4.2. Residual stress experiments using slitting method

For the slitting method residual stress tests, a hacksaw was used to cut a thin slot in the sample, while deformation on the bottom of the specimen for each different depth of slit was measured through the attached strain gauge. All recorded data was inserted to ANSYS to solve for the average residual stress profile normal to the face of cut as a function of slit depth. For instance, the recorded strain for the first cut depth (a_1= 0.75 mm) was about 285 με. By applying the boundary conditions to the model (Figure 33) and unit stress (1 MPa) to the cut surface in negative direction of X axis, strain on the bottom surface was found to be -40 με. By calculating a simple ratio, the residual stress for first cut depth was about 7.14 MPa in positive direction of X axis. For the second cut depth (a_2= 1 mm), the unit stress was applied to the new cut surface (a_2-a_1) and same procedure was used. The calculated residual stress for the second cut depth was about 11.89 MPa; these calculations were done for each cut depth of part. Last cut depth was at

8.25 mm from the top surface and residual stress associated with this cut depth was about -1.86 MPa. Figure 42 shows the average residual stress found at each different cut depth for the sample with 10 mm height, in addition to a polynomial fit to this data.

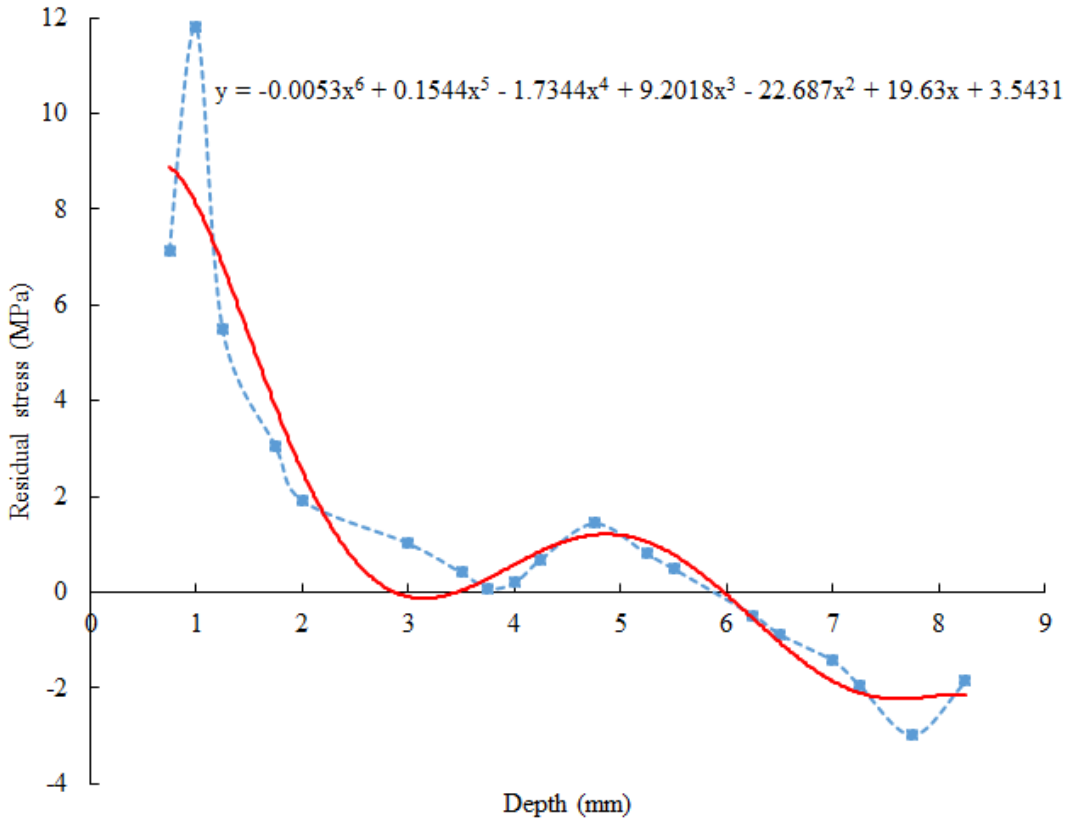

Figure 42. Residual stress vs depth profile resulting from slitting method for sample with 10 mm height

The first and the last strain values were recorded at 0.75 and 8.25 mm cut depth, respectively. Therefore, the residual stress vs depth profile was plotted for sample between these two depths. As it is shown, both compressive and tensile stresses were released by cutting the part. Although, the overall force/moment balance requires that integrating the area under the positive and negative sides of the curve should sum to zero,

the last 10-20% of the cut depth values were unknown or less reliable, so that could make the stress-depth curve of this test reasonable.

In this measurement, just the back strain gauge was used, which gives accurate strain results for about 5% to 95% of the part thickness. All of the cut depths used in this experiment fall within this range. In all printed samples, the magnitude value of residual stress never passed the yield stress that found in the previous chapters from quasi-static stress strain curve. The maximum residual stress from slitting method and simulation modeling is shown in Table 9.

Table 9. Maximum residual stress (both experimental and simulation) for all printed samples

Height of samples (mm)	2.5	5	10	20	40
In-plane Residual stress (simulation Results)(MPa)	10	26	55	92	104
Maximum Residual stress (Experimental method)(MPa)	-	7	12	23	28

Because the height of sample was really small, residual stresses for the sample with 2.5 mm height was hard to measure using slitting method. Therefore, no value was computed for this specimen. As expected, both simulations and experiment showed that adding more layers to the part increased the residual stress level. It is obvious that by adding more layers, the heating and cooling cycles will be increased which result in increasing the residual stress in the part.

Although the general trend for both simulation and experimental results were the same, there was a differences between these values for each part. The main reason for the

differences is related to the fact that slitting method can get only about 15-20% of the actual values, so the experimental results should be much lower than simulation results. In addition, in the simulation results, the von Mises stress residual stress was found for each sample and a von Mises stress includes all the stress components (and will be higher if other components exist), versus just a normal stress that we measure in the surface plane experimentally. Moreover, crystallinity behavior of PVDF was not inserted to Digimat software. Adding the crystalline material model may help lower the residual stress value, basically the β-phase forms to help reduce the strain energy when it is highly stretched. Also, the residual stress experimental measure is an average across the whole specimen, which will give a lower value.

5.5. Conclusions

In the present chapter, part warping and residual stress were measured experimentally using DIC technique and slitting method, respectively. Then, experimental results were compared with simulation models results of Digimat software and it was observed that the general trend for both warpage and maximum residual stress between different height of printed structures were the same. Thicker parts have greater cooling and heating cycles than thinner parts, which results in more thermal gradient and residual stress in the taller 3D printed parts. But instead of a monotonic relationship between warping rate and height of printed parts, warpage had a greatest value at parts with 20mm height and it is decreased afterwards for thicker 3D printed objects (like samples with 40 or 80 mm tall hights). Thermal conduction through the specimen is the main reason for increasing the bending stiffness and reducing the warping rate in the taller printed samples.

In addition, results from both experimental and simulation methods showed that residual stresses on top surfaces were higher than bottom surfaces in the PVDF structure; this had direct relationship with the amount of β-phase fraction on those surface. Because FTIR results revealed that the absorption intensity of top surfaces had greater values than bottom ones at 840 cm^{-1} and 1275 cm^{-1}.

CHAPTER 6

INFLUENCES OF ZIRCONIUM TUNGSTATE ADDITIVES ON MEAM PVDF

6.1. Introduction

Thermoplastic polymers are the most popular choice of commercially available MEAM filament feedstock materials. Amongst all the potential polymer feedstock materials, few options currently exist for depositing “smart” materials demonstrating additional capabilities such as piezoelectricity, shape memory effects, pyroelectricity, etc. The reasons for this are twofold. One, typically multifunctional materials require a highly controlled processing environment to produce the desired properties. Secondly, numerous inherent difficulties exist in simply fabricating basic materials through MEAM methods with a level of structural integrity comparable to that found for traditional manufacturing means like casting or injection molding. As primary challenge in this respect is the degree of warping and residual stress that can develop within MEAM components as the printed structures reach thermal equilibrium after cooling from the required elevated deposition temperatures.

Filament-based deposition fabrication techniques hold great promise for creating piezoelectric PVDF, as the stresses generated in the material deposited via these methods in some ways mimics the established mechanical routes of creating high β -phase content PVDF microstructures. As it is stated earlier, one of the primary challenges limiting the

size and complexity of PVDF structures manufactured via MEAM methods is related to its high coefficient of thermal expansion. Compared to common material extrusion thermoplastics like Acrylonitrile Butadiene Styrene(ABS) and poly lactic acid (PLA), which have CTE values in the range of 70-120 x 10^{-6}/°C [210, 211], homopolymer PVDF demonstrates a CTE in the range of 124-180 x 10^{-6}/°C, depending on its molecular density [1]. Substantial PVDF component warping could occur if this elevated CTE is not compensated for during deposition. In addition, structure dimension shrinkage for PVDF is greater than that for other thermoplastic feedstocks due to this high CTE, making the molecular entanglement between deposited tracks layers extremely important for maintaining component integrity.

To improve the thermal properties or other performance behavior of MEAM printed parts, particulate material can be added to the thermoplastic polymer feedstock material to create composite filaments [115-118]. The focus of this work was exploring the use of zirconium tungstate particulate, a material demonstrating a negative CTE, to mitigate the typical large, positive CTE of homopolymer PVDF while also minimizing degradation of the mechanical integrity of MEAM fabricated components. While other filler material, such as glass fiber [212, 213] and graphite powder [214] have been used to lower the CTE value of PVDF, zirconium tungstate can help maintain PVDF's excellent resistance to corrosive acids compared to some of these other options. In addition, a secondary goal was to maximize the piezoelectric potential of printed by generating PVDF microstructures dominated by β-phase content. In theory, the CTE of the printed composite structures would reduce the net shrinkage and warping found in pure PVDF fabricated parts. In addition, the internal stress state resulting from the inclusion of the

negative CTE zirconium tungstate should also generate a net residual tensile stress in the PVDF matrix upon cooling from the deposition temperature, increasing the likelihood of β-phase microstructure formation.

6.2. Experimental methodology

6.2.1. Materials processing

Negative coefficient of thermal expansion behavior is demonstrated by relatively few materials, with zirconium tungstate [$Zr(WO_4)_2$], scandium tungstate [$Sc_2(WO_4)_3$], cadmium cyanide [$Cd(CN)_2$] and rhenium trioxide [ReO_3] representing such known material systems. Cubic zirconium tungstate exhibits a strong negative CTE response over a range of temperatures consistent with standard MEAM fabrication operating parameters. As it can be synthesized in nano-to-micro sized particulate in the form of rods or whiskers, $Zr(WO_4)_2$ has found use in a variety of composite applications [215, 216].

In this work, both homopolymer PVDF and blended compositions of PVDF/$Zr(WO_4)_2$ were used as a feedstock material for MEAM fabrication of 3D specimens. Homopolymer PVDF (Kynar 740) in pellet form was obtained commercially and used for all filament variations. Composite PVDF/$Zr(WO_4)_2$ filament was manufactured by first mixing ~5 micron mean length zirconium tungstate particulate (American Elements(Figure 43)) with homopolymer PVDF resin pellets at the desired volume fraction using a torque rheometer. The torque rheometer machine (Intelli-Torque Plasti-Corder) was operated at a rotational speed of 15rpm and a temperature of 200°C for approximately two hours to fully disperse the particulate in the PVDF.

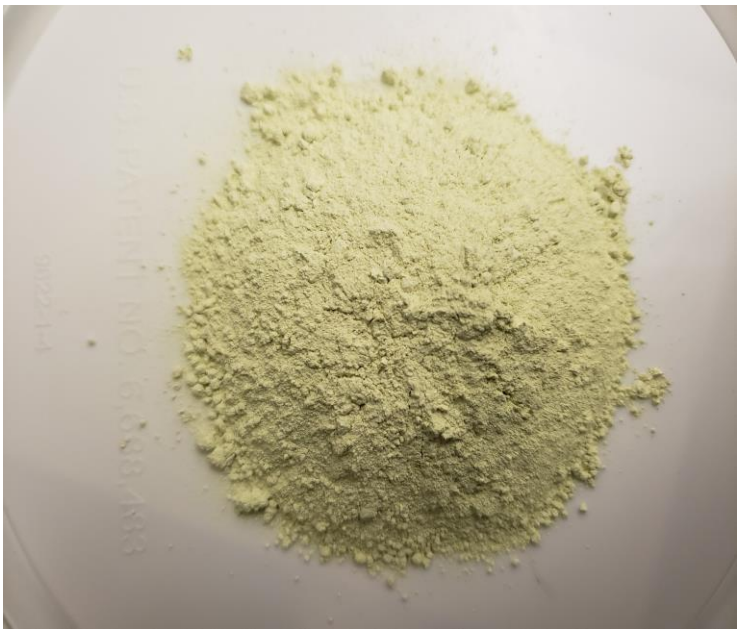

Figure 43. 99.5% (metal basis) Zirconium tungstate powder

Three batches of PVDF/Zirconium tungstate composite with volume fractions of 1%, 2.5% and 10% of $Zr(WO_4)_2$ were processed. The blended composite output was then run through a chopper which turns them into irregular pellet form sized approximately 10 mm in length, suitable for filament extrusion. Figure 44 shows PVDF/ zirconium tungstate pellets which have been created by torque rheometer machine.

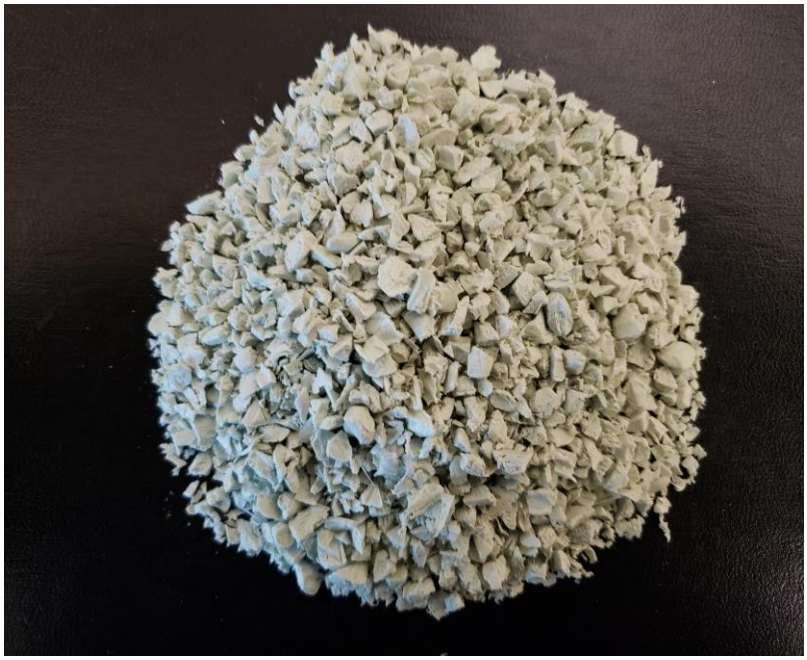

Figure 44. PVDF composite pellets

Pellets of the three composite blends, as well as raw homopolymer PVDF, were then extruded to create moderately cylindrical (1.75±0.15 mm diameter) filament for MEAM deposition.

6.2.2. MEAM deposition parameters

All four types of filaments were extruded on the heated build platform of an open source Reprap Prusa i3 material extrusion 3D printer. Micro-tensile dog bone specimens sized according to ASTM D1708 were fabricated and used for all testing. A schematic of the testing samples dimensions is shown in Figure 45. For each material variation, ten specimens with a thickness of 1.5 mm in the build direction were printed for mechanical and material characterization test. The platform and nozzle temperature were fixed at 110°C and 220°C, respectively. To improve the bonding quality between the first layer and build platform, the heated bed was covered by 3M Scotch blue painter's tape. The deposition parameters used were based on a previous study to optimize structural

integrity of MEAM homopolymer PVDF. Accordingly, the layer height was set to 0.15 mm, and a sharp brass nozzle with 0.35 mm diameter to form the specimens with a 70% infill density. In order to avoid the gaps between perimeters and infill area for each specimen, two shell perimeters were printed at a rate of 10 mm/s, while the infill speed was set to 15 mm/s. Figure 46 shows some of the resulting MEAM printed pure PVDF and PVDF composite samples.

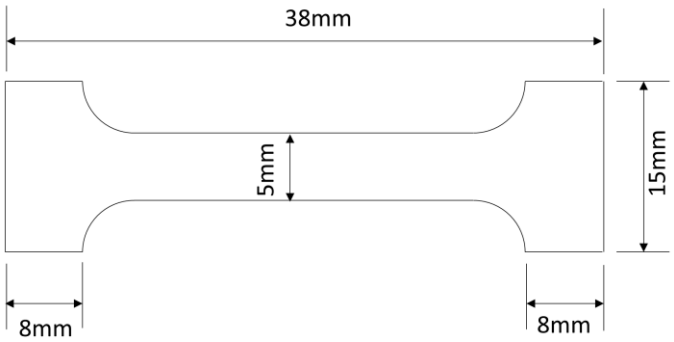

Figure 45. Schematic of testing samples.

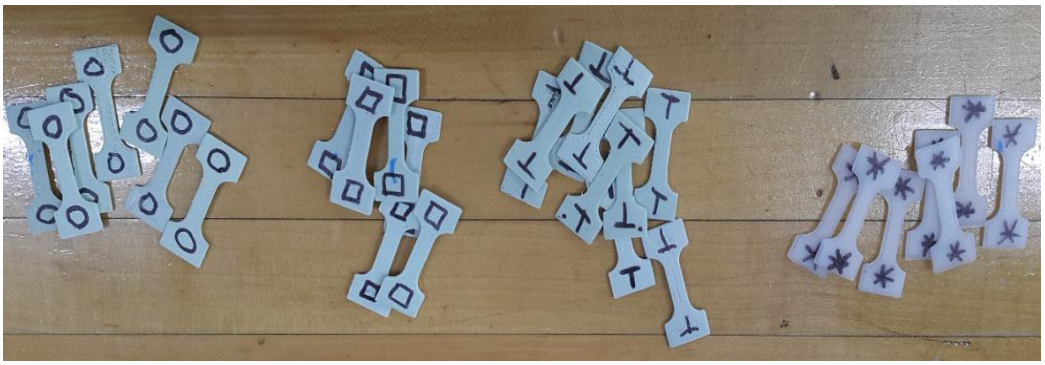

Figure 46. Fabricated samples via MEAM process, from left to right composite 10% fill (○), composite 2.5% fill (□), composite 1% fill (T), and homopolymer PVDF (*).

6.2.3. Microstructure characterization

Microstructure characterization was performed using FTIR with ATR attachment. This technique facilitates investigation of semi-crystalline phase development within the polymer specimens. The ATR mode assists in obtaining the IR spectra in thick samples through the use of surface reflection data. In this test, the intensity of infrared light absorption at different wavelength generates a unique spectral fingerprint associated with the crystalline structure of a material. For this study, a PerkinElmer Spectrum™ 100 FT-IR spectrometer was used to determine the IR spectra of printed specimens in the wavelength range of 400-1300 cm^{-1} with a resolution of 4 cm^{-1} were recorded. From these scans, the relative content of crystalline β-phase for each specimen variation could be measured.

6.2.4. Measurements of coefficient of thermal expansion

Coefficient of thermal expansion is a physical characteristic that represents the dimensional changes, often fairly linear, that a material undergoes during a temperature change. According to Equation 3, the coefficient of linear thermal expansion (α) of a pure material can be calculated using :

$$\alpha = (\Delta L/L)\ (1/\Delta T) \tag{4}$$

where ΔT is the temperature differential and ΔL/L is thermal strain. The theoretical value of CTE for a bulk composite material can be predicted utilizing the Turner equation, shown in Equation 4 [217]:

$$\alpha_{Comp} = \left(\frac{\alpha_{matrix}\, \kappa_{matrix}\, V_{matrix} + \alpha_{\text{particulate}}\, \kappa_{\text{particulate}}\, V_{\text{particulate}}}{\kappa_{matrix}\ V_{matrix} + \kappa_{\text{particulate}}\, V_{\text{particulate}}} \right) \tag{5}$$

where α refers to the CTE and κ is the bulk modulus for either the matrix, or particulate depending on subscript, and the terms V_{matrix} and $V_{particulate}$ represent the matrix and reinforcement volume fraction within the composite part, respectively. Particulate loading fraction and void volume (*i.e.*, porosity) are two main factors that influence the total CTE value of a composite. The direct impact of void volume is much less than fiber volume and can be quantified by comparing the CTE of MEAM pure PVDF structures with dense, bulk material. Void existence can lead to indirect effects on the total amount of the CTE of the composite, in that the matrix may show microcrack formation and may influence the moisture content of the composite [218].

Various methods for measuring thermally driven displacement changes have been previously deployed and can be divided into mechanical dilatometry, optical methods, and diffraction-based techniques [219]. In this chapter, the optical-based method Digital Image Correlation (DIC) system was used to monitor strain development on the surface of the 1.5 mm thick specimens. A two camera, 3D DIC system with commercial software VIC-3D (Correlated Solutions) was used to map 3D displacements and strain fields of the speckled surface, while specimens were heated on the thermal plate (Dataplate hot plate/Stirrer Series 720) from room temperature up to 180°C at a rate of approximately 10°C per minute. A thermocouple probe (Fluke 179 true RMS multimeter) monitored the surface temperature of the printed specimens, which were otherwise free to expand. Prior to testing, specimens were coated with a thin layer of paint to provide a speckle pattern appropriate for performing DIC analysis.

6.2.5. Micro-tensile specimen testing

Fabricated samples were subjected to tensile loaded in an universal materials testing machine at a constant displacement rate of 1.25 mm/min (Figure 47). Following ASTM standards for tensile testing [220, 221], a minimum of five tensile specimens from each group of samples were used for mechanical testing. Displacement and force were recorded automatically by the tensile testing apparatus, and in-plane strains were measured in the specimen gage regions using the same 3D DIC system used for CTE characterization. All taken images were analyzed using DIC software in order to obtain both axial and transverse strains (Figure 48). Painted and unpainted sides of one of the broken samples after tensile testing test is shown in Figure 49.

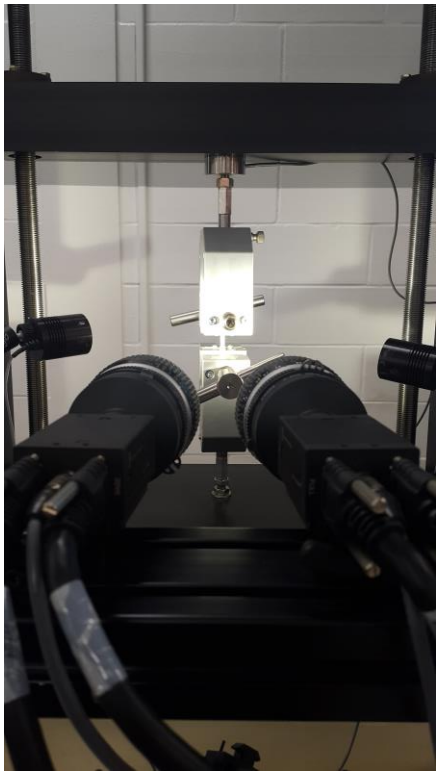

Figure 47. Tensile test apparatus and DIC system

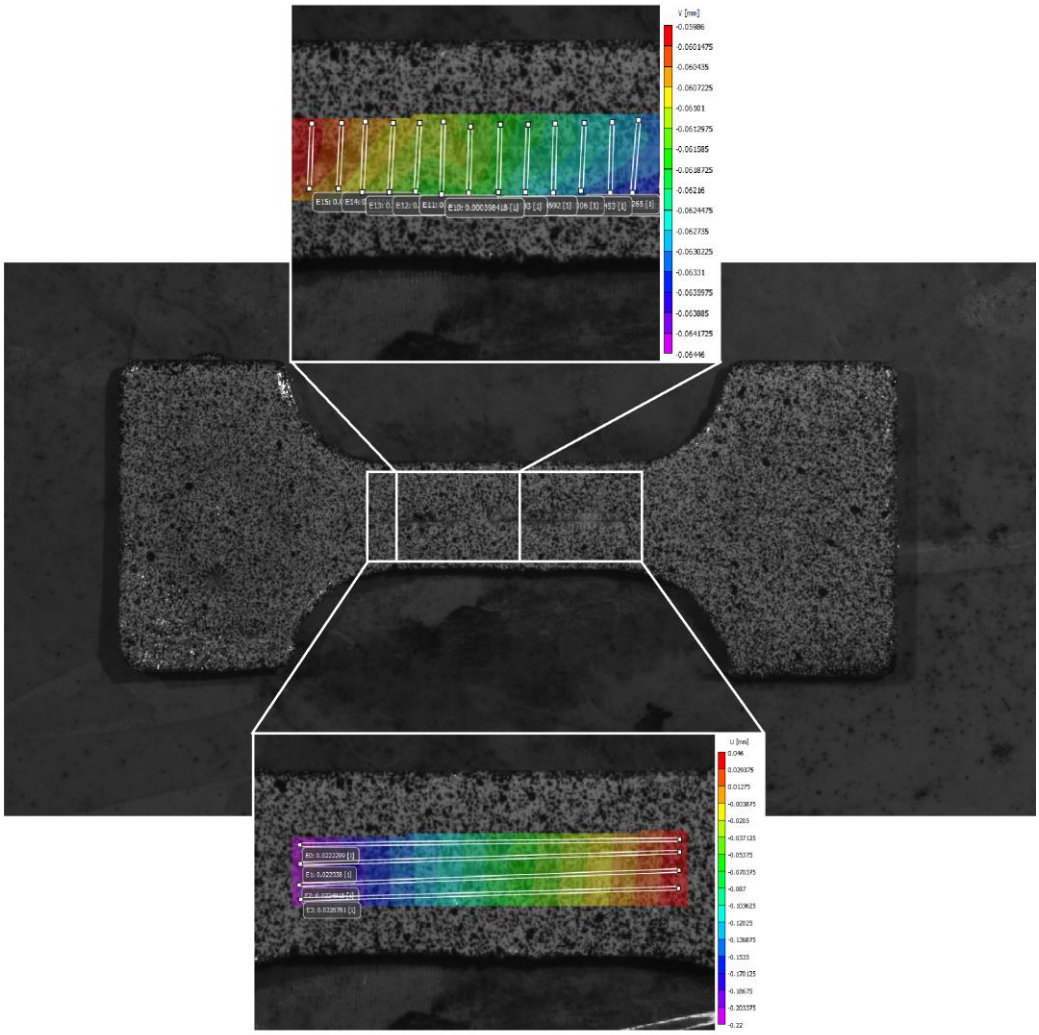

Figure 48. Speckle pattern on specimen, with insets showing displacements in the transverse (top) and axial (bottom) directions, as well as the virtual extensometers used to measure associated strains.

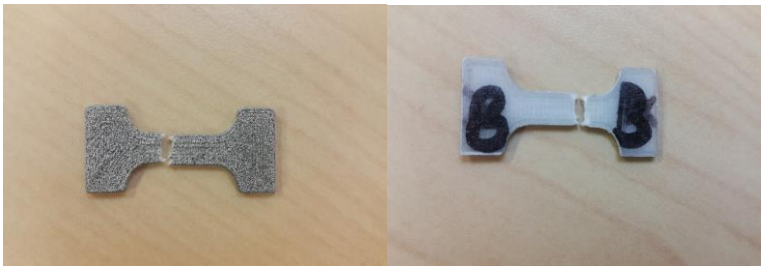

Figure 49. Typical PVDF sample after mechanical testing (2 sides)

6.3. Results of zirconium tungstate additives

6.3.1. FTIR Results

According to literature [7, 217] the peak at 1070 cm^{-1} in the PVDF FTIR spectra is the only vibrational band that is independent from all crystalline forms. Therefore, all of the FTIR result should be normalized according to this peak, a procedure that was performed in this study. The fraction of β-phase in each specimen was calculated by using Equation 1. This equation was used in order to quantify the semi-crystalline microstructure resulting from MEAM fabrication. The amount of calculated β-phase fraction found for each material variation is listed in Table 10.

Table 10. β-phase fraction of the MEAM fabricated specimens

Samples	F (β)
Pure PVDF (0%)	0.478
PVDF composite (1%)	0.471
PVDF composite (2.5%)	0.466
PVDF composite (10%)	0.460

The relative content of β-phase was found to be highest in the pure PVDF samples. While the fraction of crystalline β-phase trended downward as the loading of zirconium tungstate increased, the changes with particulate loading were small. In fact, only a 1.8% total difference in β-phase content was found between the pure homopolymer PVDF and the maximum $Zr(WO_4)_2$ loading case (composite 10%). According to the Table 10, adding zirconium tungstate to the PVDF matrix did not have significant reduction in the β-phase fraction of the printed components, any of these cases were suitable regarding the β-phase fraction. The FTIR spectra for all samples are shown

in Figure 50. As presented, the absorbance at 840 cm^{-1} for homopolymer PVDF was a bit higher than PVDF composites.

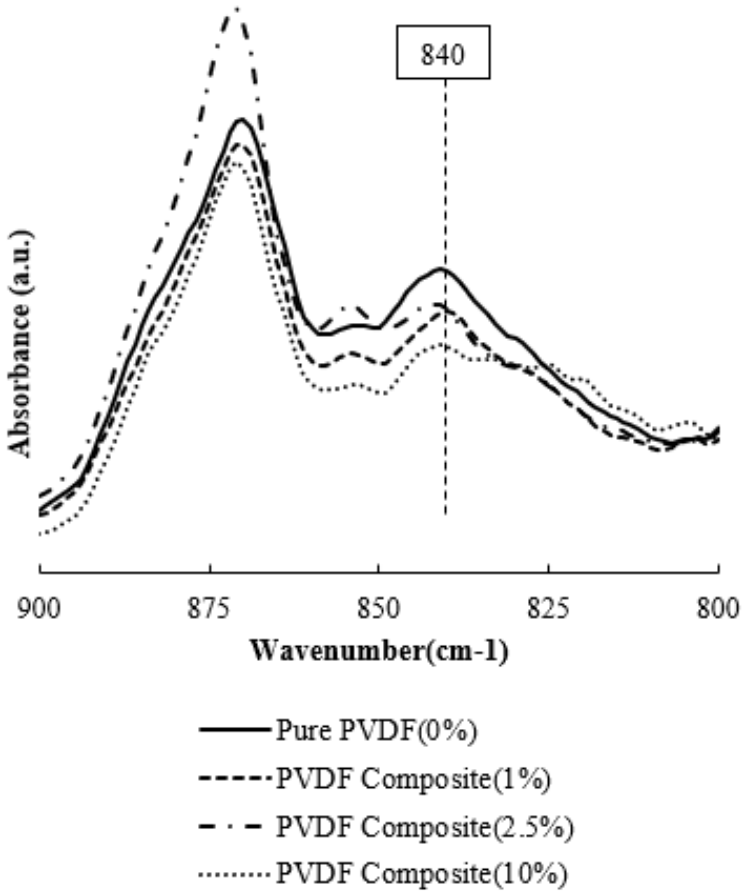

Figure 50. FTIR spectra of printed samples (PVDF homopolymer and PVDF composites)

6.3.2. Coefficient of thermal expansion results

As shown in Figure 51a, the average maximum thermal strain found for the PVDF homopolymer was 33,730 με and for PVDF composite with 10% $Zr(WO_4)_2$ was only 20,1840 με, a drop of ~40% in net expansion. The corresponding CTE values determined for the entire range of temperatures tested showed consistent behavior, Figure 51b. Adding just 1% by volume of the $Zr(WO_4)_2$ micro particulate decreased the net CTE by

~17%. PVDF with 70% infill density was different from the theoretical CTE value supplied by the manufacturer. Because of the resistance from zirconium tungstate to expand upon heating due to its intrinsic properties, pure PVDF had higher thermal strain than PVDF composite and this resistance raised up by doping more particulate in the matrix. Reduction in CTE by adding more zirconium tungstate particulate can be proved theoretically as well. According to the equation 3, by having more $Zr(WO_4)_2$ particulate within PVDF matrix, the numerator of the mentioned fraction is decreased, while denominator is increased. Therefore, it was led to lower amount of CTE.

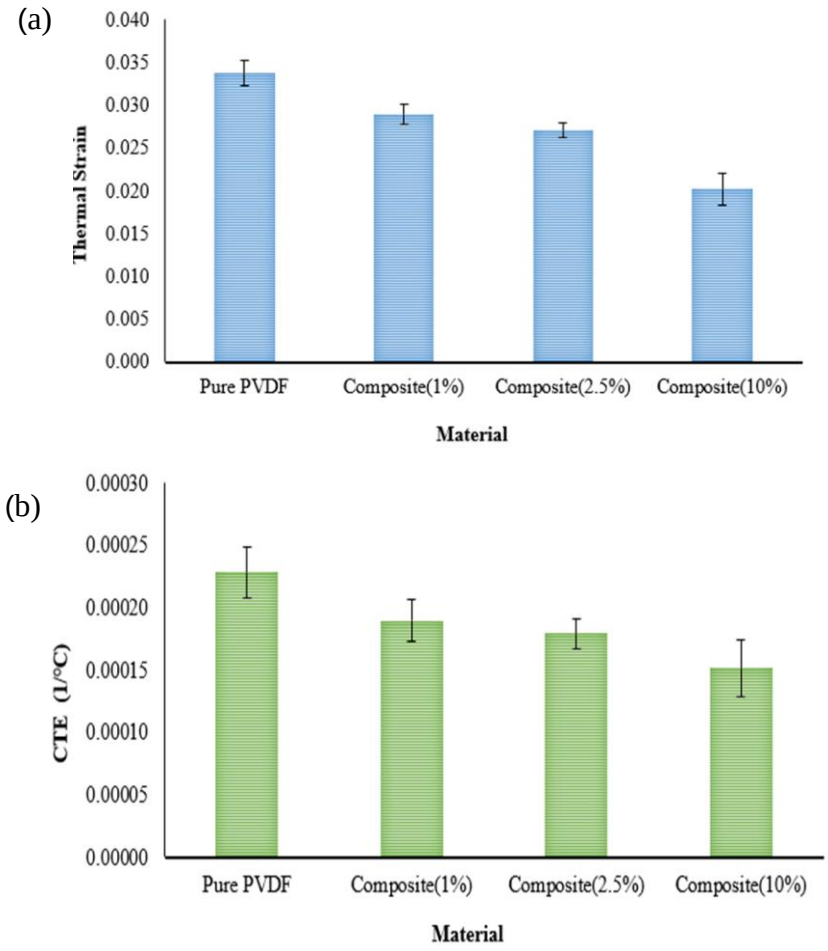

Figure 51. Maximum thermal strain (at 180°C) measured via DIC (a), and the averaged CTE response found over the entire 25-180°C temperature range for each specimen variation (b).

The experimentally determined CTEs, along with theoretically predicted values, are presented in Table 11. As expected, the experimental CTE value for MEAM printed homopolymer PVDF with 70% infill density was different from the theoretical CTE value supplied by the manufacturer. Practically, the significance of such CTE reductions for MEAM printing of PVDF means that larger components can be fabricated without experiencing separation from the build platform due to warping. In addition,

manufactured structures will more accurately represent the digital model features they are based upon (*i.e.*, better dimensional tolerances).

Table 11. Comparison between experimentally measured and theoretical values of CTE found via equation (2).

Samples	Theoretical value	Experimental value	Standard deviation	Percentage decrease from pure PVDF
Homopolymer PVDF	---	2.29E-04	±6.22E-06	---
PVDF composite (1%)	2.22E-04	1.90E-04	±4.67E-06	-17%
PVDF composite (2.5%)	2.13E-04	1.79E-04	±1.38E-06	-22%
PVDF composite (10%)	1.73E-04	1.52E-04	±1.41E-05	-34%

6.3.3. Tensile testing results

Representative stress-strain responses of micro tensile specimens are shown in Figure 52, and a summary of the average effective yield stress and stiffness response for each is included in Table 12. Clearly, the addition of zirconium tungstate degraded the mechanical strength of the MEAM PVDF components. The Young's modulus improved for about 30% in PVDF composite (10%) than pure PVDF. Moreover, according to the area under load-displacement curve of printed samples, the energy absorption of PVDF composite (1%) was about 32% and 60% higher than composite with 2.5% and 10% volume of zirconium tungstate, respectively. The likely explanation for the reductions in mechanical strength associate with higher particulate doping levels is the quality of interfacial adhesion strength between the PVDF and the embedded material. Debonding between the disparate composite constituents would explain the strength degradation observed.

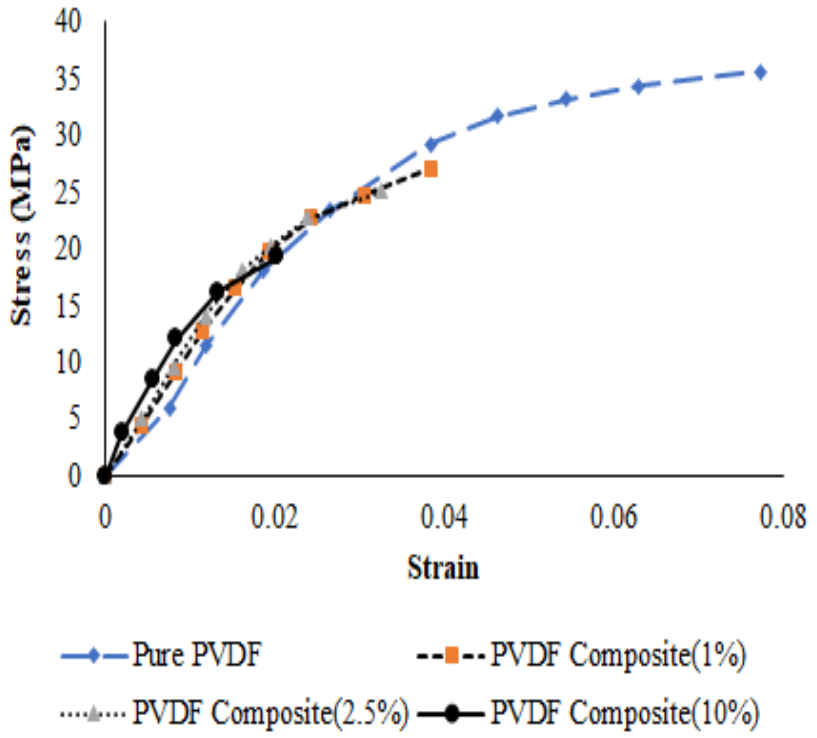

Figure 52. The stress-strain curve from MTI testing machine

Table 12. Average yield stress (MPa) and Young's modulus of micro tensile specimens

Samples	Avg. yield strength (MPa)	Standard deviation (MPa)	Young's modulus (MPa)
Homopolymer PVDF	35.5	±1.7	845.6
PVDF composite (1%)	25.9	±1.1	1081.7
PVDF composite (2.5%)	24.3	±0.6	1111.1
PVDF composite (10%)	19.0	±1.6	1194.3

6.4. Significance of zirconium tungstate additives

There are multiple takeaways from this study, which elucidates some of the relationships between mechanical strength, CTE, and microstructure development for PVDF/$Zr(WO_4)_2$ composite particulate loading. Clear trends emerged from this work, the most substantial being the relation between increases in zirconium tungstate particulate content and reduction in mechanical strength. However, the addition of $Zr(WO_4)_2$ particulate was also found to greatly reduce the net component CTE, while also having a small effect on the measured β-phase fraction.

Ideally, the proper level of particulate loading could be added such that the desired combination of mechanical strength and component warping for a particulate MEAM structure application could be constructed. Some circumstances may require more mechanical strength, while others may demand higher dimensional tolerances. Conversely, applications using material systems with greater $Zr(WO_4)_2$ content could compensate for the mechanical strength reductions through the use of larger structures, while still reaping the benefits of lesser component warping.

6.5. Conclusions

The addition of $Zr(WO_4)_2$ particulate within a PDVF matrix was found to vastly reduce the net CTE in MEAM fabricated components, with the amount of CTE reduction scaling directly with the particulate content loading. This result is significant in that, with sufficient particulate loading, the net CTE of the $Zr(WO_4)_2$/PVDF composite filament can be lowered into the same range as standard filament-based MEAM deposition materials. Such CTE mitigation is useful for minimizing structure warping and improving manufactured part dimensional tolerances. However, the $Zr(WO_4)_2$ particulate loading

also caused a substantial reduction in mechanical strength properties, lowering both the effective yield stress and elongation to failure. Furthermore, a slight reduction in the formation of β-phase microstructure in PVDF, which is associated with a significant piezoelectric response, occurred with $Zr(WO_4)_2$ particulate loading. These results suggest the concentration of particulate loading could be tailored to balance dimensional tolerances and mechanical properties appropriate for a particular application.

CHAPTER 7

CONCLUSIONS AND FUTURE WORK

In this research, the feasibility of utilizing PVDF homopolymer as a smart polymer for creating various 3D printed objects with different geomtries and a balanced mix of mechanical and electro-mechanical behaviors to supplant several frameworks with one single smart segment was illustrated. Due to the molecular weight and microstructure resulting from processing, PVDF has a large coefficient of thermal expansion. In addition, volume of shrinkage in semi-crystalline polymers are much greater than amorphous material which leads to dimensional instability in semi-crystalline materials. Therefore, due to the aforementioned impediments, utilizing PVDF as feedstock material for fabricating objects with sensing or actuation capabilities through the MEAM approach presents numerous difficulties. This work quantified many of these issues and presented approaches for mitigating their sources.

An initial parametric study was performed that identified a viable process deposition range for MEAM PVDF parts based on the integrity, physical dimensions, appearance, and performance. Utilizing the quasi-optimized printing parameters found, including a heated print bed (at 100°C), slower printing speeds (15 mm/s), thicker first deposition layer than other deposition layers, and inclusion of a specimen brim, this work reported the first successful MEAM production of truly three-dimensional PVDF

components (work published in Rapid Prototyping journal [112]). Studying the effects of MEAM printing with these parameters on PVDF microstructure also showed that the β-phase fraction in PVDF fabricated parts was about three times larger than in its pellet form. Due to stretching during printing and annealing at high pressure in the nozzle of MEAM 3D printer, semi-crystalline phase of 3D printed samples were about 31 percent and 18 percent higher than extruded filament and extrudate, respectively.

Apart from the effect of printing conditions on physical properties of fabricated part, the influence of some of the deposition parameters on electromechanical coupling behavior was investigated. Due to the lower air gaps and porosity in samples with higher infill density, more solid specimen had higher semi-crystalline phase fraction. For instance, samples with 75% infill density had about 22% lower electromechanical attributes than 100% counterparts. β-phase fraction for different infill patterns were about the same which means the infill types did not have remarkable impact on electrical features of final printed parts. Due to stressing/stretching during printing, both smaller nozzle diameter and thinner layer thickness were significant factors on improving the crystalline β-phase fraction within the fabricated structures. Piezoelectric polymorph within samples with 1 mm layer height were about 32% higher than parts with 2 mm layer thickness. Electroactive β-phase content in samples which are printed with 0.4 mm diameter nozzles was greater by about 15% than created samples with 1 mm diameter brass nozzles.

In order to get better understanding of degree of component warping and locked-in thermal stress in the MEAM objects, warpage and residual stress were measured using simulation and experimental method. According to acquired DIC images and Digimat-

AM simulation data, warpage did not have a monotonic relationship with the height of fabrication samples. It had a peak point at 20mm in warpage versus height plot and this warping rate is decreased with increasing in the height of samples. The range of warpage was around 0.45-0.84 mm for samples with same cross section area and different heights (from 2.5 mm to 80 mm). The maximum residual stress was in the range of 7-28 MPa for samples with (5 mm to 40 mm) height. This difference was attributed to taller parts experiencing a greater number heating/cooling cycles and larger thermal gradients between the hot-end and the component locations in contact with the print bed. In all cases, tensile residual stresses were found near the top surface, transitioning into compressive stress states towards the bottom of the specimens.

Although using suggested deposition parameters helped to improve the physical integrity and dimensional accuracy of MEAM parts, experimental and simulation results showed that warping still occurs in fabricated PVDF parts. The main reason of the unwanted distortion is related to PVDF's high CTE value. In order to increase the total CTE of the printed parts, zirconium tungstate as material with negative CTE values was added to PVDF matrix and thermal strain, CTE, mechanical and electro-mechanical behavior of PVDF composite samples were evaluated. Compared with pure homopolymer printed specimens, results show that the particulate additives effectively lowered the net coefficient of thermal expansion and thermal strain at the expense of yield strength and total elongation to failure, while the semi-crystalline structure showed a mild reduction in β-phase formation associated with increasing particulate content. Average yield stress for pure PVDF samples was about 2 times greater than PVDF

composite with 10% $Zr(WO_4)_2$, but CTE was about 31% lower in 10% PVDF composite samples.

Post-processing heat treatments were found to improve the mechanical and electromechanical properties of PVDF 3D printed samples. Due to changes in molecular mobility during the annealing process, porosity and internal defects were reduced, which in turn caused improvements in the UTS, Young modulus and β-phase fraction of heat-treated samples. In addition, due to recrystallization in heat treatment process, crystallinity is increased. Improvement in crystallization led to increase on mechanical and piezoelectric performance of 3D printed PVDF samples. Therefore, mechanical responses of annealed parts were greater than as-printed counterparts. Because of phase transformation of PVDF, samples which were heated around 85°C had the highest absorption peak and results showed that longer heat treating will increase the electromechanical properties of PVDF samples. Moreover, results showed that electrical poling as another post-processing method, aligned the di-poles within the PVDF structure and helped to enhance net piezoelectric properties of fabricated parts. The output voltage of a poled PVDF sample a was about 300% higher than that sample when it was not poled.

One natural extension of this work is to consider adding a secondary constituent particulate phase to the PVDF matrix to further enhance piezoelectricity, such as barium titanate ($BaTiO_3$). Barium titanate has been heavily studied as an electro-ceramic material, and could help maintain the biocompatibility aspects of the composite. Other electro-ceramic particulate may be considered, such as PZT, though the lead content of PZT will sacrifice biocompatibility of the resulting composite. Another extension of this

work could be employing a dual head extrusion in a filament extrusion printing system, one could easily print 95% of a component out of homopolymer PVDF (very cheap) and limit the expensive specialty polymer deposition to areas where piezoelectricity is desired. Therefore, the printed part would have desirable mechanical and elerctro-mechanical coupling responses. A variety of potential applications could possibly gain from improving the piezoelectric properties of PVDF component.

REFERENCES

1. Economidou, S.N. and D. Karalekas, *Optical sensor-based measurements of thermal expansion coefficient in additive manufacturing.* Polymer Testing, 2016. **51**: p. 117-121.
2. Wang, Y. and M. Cakmak, *Hierarchical structure gradients developed in injection-molded PVDF and PVDF–PMMA blends. I. Optical and thermal analysis.* Journal of applied polymer science, 1998. **68**(6): p. 909-926.
3. Zhong, G.J. and Z.M. Li, *Injection molding-induced morphology of thermoplastic polymer blends.* Polymer Engineering & Science, 2005. **45**(12): p. 1655-1665.
4. Sood, A.K., R.K. Ohdar, and S.S. Mahapatra, *Parametric appraisal of mechanical property of fused deposition modelling processed parts.* Materials & Design, 2010. **31**(1): p. 287-295.
5. Lee, C. and J.A. Tarbutton, *Electric poling-assisted additive manufacturing process for PVDF polymer-based piezoelectric device applications.* Smart Materials and Structures, 2014. **23**(9): p. 095044.
6. Tarbuttona, J., et al., *Phase transformation and shock sensor response of additively manufactured piezoelectric PVDF*. Procedia Manufacturing, 2017. **10**: p. 982-989.
7. Porter, D.A., T.V. Hoang, and T.A. Berfield, *Effects of in-situ poling and process parameters on fused filament fabrication printed PVDF sheet mechanical and electrical properties.* Additive Manufacturing, 2017. **13**: p. 81-92.
8. Kim, H., et al., *Fabrication and characterization of 3D printed BaTiO3/PVDF nanocomposites.* Journal of Composite Materials, 2018. **52**(2): p. 197-206.
9. McEvoy, M.A. and N. Correll, *Materials that couple sensing, actuation, computation, and communication.* Science, 2015. **347**(6228): p. 1261689.
10. Lagomarsini, C., et al., *Hybrid piezoelectric–electrostatic generators for wearable energy harvesting applications.* Smart Materials and Structures, 2019. **28**(3): p. 035003.
11. Giurgiutiu, V.J.J.o.i.m.s. and structures, *Review of smart-materials actuation solutions for aeroelastic and vibration control.* 2000. **11**(7): p. 525-544.
12. Oliveira, J., et al., *Polymer-based smart materials by printing technologies: Improving application and integration.* Additive Manufacturing, 2018.
13. Dineva, P., et al., *Piezoelectric Materials*, in *Dynamic Fracture of Piezoelectric Materials*. 2014, Springer. p. 7-32.
14. Momenzadeh, N., C.M. Stewart, and T. Berfield, *Mechanical and Thermal Characterization of Fused Filament Fabrication Polyvinylidene Fluoride (PVDF) Printed Composites*, in *Mechanics of Additive and Advanced Manufacturing, Volume 8*. 2019, Springer. p. 59-65.
15. Acosta, M., et al., *BaTiO3-based piezoelectrics: Fundamentals, current status, and perspectives.* Applied Physics Reviews, 2017. **4**(4): p. 041305.

16. Wu, J., D. Xiao, and J. Zhu, *Potassium–sodium niobate lead-free piezoelectric materials: past, present, and future of phase boundaries.* Chemical reviews, 2015. **115**(7): p. 2559-2595.
17. Zheng, T., et al., *Recent development in lead-free perovskite piezoelectric bulk materials.* Progress in materials science, 2018. **98**: p. 552-624.
18. Bar-Cohen, Y. and Q. Zhang, *Electroactive Polymer Actuators and Sensors.* MRS Bulletin, 2008. **33**(3): p. 173-181.
19. Khaled, S.R., D. Sameoto, and S. Evoy, *A review of piezoelectric polymers as functional materials for electromechanical transducers.* Smart Materials and Structures, 2014. **23**(3): p. 033001.
20. Murayama, N. and H. Obara, *Piezoelectric polymers and their applications.* Japanese Journal of Applied Physics, 1983. **22**(S3): p. 3.
21. Chen-Glasser, M., et al., *Piezoelectric materials for medical applications.* Piezoelectricity-Organic and Inorganic Materials and Applications, 2018: p. 125-145.
22. Derakhshani, M., T. Berfield, and K.D. Murphy. *Dynamic Analysis of a Bi-stable Buckled Structure for Vibration Energy Harvester*. 2018. Cham: Springer International Publishing.
23. Fukada, E., *History and recent progress in piezoelectric polymers*. IEEE Transactions on ultrasonics, ferroelectrics, and frequency control, 2000. **47**(6): p. 1277-1290.
24. Bar-Cohen, Y. *Electroactive polymers as artificial muscles: capabilities, potentials and challenges*. in *Robotics 2000*. 2000.
25. Ramadan, K.S., D. Sameoto, and S. Evoy, *A review of piezoelectric polymers as functional materials for electromechanical transducers.* Smart Materials and Structures, 2014. **23**(3): p. 033001.
26. Mohebbi, A., et al., *Cellular polymer ferroelectret: a review on their development and their piezoelectric properties.* Advances in Polymer Technology, 2018. **37**(2): p. 468-483.
27. Harrison, J. and Z. Ounaies, *Piezoelectric polymers*. Wiley Online Library.
28. Cohen, J. and S. Edelman, *Piezoelectric Effect in Oriented Polyvinylchloride and Polyvinylflouride.* Journal of Applied Physics, 1971. **42**(8): p. 3072-3074.
29. Mathur, S., J. Scheinbeim, and B. Newman, *Piezoelectric properties and ferroelectric hysteresis effects in uniaxially stretched nylon-11 films.* Journal of applied physics, 1984. **56**(9): p. 2419-2425.
30. Kawai, H., *The piezoelectricity of poly (vinylidene fluoride).* Japanese Journal of Applied Physics, 1969. **8**(7): p. 975.
31. Wiederkehr, R.S., et al. *Development of microvalves for gas flow control in micronozzles using PVDF piezoelectric polymer*. in *Journal of Physics: Conference Series*. 2008. IOP Publishing.
32. Bian, Y., et al., *Design and fabrication of a metal core PVDF fiber for an air flow sensor.* Smart Materials and Structures, 2015. **24**(10): p. 105001.
33. Tamura, M., et al., *Electroacoustic transducers with piezoelectric high polymer films.* Journal of the Audio Engineering Society, 1975. **23**(1): p. 21-26.
34. Wang, G., et al., *Flexible pressure sensor based on PVDF nanofiber.* Sensors and Actuators A: Physical, 2018. **280**: p. 319-325.

35. Cochran, S., *Piezoelectricity and basic configurations for piezoelectric ultrasonic transducers*, in *Ultrasonic transducers*. 2012, Elsevier. p. 3-35.
36. Sencadas, V., R. Gregorio Jr, and S. Lanceros-Méndez, *α to β phase transformation and microestructural changes of PVDF films induced by uniaxial stretch.* Journal of Macromolecular Science®, 2009. **48**(3): p. 514-525.
37. Ueberschlag, P., *PVDF piezoelectric polymer.* Sensor Review, 2001. **21**(2): p. 118-126.
38. Sirohi, J. and I. Chopra, *Fundamental Understanding of Piezoelectric Strain Sensors.* Journal of Intelligent Material Systems and Structures, 2000. **11**(4): p. 246-257.
39. Brooke, M., *Using polyvinylidene fluoride (PVDF) to handle chromium plating solutions.* Plating and surface finishing, 1987. **74**(7): p. 42-46.
40. Stirling, C., V. Van Tilburg, and N. Miller, *Cracking of poly (vinylidene fluoride) due to chemical attack.* Polymers & polymer composites, 1993. **1**(3): p. 167-174.
41. Laroche, G., et al., *Polyvinylidene fluoride (PVDF) as a biomaterial: from polymeric raw material to monofilament vascular suture.* Journal of Biomedical Materials Research Part A, 1995. **29**(12): p. 1525-1536.
42. Häsler, E., L. Stein, and G. Harbauer, *Implantable physiological power supply with PVDF film.* Ferroelectrics, 1984. **60**(1): p. 277-282.
43. Mishra, S., et al., *Advances in piezoelectric polymer composites for energy harvesting applications: A systematic review.* Macromolecular Materials and Engineering, 2019. **304**(1): p. 1800463.
44. Kang, G.-d. and Y.-m. Cao, *Application and modification of poly(vinylidene fluoride) (PVDF) membranes – A review.* Journal of Membrane Science, 2014. **463**: p. 145-165.
45. Inderherbergh, J., *Polyvinylidene fluoride (PVDF) appearance, general properties and processing.* Ferroelectrics, 1991. **115**(4): p. 295-302.
46. Wang, H., et al., *A robust superhydrophobic PVDF composite coating with wear/corrosion-resistance properties.* Applied Surface Science, 2015. **332**: p. 518-524.
47. Rathod, V., et al., *Characterization of a large-area PVDF thin film for electro-mechanical and ultrasonic sensing applications.* Sensors and Actuators A: Physical, 2010. **163**(1): p. 164-171.
48. Wang, F., M. Tanaka, and S. Chonan, *Development of a PVDF piezopolymer sensor for unconstrained in-sleep cardiorespiratory monitoring.* Journal of intelligent material systems and structures, 2003. **14**(3): p. 185-190.
49. Jeon, J.-H., et al., *Novel biomimetic actuator based on SPEEK and PVDF*. Sensors and actuators B: Chemical, 2009. **143**(1): p. 357-364.
50. Lopes, A., J. Gutiérrez, and J. Barandiarán, *Direct fabrication of a 3D-shape film of polyvinylidene fluoride (PVDF) in the piezoelectric β-phase for sensor and actuator applications.* European Polymer Journal, 2018. **99**: p. 111-116.
51. Jung, I., et al., *Flexible piezoelectric polymer-based energy harvesting system for roadway applications.* Applied Energy, 2017. **197**: p. 222-229.
52. Jiang, Y., et al., *Low-frequency energy harvesting using a laminated PVDF cantilever with a magnetic mass.* Power MEMS, 2010. **2010**: p. 375378.

53. Martins, P., A. Lopes, and S. Lanceros-Mendez, *Electroactive phases of poly (vinylidene fluoride): determination, processing and applications.* Progress in polymer science, 2014. **39**(4): p. 683-706.
54. Salimi, A. and A. Yousefi, *Analysis method: FTIR studies of β-phase crystal formation in stretched PVDF films.* Polymer Testing, 2003. **22**(6): p. 699-704.
55. Li, Y., C. Liao, and S.C.J.N. Tjong, *Electrospun polyvinylidene fluoride-based fibrous scaffolds with piezoelectric characteristics for bone and neural tissue engineering.* 2019. **9**(7): p. 952.
56. Ruan, L., et al., *Properties and Applications of the β Phase Poly (vinylidene fluoride).* Polymers, 2018. **10**(3): p. 228.
57. Wang, X., et al., *Tactile-sensing based on flexible PVDF nanofibers via electrospinning: A review.* 2018. **18**(2): p. 330.
58. Sencadas, V., et al. *α-to β Transformation on PVDF films obtained by uniaxial stretch*. in *Materials science forum*. 2006. Trans Tech Publ.
59. Hosseini, M. and A.S.H. Makhlouf, *Industrial applications for intelligent polymers and coatings*. 2016: Springer.
60. Sencadas, V., et al., *Relaxation dynamics of poly (vinylidene fluoride) studied by dynamical mechanical measurements and dielectric spectroscopy.* 2012. **35**(5): p. 1-11.
61. Liu, J., X. Lu, and C.J.M. Wu, *Effect of preparation methods on crystallization behavior and tensile strength of poly (vinylidene fluoride) membranes.* 2013. **3**(4): p. 389-405.
62. Stucker, B. *Additive manufacturing technologies: technology introduction and business implications*. in *Frontiers of Engineering: Reports on Leading-Edge Engineering From the 2011 Symposium, National Academies Press, Washington, DC, Sept*. 2012.
63. Standard, A., *F2792-12a. 2012.* Standard terminology for additive manufacturing technologies. **10**.
64. Dey, A. and N. Yodo, *A systematic survey of FDM process parameter optimization and their influence on part characteristics.* Journal of Manufacturing and Materials Processing, 2019. **3**(3): p. 64.
65. Bourell, D.L., *Perspectives on additive manufacturing.* Annual Review of Materials Research, 2016. **46**: p. 1-18.
66. Wohlers, T. and T. Gornet, *History of additive manufacturing.* Wohlers report, 2014. **24**(2014): p. 118.
67. Miyanaji, H., et al., *Process development of porcelain ceramic material with binder jetting process for dental applications.* Jom, 2016. **68**(3): p. 831-841.
68. Wang, X., et al., *Topological design and additive manufacturing of porous metals for bone scaffolds and orthopaedic implants: A review.* Biomaterials, 2016. **83**: p. 127-141.
69. Huotilainen, E., et al., *Imaging requirements for medical applications of additive manufacturing.* 2014. **55**(1): p. 78-85.
70. Galante, R., C.G. Figueiredo-Pina, and A.P.J.D.M. Serro, *Additive manufacturing of ceramics for dental applications: A review.* 2019.
71. Shapiro, A.A., et al., *Additive manufacturing for aerospace flight applications.* Journal of Spacecraft and Rockets, 2016: p. 952-959.

72. Ngo, T.D., et al., *Additive manufacturing (3D printing): A review of materials, methods, applications and challenges.* Composites Part B: Engineering, 2018. **143**: p. 172-196.
73. Froes, F., R. Boyer, and B. Dutta, *Introduction to aerospace materials requirements and the role of additive manufacturing*, in *Additive Manufacturing for the Aerospace Industry*. 2019, Elsevier. p. 1-6.
74. Froes, F.H. and R. Boyer, *Additive Manufacturing for the Aerospace Industry*. 2019: Elsevier.
75. Lipton, J., et al. *Multi-material food printing with complex internal structure suitable for conventional post-processing*. in *Solid freeform fabrication symposium*. 2010.
76. Yang, F., et al., *Investigation on lemon juice gel as food material for 3D printing and optimization of printing parameters.* Lwt, 2018. **87**: p. 67-76.
77. Godoi, F.C., S. Prakash, and B.R.J.J.o.F.E. Bhandari, *3d printing technologies applied for food design: Status and prospects.* 2016. **179**: p. 44-54.
78. Yang, F., et al., *Recent development in 3D food printing.* 2017. **57**(14): p. 3145-3153.
79. Gosselin, C., et al., *Large-scale 3D printing of ultra-high performance concrete–a new processing route for architects and builders.* Materials & Design, 2016. **100**: p. 102-109.
80. De Schutter, G., et al., *Vision of 3D printing with concrete—technical, economic and environmental potentials.* Cement and Concrete Research, 2018. **112**: p. 25-36.
81. Paoletti, I., *Mass customization with additive manufacturing: new perspectives for multi performative building components in architecture.* 2017.
82. Cruz, P.J., et al. *From rapid prototyping to building in real scale: methodologies for upscaling additive manufacturing in architecture*. in *Proceedings of IASS Annual Symposia*. 2019. International Association for Shell and Spatial Structures (IASS).
83. Savastano, M., et al., *3-D printing in the spare parts supply chain: an explorative study in the automotive industry*, in *Digitally supported innovation*. 2016, Springer. p. 153-170.
84. Chinthavali, M. *3D printing technology for automotive applications*. in *2016 International Symposium on 3D Power Electronics Integration and Manufacturing (3D-PEIM)*. 2016. IEEE.
85. Liang, C., et al. *Evaluation of Tire Traction Performance on Dry Surface Based on Tire-Road Contact Stress*. in *SIAR International Congress of Automotive and Transport Engineering: Science and Management of Automotive and Transportation Engineering*. 2019. Springer.
86. Mousavi, H., M.N. Shenvi, and C. Sandu. *Experimental Study for Free Rolling of Tires on Ice*. in *International Design Engineering Technical Conferences and Computers and Information in Engineering Conference*. 2019. American Society of Mechanical Engineers.
87. Yap, Y. and W. Yeong, *Additive manufacture of fashion and jewellery products: a mini review: This paper provides an insight into the future of 3D printing*

industries for fashion and jewellery products. Virtual and Physical Prototyping, 2014. **9**(3): p. 195-201.
88. Kuhn, R. and R. Minuzzi, *The 3D printing's panorama in fashion design.* Moda Documenta: Museu, Memoria e Design, 2015. **11**(1): p. 1-12.
89. McCormick, H., et al., *3D-Printing in the Fashion Industry: A Fad or the Future?*, in *Technology-Driven Sustainability*. 2020, Springer. p. 137-154.
90. Kim, S.G., H.R.J.F. Kim, and T.R. Journal, *The recent tendency of fashion textiles by 3D printing.* 2018. **20**(2): p. 117-127.
91. Attaran, M., *The rise of 3-D printing: The advantages of additive manufacturing over traditional manufacturing.* Business Horizons, 2017. **60**(5): p. 677-688.
92. Ford, S. and M. Despeisse, *Additive manufacturing and sustainability: an exploratory study of the advantages and challenges.* Journal of Cleaner Production, 2016. **137**: p. 1573-1587.
93. Gibson, I., D.W. Rosen, and B. Stucker, *Additive Manufacturing Technologies: Rapid Prototyping to Direct Digital Manufacturing*. 2009: Springer Publishing Company, Incorporated. 462.
94. Novakova-Marcincinova, L. and I. Kuric, *Basic and advanced materials for fused deposition modeling rapid prototyping technology.* Manuf. and Ind. Eng, 2012. **11**(1): p. 24-27.
95. Anderegg, D.A., et al., *In-situ monitoring of polymer flow temperature and pressure in extrusion based additive manufacturing.* 2019. **26**: p. 76-83.
96. Watanabe, N., et al. *A model for residual stress and part warpage prediction in material extrusion with application to polypropylene*. in *2016 Annual International Solid Freeform Fabrication Symposium, Austin*. 2016.
97. Gibson, I., D.W. Rosen, and B. Stucker, *Additive manufacturing technologies*. Vol. 17. 2014: Springer.
98. Turner, B.N., R. Strong, and S.A.J.R.P.J. Gold, *A review of melt extrusion additive manufacturing processes: I. Process design and modeling.* 2014.
99. Bellehumeur, C., et al., *Modeling of bond formation between polymer filaments in the fused deposition modeling process.* 2004. **6**(2): p. 170-178.
100. Sun, Q., et al., *Effect of processing conditions on the bonding quality of FDM polymer filaments.* 2008.
101. McIlroy, C. and P. Olmsted, *Disentanglement effects on welding behaviour of polymer melts during the fused-filament-fabrication method for additive manufacturing.* Polymer, 2017. **123**: p. 376-391.
102. Seppala, J.E., et al., *Weld formation during material extrusion additive manufacturing.* Soft matter, 2017. **13**(38): p. 6761-6769.
103. Bartolai, J., T.W. Simpson, and R. Xie, *Predicting strength of additively manufactured thermoplastic polymer parts produced using material extrusion.* Rapid Prototyping Journal, 2018. **24**(2): p. 321-332.
104. McIlroy, C. and P.D. Olmsted, *Deformation of an amorphous polymer during the fused-filament-fabrication method for additive manufacturing.* Journal of Rheology, 2017. **61**(2): p. 379-397.
105. Kuznetsov, V.E., et al., *Strength of PLA Components Fabricated with Fused Deposition Technology Using a Desktop 3D Printer as a Function of Geometrical Parameters of the Process.* Polymers, 2018. **10**(3): p. 313.

106. Wu, W., et al., *Influence of layer thickness and raster angle on the mechanical properties of 3D-printed PEEK and a comparative mechanical study between PEEK and ABS.* 2015. **8**(9): p. 5834-5846.
107. Gordelier, T.J., et al., *Optimising the FDM additive manufacturing process to achieve maximum tensile strength: a state-of-the-art review.* 2019.
108. Momenzadeh, N., et al., *In Situ Measurement of Thermal Strain Development in 420 Stainless Steel Additive Manufactured Metals.* Experimental Mechanics, 2019: p. 1-9.
109. Wach, R.A., P. Wolszczak, and A. Adamus-Wlodarczyk, *Enhancement of Mechanical Properties of FDM-PLA Parts via Thermal Annealing.* Macromolecular Materials and Engineering, 2018. **303**(9): p. 1800169.
110. Bermingham, M., et al., *Optimising the mechanical properties of Ti-6Al-4V components produced by wire+ arc additive manufacturing with post-process heat treatments.* Journal of Alloys and Compounds, 2018. **753**: p. 247-255.
111. Fitzharris, E.R., et al., *Interlayer bonding improvement of material extrusion parts with polyphenylene sulfide using the Taguchi method.* Additive Manufacturing, 2018. **24**: p. 287-297.
112. Torres, J., et al., *Mechanical property optimization of FDM PLA in shear with multiple objectives.* Jom, 2015. **67**(5): p. 1183-1193.
113. Ćwikła, G., et al. *The influence of printing parameters on selected mechanical properties of FDM/FFF 3D-printed parts*. in *IOP Conference Series: Materials Science and Engineering*. 2017. IOP Publishing.
114. Durgun, I. and R. Ertan, *Experimental investigation of FDM process for improvement of mechanical properties and production cost.* Rapid Prototyping Journal, 2014. **20**(3): p. 228-235.
115. Hwang, S., et al., *Thermo-mechanical characterization of metal/polymer composite filaments and printing parameter study for fused deposition modeling in the 3D printing process.* Journal of Electronic Materials, 2015. **44**(3): p. 771-777.
116. Lous, G.M., et al., *Fabrication of piezoelectric ceramic/polymer composite transducers using fused deposition of ceramics.* Journal of the American Ceramic Society, 2000. **83**(1): p. 124-28.
117. Masood, S. and W. Song, *Development of new metal/polymer materials for rapid tooling using fused deposition modelling.* Materials & design, 2004. **25**(7): p. 587-594.
118. Ning, F., et al., *Additive manufacturing of carbon fiber reinforced thermoplastic composites using fused deposition modeling.* Composites Part B: Engineering, 2015. **80**: p. 369-378.
119. Momenzadeh, N., et al., *Polyvinylidene fluoride (PVDF) as a feedstock for material extrusion additive manufacturing.* Rapid Prototyping Journal, 2019.
120. Fischer, F., *Thermoplastics: the best choice for 3D printing.* White Paper, Stratasys Inc., Edn Prairie, MN, 2011.
121. Zaldivar, R., et al., *Influence of processing and orientation print effects on the mechanical and thermal behavior of 3D-Printed ULTEM® 9085 Material.* Additive Manufacturing, 2017. **13**: p. 71-80.

122. Fitzharris, E.R., *Semicrystalline polymers in material extrusion additive manufacturing*. 2019, Georgia Institute of Technology.
123. Mhetre, M.R. and H.K. Abhyankar, *Human exhaled air energy harvesting with specific reference to PVDF film.* Engineering Science and Technology, an International Journal, 2017. **20**(1): p. 332-339.
124. Shapiro, Y., G. Kósa, and A. Wolf, *Shape tracking of planar hyper-flexible beams via embedded PVDF deflection sensors.* IEEE/ASME Transactions on Mechatronics, 2014. **19**(4): p. 1260-1267.
125. Seminara, L., et al., *Piezoelectric polymer transducer arrays for flexible tactile sensors.* IEEE Sensors Journal, 2013. **13**(10): p. 4022-4029.
126. Jafer, E. and K. Arshak, *The use of PE/PVDF pressure and temperature sensors in smart wireless sensor network system developed for environmental monitoring.* Sensor Letters, 2008. **6**(4): p. 477-489.
127. Kim, H., et al., *Integrated 3D printing and corona poling process of PVDF piezoelectric films for pressure sensor application.* Smart Materials and Structures, 2017. **26**(8): p. 085027.
128. HÄMÄLÄINEN, J., *SEMI-CRYSTALLINE POLYOLEFINS IN FUSED DEPOSITION MODELING*. 2017.
129. Zander, N.E., M. Gillan, and R.H. Lambeth, *Recycled polyethylene terephthalate as a new FFF feedstock material.* Additive Manufacturing, 2018. **21**: p. 174-182.
130. Fischer, J., *Handbook of molded part shrinkage and warpage*. 2012: William Andrew.
131. Santis, F.D., et al., *Analysis of shrinkage development of a semicrystalline polymer during injection molding.* Industrial & Engineering Chemistry Research, 2010. **49**(5): p. 2469-2476.
132. Dunsch, R. and J.-M. Breguet, *Unified mechanical approach to piezoelectric bender modeling.* Sensors and Actuators A: physical, 2007. **134**(2): p. 436-446.
133. Mokhtari, F., M. Latifi, and M. Shamshirsaz, *Electrospinning/electrospray of polyvinylidene fluoride (PVDF): piezoelectric nanofibers.* The Journal of The Textile Institute, 2016. **107**(8): p. 1037-1055.
134. Benz, M., W.B. Euler, and O.J. Gregory, *The role of solution phase water on the deposition of thin films of poly (vinylidene fluoride).* Macromolecules, 2002. **35**(7): p. 2682-2688.
135. Miyanaji, H., N. Momenzadeh, and L. Yang, *Effect of printing speed on quality of printed parts in Binder Jetting Process.* Additive Manufacturing, 2018. **20**: p. 1-10.
136. Li, H., et al., *The effect of process parameters in fused deposition modelling on bonding degree and mechanical properties.* Rapid Prototyping Journal, 2018. **24**(1): p. 80-92.
137. Torrado, A.R., et al., *Characterizing the effect of additives to ABS on the mechanical property anisotropy of specimens fabricated by material extrusion 3D printing.* Additive Manufacturing, 2015. **6**: p. 16-29.
138. A.B., S., H. N., and L. G., *Influence of the particle size distribution on surface quality and mechanical properties in AM steel parts.* Rapid Prototyping Journal, 2011. **17**(3): p. 195-202.

139. Sun, Q., et al., *Effect of processing conditions on the bonding quality of FDM polymer filaments.* Rapid Prototyping Journal, 2008. **14**(2): p. 72-80.
140. N. Turner, B., R. Strong, and S. A. Gold, *A review of melt extrusion additive manufacturing processes: I. Process design and modeling.* Rapid Prototyping Journal, 2014. **20**(3): p. 192-204.
141. Mahmood, S., et al., *Tensile strength of partially filled FFF printed parts: experimental results.* Rapid Prototyping Journal, 2017. **23**(1): p. 122-128.
142. Srinivas, V., C.S. van Hooy-Corstjens, and J.A. Harings, *Correlating molecular and crystallization dynamics to macroscopic fusion and thermodynamic stability in fused deposition modeling; a model study on polylactides.* Polymer, 2018. **142**: p. 348-355.
143. D'Amico, A.A., A. Debaie, and A.M. Peterson, *Effect of layer thickness on irreversible thermal expansion and interlayer strength in fused deposition modeling.* Rapid Prototyping Journal, 2017. **23**(5): p. 943-953.
144. Cui, H., et al., *Three-dimensional printing of piezoelectric materials with designed anisotropy and directional response.* Nature materials, 2019. **18**(3): p. 234.
145. Lessing, J., et al., *Inkjet Printing of conductive inks with high lateral resolution on omniphobic "Rf paper" for paper-based electronics and MEMS.* Advanced Materials, 2014. **26**(27): p. 4677-4682.
146. Villacres, J., D. Nobes, and C. Ayranci, *Additive manufacturing of shape memory polymers: effects of print orientation and infill percentage on mechanical properties.* Rapid Prototyping Journal, 2018. **24**(4): p. 744-751.
147. Nematollahi, M., et al., *Application of NiTi in Assistive and Rehabilitation Devices: A Review.* Bioengineering, 2019. **6**(2): p. 37.
148. Oliveira, J., et al., *Polymer-based smart materials by printing technologies: Improving application and integration.* Additive Manufacturing, 2018. **21**: p. 269-283.
149. Fakhzan, M. and A.G. Muthalif. *Vibration based energy harvesting using piezoelectric material*. in *2011 4th International Conference on Mechatronics (ICOM)*. 2011. IEEE.
150. Mueller, I., *Inspection of piezoelectric transducers used for structural health monitoring systems.* 2017.
151. Safaei, M., R.M. Meneghini, and S.R. Anton, *Energy harvesting and sensing with embedded piezoelectric ceramics in knee implants.* IEEE/ASME Transactions on Mechatronics, 2018. **23**(2): p. 864-874.
152. Patel, I., E. Siores, and T. Shah, *Utilisation of smart polymers and ceramic based piezoelectric materials for scavenging wasted energy.* Sensors and Actuators A: Physical, 2010. **159**(2): p. 213-218.
153. Ribeiro, C., et al., *Piezoelectric polymers as biomaterials for tissue engineering applications.* Colloids and Surfaces B: Biointerfaces, 2015. **136**: p. 46-55.
154. Chorsi, M.T., et al., *Piezoelectric biomaterials for sensors and actuators.* Advanced Materials, 2019. **31**(1): p. 1802084.
155. Klimiec, E., et al., *Piezoelectric polymer films as power converters for human powered electronics.* Microelectronics Reliability, 2008. **48**(6): p. 897-901.

156. Nguyen, H., A. Navid, and L. Pilon, *Pyroelectric energy converter using co-polymer P (VDF-TrFE) and Olsen cycle for waste heat energy harvesting.* Applied thermal engineering, 2010. **30**(14-15): p. 2127-2137.
157. Oh, S.R., et al., *Fabrication of piezoelectric polymer multilayers on flexible substrates for energy harvesting.* Smart materials and structures, 2013. **23**(1): p. 015013.
158. Toprak, A. and O. Tigli, *MEMS scale PVDF-TrFE-based piezoelectric energy harvesters.* Journal of Microelectromechanical Systems, 2015. **24**(6): p. 1989-1997.
159. Sharma, T., et al., *Patterning piezoelectric thin film PVDF–TrFE based pressure sensor for catheter application.* Sensors and Actuators A: physical, 2012. **177**: p. 87-92.
160. Abdullah, I.Y., et al., *Influence of Temperature on Crystalline Structure of Polyvinylidene Fluoride.* Intern J Tech Res Appl, 2015. **23**: p. 46-50.
161. Satapathy, S., et al., *Crystallization of Beta-phase Poly (vinylidene fluoride) films using dimethyl sulfoxide (DMSO) solvent and at suitable annealing condition.* arXiv preprint arXiv:0808.0419, 2008.
162. Tiwari, V. and G. Srivastava, *Effect of thermal processing conditions on the structure and dielectric properties of PVDF films.* Journal of Polymer Research, 2014. **21**(11): p. 587.
163. Momenzadeh, N., H. Miyanaji, and T.A. Berfield, *Influences of zirconium tungstate additives on characteristics of polyvinylidene fluoride (PVDF) components fabricated via material extrusion additive manufacturing process.* The International Journal of Advanced Manufacturing Technology, 2019.
164. Ke, K., et al., *Achieving β-phase poly (vinylidene fluoride) from melt cooling: Effect of surface functionalized carbon nanotubes.* Polymer, 2014. **55**(2): p. 611-619.
165. Cai, X., et al., *A critical analysis of the α, β and γ phases in poly (vinylidene fluoride) using FTIR.* RSC advances, 2017. **7**(25): p. 15382-15389.
166. Ahn, Y., et al., *Enhanced piezoelectric properties of electrospun poly (vinylidene fluoride)/multiwalled carbon nanotube composites due to high β-phase formation in poly (vinylidene fluoride).* The Journal of Physical Chemistry C, 2013. **117**(22): p. 11791-11799.
167. Kaura, T., R. Nath, and M. Perlman, *Simultaneous stretching and corona poling of PVDF films.* Journal of Physics D: Applied Physics, 1991. **24**(10): p. 1848.
168. Rossini, N., et al., *Methods of measuring residual stresses in components.* Materials & Design, 2012. **35**: p. 572-588.
169. Li, J.-g. and S.-q. Wang, *Distortion caused by residual stresses in machining aeronautical aluminum alloy parts: recent advances.* The International Journal of Advanced Manufacturing Technology, 2017. **89**(1-4): p. 997-1012.
170. Kanchidurai, S., et al. *A review of inducing compressive residual stress–shot peening; on structural metal and welded connection*. in *IOP Conference Series: Earth and Environmental Science*. 2017. IOP Publishing.
171. van Zyl, I., I. Yadroitsava, and I. Yadroitsev, *Residual stress in Ti6Al4V objects produced by direct metal laser sintering.* South African Journal of Industrial Engineering, 2016. **27**(4): p. 134-141.

172. Babu, S.S., et al., *Additive manufacturing of materials: Opportunities and challenges.* MRS Bulletin, 2015. **40**(12): p. 1154-1161.
173. Yadollahi, A. and N. Shamsaei, *Additive manufacturing of fatigue resistant materials: Challenges and opportunities.* International Journal of Fatigue, 2017. **98**: p. 14-31.
174. Momenzadeh, N., et al., *In situ measurement of thermal strain development in 420 stainless steel additive manufactured metals.* Experimental Mechanics, 2019. **59**(6): p. 819-827.
175. Ali, H., et al., *In-situ residual stress reduction, martensitic decomposition and mechanical properties enhancement through high temperature powder bed pre-heating of Selective Laser Melted Ti6Al4V.* Materials Science and Engineering: A, 2017. **695**: p. 211-220.
176. Uzan, N.E., et al., *On the effect of shot-peening on fatigue resistance of AlSi10Mg specimens fabricated by additive manufacturing using selective laser melting (AM-SLM).* Additive Manufacturing, 2018. **21**: p. 458-464.
177. Kalentics, N., et al., *3D Laser Shock Peening–A new method for the 3D control of residual stresses in Selective Laser Melting.* Materials & Design, 2017. **130**: p. 350-356.
178. Denlinger, E.R., et al., *Effect of inter-layer dwell time on distortion and residual stress in additive manufacturing of titanium and nickel alloys.* Journal of Materials Processing Technology, 2015. **215**: p. 123-131.
179. Cheng, L., et al., *On utilizing topology optimization to design support structure to prevent residual stress induced build failure in laser powder bed metal additive manufacturing.* Additive Manufacturing, 2019. **27**: p. 290-304.
180. Cheng, L. and A. To, *Part-scale build orientation optimization for minimizing residual stress and support volume for metal additive manufacturing: Theory and experimental validation.* Computer-Aided Design, 2019. **113**: p. 1-23.
181. El Moumen, A., M. Tarfaoui, and K. Lafdi, *Modelling of the temperature and residual stress fields during 3D printing of polymer composites.* The International Journal of Advanced Manufacturing Technology, 2019. **104**(5-8): p. 1661-1676.
182. Yang, L., et al., *Experimental investigations for optimizing the extrusion parameters on FDM PLA printed parts.* Journal of Materials Engineering and Performance, 2019. **28**(1): p. 169-182.
183. Spoerk, M., C. Holzer, and J. Gonzalez-Gutierrez, *Material extrusion-based additive manufacturing of polypropylene: A review on how to improve dimensional inaccuracy and warpage.* Journal of Applied Polymer Science, 2020. **137**(12): p. 48545.
184. Wang, J., *PVT properties of polymers for injection molding.* Some Critical Issues for Injection Molding, 2012: p. 3-30.
185. Stansbury, J.W. and M.J. Idacavage, *3D printing with polymers: Challenges among expanding options and opportunities.* Dental Materials, 2016. **32**(1): p. 54-64.
186. Nieto, D.M., V.C. López, and S.I. Molina, *Large-format polymeric pellet-based additive manufacturing for the naval industry.* Additive Manufacturing, 2018. **23**: p. 79-85.

187. Turner, B.N. and S.A. Gold, *A review of melt extrusion additive manufacturing processes: II. Materials, dimensional accuracy, and surface roughness.* Rapid Prototyping Journal, 2015.
188. Wang, T.-M., J.-T. Xi, and Y. Jin, *A model research for prototype warp deformation in the FDM process.* The International Journal of Advanced Manufacturing Technology, 2007. **33**(11): p. 1087-1096.
189. Herrmann, K.-H., et al., *3D printing of MRI compatible components: Why every MRI research group should have a low-budget 3D printer*. Vol. 36. 2014.
190. Momenzadeh, N., H. Miyanaji, and T.A. Berfield, *Influences of zirconium tungstate additives on characteristics of polyvinylidene fluoride (PVDF) components fabricated via material extrusion additive manufacturing process.* The International Journal of Advanced Manufacturing Technology, 2019. **103**(9-12): p. 4713-4720.
191. Prime, M.B., *Cross-sectional mapping of residual stresses by measuring the surface contour after a cut.* J. Eng. Mater. Technol., 2001. **123**(2): p. 162-168.
192. Casavola, C., et al., *Residual stress measurement in Fused Deposition Modelling parts.* Polymer Testing, 2017. **58**: p. 249-255.
193. Schajer, G.S. and P.S. Whitehead, *Hole drilling and ring coring.* Practical residual stress measurement methods, 2013: p. 29-64.
194. Prevey, P.S., *X-ray diffraction residual stress techniques.* ASM International, ASM Handbook., 1986. **10**: p. 380-392.
195. Allen, A., et al., *Neutron diffraction methods for the study of residual stress fields.* Advances in Physics, 1985. **34**(4): p. 445-473.
196. Guo, J., et al., *Recent Progress of Residual Stress Measurement Methods: A Review.* Chinese Journal of Aeronautics, 2019.
197. N., T.B. and G.S. A, *A review of melt extrusion additive manufacturing processes: II. Materials, dimensional accuracy, and surface roughness.* Rapid Prototyping Journal, 2015. **21**(3): p. 250-261.
198. Hill, M.R.J.P.r.s.m.m., *The slitting method.* 2013: p. 89-108.
199. Schajer, G.S. and M.B. Prime, *Residual stress solution extrapolation for the slitting method using equilibrium constraints.* 2007.
200. Prime, M.B. and D.L. Crane, *Slitting method measurement of residual stress profiles, including stress discontinuities, in layered specimens*, in *Residual Stress, Thermomechanics & Infrared Imaging, Hybrid Techniques and Inverse Problems, Volume 8*. 2014, Springer. p. 93-102.
201. Prime, M. and P. Pagliaro. *Uncertanty, Model Error, and Improving the Accuracy of Residual Stress Inverse Solutions*. in *SEM Annual Conference and Exposition on Experimental and Applied Mechanics 2006*. 2006. Society for Experimental Mechanics.
202. Cheng, W. and I. Finnie, *Residual stress measurement and the slitting method*. 2007: Springer Science & Business Media.
203. Lee, M.J. and M.R.J.E.M. Hill, *Intralaboratory repeatability of residual stress determined by the slitting method.* 2007. **47**(6): p. 745.
204. Yaowu, X. and B.J.C.J.o.A. Rui, *Residual stress determination in friction stir butt welded joints using a digital image correlation-aided slitting technique.* 2017. **30**(3): p. 1258-1269.

205. Shokrieh, M.M. and S.J.J.o.c.m. Akbari R, *Simulation of slitting method for calculation of compliance functions of laminated composites.* 2012. **46**(9): p. 1101-1109.
206. Turner, B.N., R. Strong, and S.A. Gold, *A review of melt extrusion additive manufacturing processes: I. Process design and modeling.* Rapid Prototyping Journal, 2014.
207. Spoerk, M., et al., *Shrinkage and Warpage Optimization of Expanded-Perlite-Filled Polypropylene Composites in Extrusion-Based Additive Manufacturing.* Macromolecular Materials and Engineering, 2017. **302**(10): p. 1700143.
208. Spoerk, M., et al. *The consequences of different printing chamber temperatures in extrusion-based additive manufacturing*. in *International Conference on Polymers and Moulds Innovations-PMI 2018*. 2018. Institute of Polymers and Composites, University of Minho, Portugal.
209. Armillotta, A., et al., *Warpage of FDM parts: Experimental tests and analytic model.* 2018. **50**: p. 140-152.
210. Cheng, S., et al., *Mechanical and thermal properties of chicken feather fiber/PLA green composites.* Composites Part B: Engineering, 2009. **40**(7): p. 650-654.
211. Kantaros, A. and D. Karalekas, *Fiber Bragg grating based investigation of residual strains in ABS parts fabricated by fused deposition modeling process.* Materials & Design, 2013. **50**: p. 44-50.
212. Chu, X., et al., *Mechanical and thermal expansion properties of glass fibers reinforced PEEK composites at cryogenic temperatures.* Cryogenics, 2010. **50**(2): p. 84-88.
213. Luo, N., et al., *Preparation and characterization of PVDF-glass fiber composite membrane reinforced by interfacial UV-grafting copolymerization.* Journal of Environmental Sciences, 2015. **38**: p. 24-35.
214. Oddone, V., R.C. Wimpory, and S. Reich, *Understanding the negative thermal expansion in planar graphite–metal composites*. Journal of Materials Science, 2019. **54**(2): p. 1267-1274.
215. Evans, J.S., *Negative thermal expansion materials.* Journal of the Chemical Society, Dalton Transactions, 1999(19): p. 3317-3326.
216. Takenaka, K., *Negative thermal expansion materials: technological key for control of thermal expansion.* Science and technology of advanced materials, 2012. **13**(1): p. 013001.
217. Turner, P.S., *The problem of thermal-expansion stresses in reinforced plastics.* 1942.
218. Johnson, R.R., M.H. Kural, and G.B. Mackey, *Thermal Expansion Properties of Composite Materials*. 1981, LOCKHEED MISSILES AND SPACE CO INC SUNNYVALE CA.
219. James, J., et al., *A review of measurement techniques for the thermal expansion coefficient of metals and alloys at elevated temperatures.* Measurement Science and Technology, 2001. **12**(3): p. R1.
220. Forster, A.M., *Materials testing standards for additive manufacturing of polymer materials.* NI: ST, Department of Commerce, 2015.
221. Dizon, J.R.C., et al., *Mechanical Characterization of 3D-Printed Polymers.* Additive Manufacturing, 2017.

CURRICULUM VITA

Niknam Momenzadeh

(502) 644-1767
Niknam.momenzadeh@louisville.edu

Education

-**Doctor of Philosophy** in Mechanical Engineering 2016-Present
University of Louisville; Louisville, KY

-**Master of Science** in Mechanical Engineering (Manufacturing) 2012-2015
Islamic Azad University; Tehran, Iran

-**Bachelor of Science** in Mechanical Engineering (Manufacturing) 2007-2012
Islamic Azad University; Tehran, Iran

-National Organization for Development of Exceptional Talents (NODET) 2000-2007
Esfahan, Iran

Honors and Awards

-Graduate Teaching Assistantship, University of Louisville, United states 2017-Present

-UofL-National Science Foundation I-Corps Research Award 2017

-Member of Graduate Teacher Assistant Academy, 2016
School of Interdisciplinary and Graduate Studies, Louisville, United states

Research Experience

-Department of Mechanical Engineering; 2018-Present
University of Louisville, Louisville, KY
Project: In-situ thermal strain development in additive manufactured metals.
Under Supervision of Dr. Sundar Atre and Dr. T.A. Berfield

-Department of Mechanical Engineering; 2017-Present
University of Louisville, Louisville, KY
Project: Stress effects on properties of smart materials fabricated through material extrusion deposition processes.
Under Supervision of Dr. T.A. Berfield

-Department of Mechanical Engineering; 2017-2018
University of Louisville, Louisville, KY
Project: Effect of printing speed on quality of printed parts in binder jetting additive manufacturing process.
Under Supervision of Dr. Li Yang

-Department of Mechanical Engineering; 2013-2015
University of Louisville, Louisville, KY

Project: Design, simulation and analysis of a novel customized dental implant using additive manufacturing technology.

Under Supervision of Dr. S. Rahmati and Dr. A. Azari

Student Leadership Experience

-President of Iranian student organization, University of Louisville 2017-2019

-Supervised undergrad and graduate students, University of Louisville 2017-2019

Publication

-**Momenzadeh, N.**, T. A. Berfield. "Electromechanical Enhancement of Material Extrusion Additively Manufactured Polyvinylidene Fluoride Structures" [Submitted]

-**N. Momenzadeh**, H. Miyanaji, D. A. Porter, T. A. Berfield, "Polyvinylidene Fluoride (PVDF) as a Feedstock Material in Fused Filament Fabrication (FFF) ", Rapid prototyping journal, Emerald, 2019.

-**Momenzadeh, N.**, S. D. Nath, T. A. Berfield, and S. V. Atre. "In Situ Measurement of Thermal Strain Development in 420 Stainless Steel Additive Manufactured Metals." *Experimental Mechanics* (2019): 1-9.

-**Momenzadeh, Niknam,** Hadi Miyanaji, and Thomas A. Berfield. "Influences of zirconium tungstate additives on characteristics of polyvinylidene fluoride (PVDF) components fabricated via material extrusion additive manufacturing process." *The International Journal of Advanced Manufacturing Technology* (2019): 1-8.

-Miyanaji, Hadi, **Niknam Momenzadeh**, and Li Yang. "Efffect of powder characteristics on parts fabricated via binder jetting process. " *Rapid Prototyping Journal* 25, no. 2 (2019): 332-342.

-**Momenzadeh, Niknam**, Carson M. Stewart, and Thomas Berfield. "Mechanical and Thermal Characterization of Fused Filament Fabrication Polyvinylidene Fluoride (PVDF) Printed Composites." In Mechanics of Additive and Advanced Manufacturing, Volume 8, pp. 59-65. Springer, Cham, 2019.

-Miyanaji, Hadi, **Niknam Momenzadeh**, and Li Yang. "Effect of printing speed on quality of printed parts in Binder Jetting Process." Additive Manufacturing 20 (2018): 1-10.

-**N. Momenzadeh**, T. A. Berfield, "Influences of printing parameters on semi-crystalline microstructure of fused filament fabrication polyvinylidene fluoride (PVDF) components", in *Proceedings of the Solid Freeform Fabrication Symposium, Austin*, TX, USA, 2018.

-**N. Momenzadeh**, S. Rahmati, A. Azari. "Design, simulation and analysis of a novel customized dental implant using Additive Manufacturing Technology", *Iranian Journal of Manufacturing Engineering*, Vol. 2, No. 2, pp. 52-58, 2015. (In Persian)

Presentation

- "Mechanical and thermal Characterization of Fused Filament Fabrication Polyvinylidene Fluoride (PVDF) Printed Composites", SEM annual conference, Greenville, South Carolina, June 2018.
- "Increasing the piezoelectric responses of polyvinylidene fluoride additively manufactured components", KY Nano + AM symposium, Louisville, Kentucky, August 2018.
- "Influences of printing parameters on semi-crystalline microstructure of fused filament fabrication polyvinylidene fluoride (PVDF) components", Solid freeform fabrication, Austin, Texas, August 2018.
- "Investigation of effect of heat treatment process on PVDF additively manufactured parts", Solid freeform fabrication, Austin, Texas, August 2019.
- "Comparison between piezoelectric and mechanical properties of PVDF and PVDF-TrFE additively manufactured parts", ASME conference, Louisville, Kentucky, September 2019.

Summer of Skills

-Expert in finite element modeling and simulation with Catia, Solid Works, Abaqus, Ansys.
-Ability to work with additive manufacturing systems, such as FDM, SLM, SLA, Binder jetting.
-Knowledge of traditional manufacturing systems, such as CNC, turning, casting.
-Experience conducting materials characterization tests, such as FTIR, XRD, SEM.
-Ability to do mechanical testing, such as tensile, compression, torsion, bending, fatigue.
-Competent with no-contact optical measurement system such as DIC.